UNIVERSITÀ DEGLI STUDI DI MILANO

FACOLTÀ DI SCIENZE E TECNOLOGIE

Corso di Laurea Magistrale in Fisica

3D Inter-Fractional Monitoring in ^{12}C Ion Therapy: Simulation Study of MULTIPASS Detector Performance in the framework of the INSIDE Clinical Trial at CNAO

Relatore Interno:
Prof. Ivan Veronese

Relatrice Esterna:
Dott.ssa Ilaria Mattei

Candidata:
Margherita Pini
Matricola 30423A

Anno Accademico 2024/2025

Contents

Introduction

Ion therapy has become increasingly important for treating deep-seated tumors due to its ability to deliver highly conformal radiation while sparing surrounding healthy tissues [1]. The dose, defined as the energy deposited per unit mass of tissue, can be precisely conformed over the tumor volume due to the characteristic depth–dose profile of charged particles, specifically the Bragg peak. Among charged particles, heavy ions such as carbon ions are especially effective: their high linear energy transfer (LET) and relative biological effectiveness (RBE), combined with a reduced oxygen enhancement ratio (OER), make them well-suited for targeting radioresistant and hypoxic tumors [2, 3].
The total dose prescribed to a patient is determined by the treatment plan, which specifies how the beam should be delivered to target the tumor while minimizing exposure to healthy tissues. To reduce side effects and allow normal tissue recovery, the total dose is typically divided over multiple treatment sessions, called fractions, all following the same treatment plan.

A key aspect of ion therapy is the precise control of the particle range, that is the depth at which the particle beam stops within the patient and releases its therapeutic dose. Accurate knowledge of this range is essential to ensure that the delivered dose matches the distribution prescribed by the treatment plan, effectively targeting the tumor while sparing healthy tissues.
Several sources of uncertainty can affect the particle range, with a potential impact on dose delivery accuracy. These include inaccuracies in medical imaging and in the conversion of imaging data into tissue density and composition, small deviations in patient positioning, and physiological organ motion due to breathing. Altogether, these factors can lead to a total uncertainty of a few millimeters in the dose delivered to a given voxel [4], which is accounted for in the treatment plan by introducing safety margins around the tumor, i.e., additional volumes of tissue surrounding the target.

Range monitoring has been developed to address these uncertainties and reduce safety margins, thereby confining the dose more accurately to the tumor volume, enhancing treatment precision and increasing therapeutic potential, particularly for head and neck tumors and for tumors located close to organs at risk.
The techniques for range monitoring necessarily rely on detecting secondary radiation produced by nuclear interactions between the primary beam and patient nuclei. These secondary particles can exit the body and carry valuable information about the beam's penetration, making them effective observables for verifying the beam during treatment.

In the context of inter-fractional range monitoring, another, but related, objective is to determine whether the patient has undergone morphological variations with respect to the anatomical configuration assumed during treatment planning, as defined by the *planning* Computed Tomography (CT). Although imaging scans can detect anatomical variations, they are not routinely performed and are typically acquired at the midpoint of treatment

sessions, only when clinical indications or disease progression suggest a significant risk of changes affecting dose delivery. In this context, patient-based monitoring systems that indirectly detect anatomical variations, through the measurement of secondary particles exiting the patient's body, represent a practical and promising approach to support re-planning decisions and maintain treatment quality tailored to the individual patient, while avoiding extra dose when an unecessary CT scan is performed.

Within this framework, the Dose Profiler detector, developed by the INSIDE (INnovative Solution for In-beam DosimEtry in hadrontherapy) collaboration and currently installed in treatment room 1 at the CNAO (Centro Nazionale di Adroterapia Oncologica) facility in Pavia, is designed to evaluate morphological changes between treatment sessions by measuring secondary charged particles emitted at large angles (especially secondary protons) in carbon ion treatments. Experimental data from a clinical trial (ClinicalTrials.gov Identifier: NCT03662373) started in August 2019, along with Monte Carlo simulations of selected patient cases, have been analyzed to investigate and support its use. At the same time, these studies highlighted several intrinsic limitations of the detector, including its relatively large distance from the patient, limited solid angle coverage, and restricted rate capability, which constrained the achievable performance.

In response to these limitations, and with the aim of extending its monitoring capabilities, the PRIN (Progetti di Rilevante Interesse Nazionale) MULTIPASS (MULTIPle trAcker for Secondary particleS monitoring) project was launched to develop, construct, and validate a compact prototype detector, specifically designed for charged particle therapy applications. In addition to overcoming the intrinsic constraints of the Dose Profiler, MULTIPASS is capable of detecting secondary protons if used for inter-fractional monitoring in carbon-ion treatments, and prompt-γ radiation if employed for range monitoring in proton therapy. This dual capability enables the identification of morphological changes in the treated region for both types of therapy. The system also aims to the characterization of neutron-induced background radiation produced in ion therapy, which may result in dose deposition in healthy tissues far from the target volume.

This thesis focuses on evaluating, through a Monte Carlo simulation study, the capability of the MULTIPASS detector to identify inter-fractional morphological changes in carbon-ion treatments. The spatial distribution of detected secondary protons is analyzed, with the additional objective of comparing the detector's performance to that of the Dose Profiler under the same monitoring task.
For this study, a patient from the INSIDE clinical trial, diagnosed with intestinal-type adenocarcinoma (ITAC), a malignant tumor originating in the nasal cavities, has been selected. The patient, who had undergone a mid-treatment *control* CT, has been measured and analyzed using the Dose Profiler. Thanks to the the mid-treatment *control* CT, a morphological change has been addressed and the patient was replanned.
Two Monte Carlo simulations of the clinical treatment plan have been performed with the FLUKA code: the first was based on the *planning* CT, representing the patient's anatomy at the start of therapy, and the second was based on the mid-treatment *control* CT, capturing the anatomical changes that occurred during treatment. Together, these simulations effectively emulate two fractions of the same treatment.
In both cases, MULTIPASS has been positioned to reproduce the same spatial orientation and angular acceptance as the Dose Profiler, ensuring a consistent and meaningful comparison between the two systems.
The 3D spatial emission distribution of secondary charged particles recorded by MULTIPASS in each simulation has been analyzed, and morphological changes have been inferred

by comparing the spatial distributions of secondary proton emission coordinates from the *planning* and *control* CT simulations using a gamma index test.
To perform this analysis, a dedicated C++ framework has been developed, extending and adapting the one previously implemented for the Dose Profiler case study.

Building on these motivations, the thesis is organized as follows. Chapter 1 introduces the fundamental physical principles underlying ion therapy, including the biological effects of radiation and the concepts of range monitoring. Chapter 2 presents the detectors studied in this work, with a focus on the design and structure of the MULTIPASS detector, while also providing an overview of the Dose Profiler for comparison. Chapter 3 describes the Monte Carlo simulation of the treatment plan for the selected patient, performed using the FLUKA code. Finally, Chapter 4 details the reconstruction, backtracking and analysis of secondary charged particles produced in the FLUKA simulations and detected by the MULTIPASS detector, in order to evaluate its capability to identify inter-fractional morphological changes and to compare its performance with that of the Dose Profiler.

Chapter 1

Charged Particle Therapy

Radiotherapy is a central modality for cancer treatment, alongside surgery and chemotherapy. Its primary goal is to eradicate malignant cells by inducing irreparable DNA damage while minimizing harm to surrounding healthy tissues. Conventional external beam radiotherapy uses high-energy X-rays and γ-rays, which can reach deep-seated tumours but may also interact with healthy tissues along their path, potentially causing unintended damage. Particle-based radiotherapy, or *hadrontherapy*, was developed to achieve greater selectivity and therapeutic effectiveness by employing charged hadrons, primarily protons and carbon ions. Protons are typically accelerated to 50–250 MeV using cyclotrons or synchrotrons, while carbon ions reach 80–400 MeV/u in synchrotrons. Thanks to their characteristic penetration and stopping behaviour, these particles allow precise targeting of the tumour while sparing surrounding healthy tissues.

The physical interactions of charged particles in tissue that are most relevant for hadrontherapy are described in Section 1.1, and the associated biological effects are presented in Section 1.2. Given this precise targeting—and the enhanced biological effects of charged ions—accurate delivery of the beam to the tumour volume is essential. This requirement has motivated the development of range verification and monitoring techniques, introduced in Section 1.3, which constitute the scientific motivation of the present thesis.

1.1 Interactions of Charged Particles with Matter

Charged Particle Therapy (CPT) is based on the transport of energetic ions through matter. In the therapeutic energy range, the interaction of charged particles with the medium is dominated by electromagnetic processes, primarily inelastic collisions with atomic electrons, which govern the continuous energy loss and determine the characteristic depth–energy deposition profile of the beam. Although electronic interactions represent the primary mechanism of energy deposition, additional processes must be taken into account for an accurate physical description of beam transport. Elastic Coulomb interactions with atomic nuclei lead to multiple scattering, causing a progressive lateral broadening of the beam, while nuclear interactions may induce fragmentation processes, particularly for heavy ions. These effects do not dominate the energy loss but play a crucial role in shaping the spatial distribution of the energy release and in determining secondary particle production, which is relevant for monitoring and modeling purposes.
This section introduces the key physical mechanisms governing charged particle transport in matter. The stopping power is presented as the fundamental quantity describing energy loss and leading to the formation of the Bragg peak. The concepts of particle range and range straggling are then discussed. The role of multiple Coulomb scattering in beam

broadening is examined, followed by an overview of nuclear interactions and fragmentation, which are essential for a comprehensive description of charged particle beams in hadrontherapy.

1.1.1 Stopping power

Charged particle transport in matter is governed predominantly by electromagnetic interactions mediated by Coulomb forces. In the therapeutic energy range relevant for hadrontherapy, the dominant contribution to the interaction of charged particles with matter arises from inelastic collisions with atomic electrons, which determine the energy loss of the projectile along its path.
The description of energy loss is commonly formulated within the framework of the Continuous Slowing Down Approximation (CSDA) [5]. In this approach, the charged particle undergoes a large number of interactions, each transferring a small fraction of energy to the medium. Under these conditions, both the energy loss and the deceleration of the particle can be treated as continuous quantities.

The interactions of a charged particle with the medium can be described in terms of the semiclassical impact parameter b relative to the atomic radius r_{atom}. For $b > r_{\text{atom}}$, the particle undergoes soft inelastic collisions with the electron cloud, leading to the excitation or ionization of outer-shell electrons. These interactions are associated with high cross sections and small energy transfers per event, and they dominate the total number of energy-depositing collisions. When $b \sim r_{\text{atom}}$, hard inelastic collisions with inner-shell electrons occur, producing energetic secondary electrons, also known as knock-on or δ rays. These events have lower cross sections than soft collisions but involve substantially higher energy transfers per interaction. For $b < r_{\text{atom}}$, the particle can interact with the nuclear electric field, giving rise to elastic or inelastic scattering on nuclei. Nuclear interactions occur with comparatively low cross sections relative to electronic collisions. At very high energies, or for light charged particles such as electrons, inelastic scattering in the nuclear field can result in radiative energy losses via bremsstrahlung.

The mean energy loss per unit path length, or linear stopping power S, is defined as

$$S = -\frac{\mathrm{d}E}{\mathrm{d}x}, \tag{1.1}$$

where E denotes the kinetic energy of the particle and x the distance traversed in the medium. The total stopping power can be expressed as the sum of the contributions arising from the different interaction mechanisms:

$$S = S_{\text{el}}^{\text{hard}} + S_{\text{el}}^{\text{soft}} + S_{\text{rad}} + S_{\text{nucl}}, \tag{1.2}$$

where $S_{\text{el}}^{\text{hard}}$ and $S_{\text{el}}^{\text{soft}}$ correspond to electronic stopping due to hard and soft collisions, respectively, S_{rad} accounts for radiative energy losses, and S_{nucl} represents energy loss due to elastic interactions with nuclei.

A semi-classical description of energy loss for heavy charged particles was first proposed by Bohr [6], later generalized by Bethe and subsequently refined by Bloch to incorporate quantum-mechanical effects, leading to the well-known Bethe–Bloch formulation of stopping power [7, 8].
The Bethe–Bloch theory assumes that the projectile velocity is large compared to the orbital velocities of atomic electrons, that the projectile mass is much larger than the

electron mass, and that nuclear reactions can be neglected. Under these conditions, the stopping power is dominated by electronic interactions ($S \simeq S_{\mathrm{el}}^{\mathrm{hard}} + S_{\mathrm{el}}^{\mathrm{soft}}$):

$$-\frac{\mathrm{d}E}{\mathrm{d}x} = 4\pi N_A r_e^2 m_e c^2 \, \rho \, \frac{Z_p^2 Z_t}{A_t} \frac{1}{\beta^2} \left[\ln\left(\frac{2 m_e c^2 \beta^2 \gamma^2 T_{\max}}{I^2} \right) - \beta^2 \right], \tag{1.3}$$

where:

- N_A is Avogadro's number;
- r_e and m_e are the classical electron radius and the electron mass, respectively;
- ρ, Z_t and A_t denote the density, atomic number and atomic mass of the target material;
- Z_p and $\beta = v_p/c$ are the charge number and the velocity of the incident particle, expressed in units of the speed of light c;
- $T_{\max}$ is the maximum kinetic energy that can be transferred to an atomic electron in a single collision;
- I is the mean excitation (or ionization) potential of the target medium;
- $\gamma = (1-\beta^2)^{-1/2}$ is the Lorentz factor.

Expression 1.3 is valid in the interval $0.1 \lesssim \beta\gamma \lesssim 1000$, where the assumptions underlying the Bethe–Bloch theory are satisfied. Outside this range, additional corrections must be introduced.
For $\beta\gamma \lesssim 0.1$, the projectile velocity becomes comparable to the orbital velocities of bound atomic electrons. As a consequence, the assumption of free and stationary target electrons breaks down. This effect is taken into account by the *shell correction* C, which accounts for the atomic structure of the medium and reduces the stopping power with respect to the Bethe–Bloch prediction.
For $\beta\gamma \gtrsim 1000$, corresponding to the ultra-relativistic regime, the transverse electric field of the projectile induces polarization of the medium. This collective response of the electrons effectively screens the long-range Coulomb field of the projectile, limiting the contribution of distant collisions. The resulting reduction of the stopping power is described by the *density-effect correction* δ. The corrected Bethe–Bloch formula reads [9]:

$$-\frac{\mathrm{d}E}{\mathrm{d}x} = 4\pi N_A r_e^2 m_e c^2 \, \rho \, \frac{Z_p^2 Z_t}{A_t} \frac{1}{\beta^2} \left[\ln\left(\frac{2 m_e c^2 \beta^2 \gamma^2 T_{\max}}{I^2} \right) - \beta^2 - \frac{\delta}{2} - \frac{C}{Z_t} \right]. \tag{1.4}$$

In order to reduce the explicit dependence of the stopping power on the target material density, it is convenient to introduce the *mass stopping power*, defined as the stopping power normalized to the mass density ρ of the medium,

$$\frac{S}{\rho} = -\frac{1}{\rho}\frac{\mathrm{d}E}{\mathrm{d}x}, \tag{1.5}$$

which is commonly expressed in units of $\mathrm{MeV\,cm^2/g}$.

The kinetic-energy dependence of the mass stopping power can be divided into four characteristic regimes, illustrated for positive muons in copper in Figure 1.1.

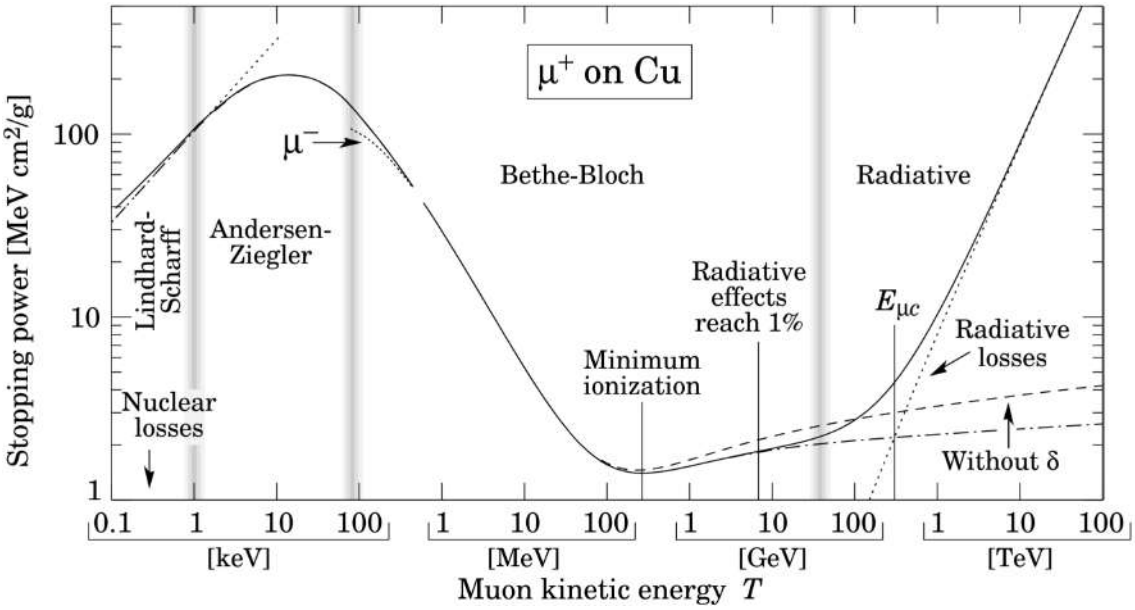

Figure 1.1: Mass stopping power for positive muons in copper as a function of kinetic energy T. Vertical bands indicate boundaries between regions with different dominant physical processes. Image from [10].

At low energies, $\frac{S}{\rho}$ rises with increasing kinetic energy, reaching a maximum around $250I$, where atomic shell effects are significant and shell corrections to the Bethe–Bloch formula dominate.
In the intermediate-energy range, mass stopping power decreases roughly as $1/\beta^2$, reaching a broad minimum for kinetic energies on the order of 2–2.5 times the particle rest mass. This reflects the reduced interaction time between the projectile and atomic electrons and corresponds to the region of minimum-ionizing particles.
At higher energies, $\frac{S}{\rho}$ increases gradually with kinetic energy due to relativistic effects, while radiative contributions, such as bremsstrahlung, become noticeable only at ultra-relativistic velocities, remaining subdominant for moderately relativistic particles. This behaviour is illustrated in Figure 1.2, which shows the mass stopping power for muons, pions and protons in different materials. While the overall energy dependence is similar across media, the absolute magnitude of $\frac{S}{\rho}$ depends on both the properties of the projectile and those of the absorbing medium. In particular, the mass stopping power depends explicitly on the projectile charge Z_p and velocity β, but is independent of the projectile mass. As a consequence, heavy charged particles with identical Z_p and β experience the same stopping power in a given medium.

The influence of the absorbing medium on the stopping power is governed by three main parameters. The ratio Z_t/A_t, which decreases slightly from light to heavy elements (with the exception of hydrogen, for which $Z_t/A_t = 1$), enters linearly in the Bethe–Bloch formula and inversely affects S, as shown for $\frac{S}{\rho}$ in Figure 1.2. The mean excitation potential I, which generally increases with atomic number, plays a crucial role in determining the magnitude of the stopping power. Finally, the material density ρ scales the stopping power linearly with the amount of matter traversed per unit path length.

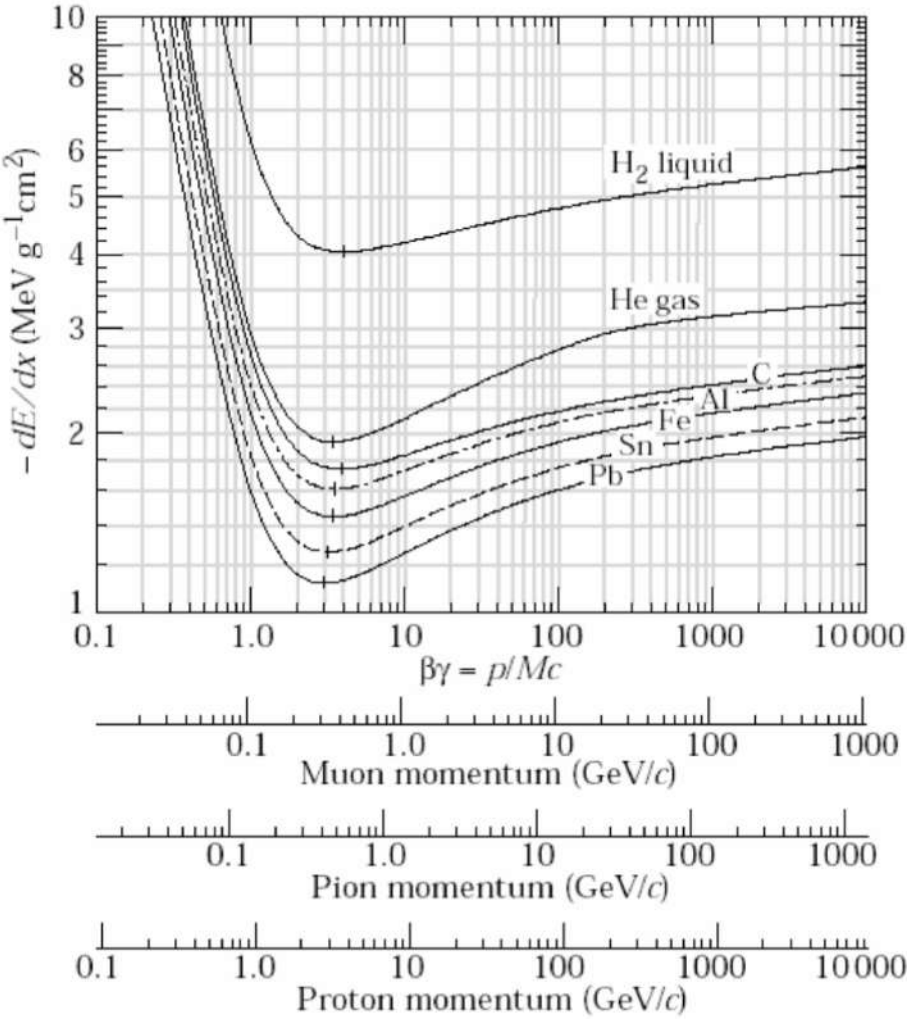

Figure 1.2: Mass stopping power for muons, pions and protons in various materials. Image from [11].

1.1.2 Bragg Peak

From Figure 1.1 it can be observed that, for heavy charged particles, the energy released in the medium is strongly concentrated at low particle velocities, corresponding to the final portion of the particle trajectory. This pronounced maximum in the depth–energy release distribution is known as the *Bragg peak* (Figure 1.3, left). The depth at which the Bragg peak occurs is determined by the initial energy of the particle beam: increasing the beam energy leads to deeper penetration into the medium and a corresponding shift of the Bragg peak to larger depths.
This distinctive depth-dependent energy deposition profile represents a key physical feature underlying the potential advantages of charged particle beams over conventional X-rays in radiation therapy. The strong localization of energy release near the end of the particle range allows a high concentration of energy to be delivered within the tumour region, while reducing the energy deposited in the surrounding healthy tissues. In contrast, high-energy photon beams release energy more gradually along their path, resulting in a less localized interaction pattern and a larger exposure of non-target tissues.

In clinical applications, the finite thickness of the tumor is accounted for by superimpos-

ing particle beams of different initial energies, resulting in a composite longitudinal profile known as the *Spread-Out Bragg Peak* (SOBP), shown in the right panel of Figure 1.3. The SOBP enables a nearly uniform energy release throughout the target region, while preserving the steep fall-off beyond the distal edge, thereby maintaining the spatial selectivity characteristic of charged particle beams.

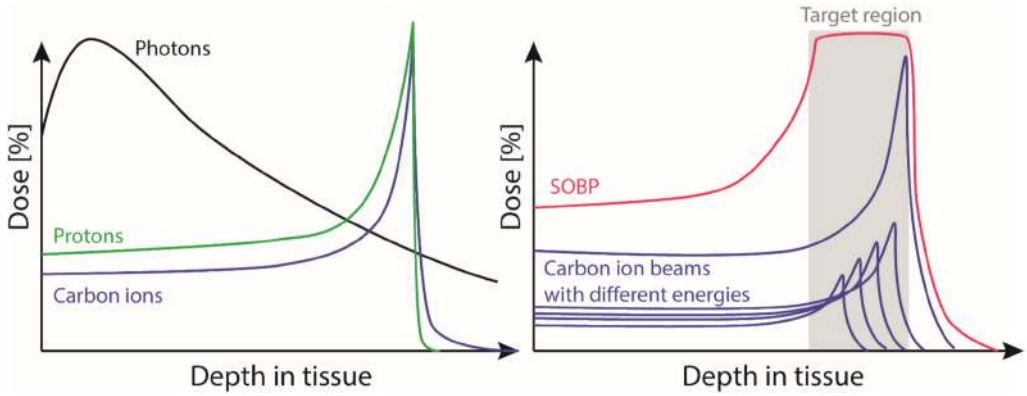

Figure 1.3: Depth–dose distributions of different radiation types in tissue. Here, the term *dose* is used to indicate the energy released per unit mass of tissue, providing a qualitative view of energy deposition; a formal definition will be given in Section 1.2. On the left, the curves show the depth dependence for a high-energy photon beam (black), a proton beam (green), and a carbon ion beam (blue). On the right, the superposition of several mono-energetic carbon ion beams produces a Spread-Out Bragg Peak. Image adapted from [12].

1.1.3 Range

Within the framework of the CSDA, the total distance traveled by a charged particle in a given material is defined as its *range*. Due to the stochastic nature of the underlying interaction processes, the number of collisions required to bring a particle to rest varies slightly from one particle to another. Consequently, the penetration depth is not a unique quantity but exhibits a statistical spread, commonly referred to as *range straggling*.

For practical purposes, the particle range is generally defined as an average quantity. Specifically, the mean range corresponds to the depth beyond which 50% of the incident particles are stopped in the medium. Experimentally, this quantity can be determined by measuring the depth–energy deposition profile produced by a monoenergetic particle beam of given intensity impinging on the target material.

Within the CSDA, the average range $R(E_0)$ of a monoenergetic beam with initial kinetic energy E_0 can be expressed as

$$R(E_0) = \int_0^{E_0} \left(\frac{\mathrm{d}E}{\mathrm{d}x}\right)^{-1} \mathrm{d}E, \tag{1.6}$$

where $\mathrm{d}E/\mathrm{d}x$ denotes the stopping power of the particle in the considered medium.

The CSDA range in water as a function of the energy for different ion species is illustrated in Figure 1.4.

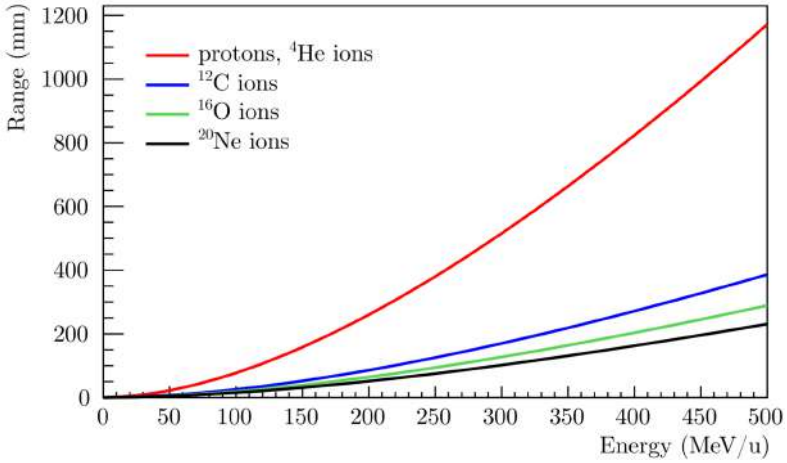

Figure 1.4: CSDA range in water as a function of the energy for protons (red line), ^{4}He (red line), ^{12}C (blue line), ^{16}O (green line) and ^{20}Ne (black line) ions. Image from [13].

1.1.4 Multiple Coulomb Scattering

As discussed in Subsection 1.1.1, charged particles traversing a material can undergo elastic interactions with atomic nuclei. Among these, Coulomb-mediated scattering exhibits the largest cross section. When the mass of the incident particle is much smaller than that of the nucleus, the energy transferred in each collision is negligible, and the dominant effect is a deflection of the particle trajectory. Repeated small-angle deflections accumulate along the path, giving rise to a statistical lateral spread of the beam, commonly referred to as *multiple Coulomb scattering*.
Although multiple Coulomb scattering contributes only marginally to the total energy loss, it strongly influences the spatial distribution of the particle beam. The cumulative effect of many small-angle deflections results in a progressive broadening of the beam as it propagates through the medium. The magnitude of this effect increases with the atomic number of the target material and is inversely proportional to the particle mass and velocity. Consequently, for the same penetration depth, heavier particles such as carbon ions exhibit a narrower lateral spread than protons.

A rigorous description of multiple scattering is provided by Molière's theory [14], which accounts for the full angular distribution of deflections. For practical purposes, the distribution of net deflection angles can be approximated by a Gaussian centered at zero, whose root-mean-square angular width θ_0 is given by the *Highland approximation* [15, 16]:

$$\theta_0 = \frac{14.1 \text{ MeV}}{\beta c p} Z_p \sqrt{\frac{L}{L_0}} \left[1 + 0.0083 \ln\left(\frac{L}{L_0}\right) \right], \tag{1.7}$$

where p is the particle momentum, Z_p its charge, βc its velocity, L the path length in the material, and L_0 the radiation length of the medium. The formula shows that multiple scattering increases with projectile charge and target thickness, but decreases for heavier and faster particles.

Figure 1.5 illustrates the lateral spread of proton and carbon-ion beams as a function of depth in a representative medium. Protons exhibit a larger angular deviation compared to carbon ions, while the scattering increases near the end of the particle range due to the reduced particle velocity [13].

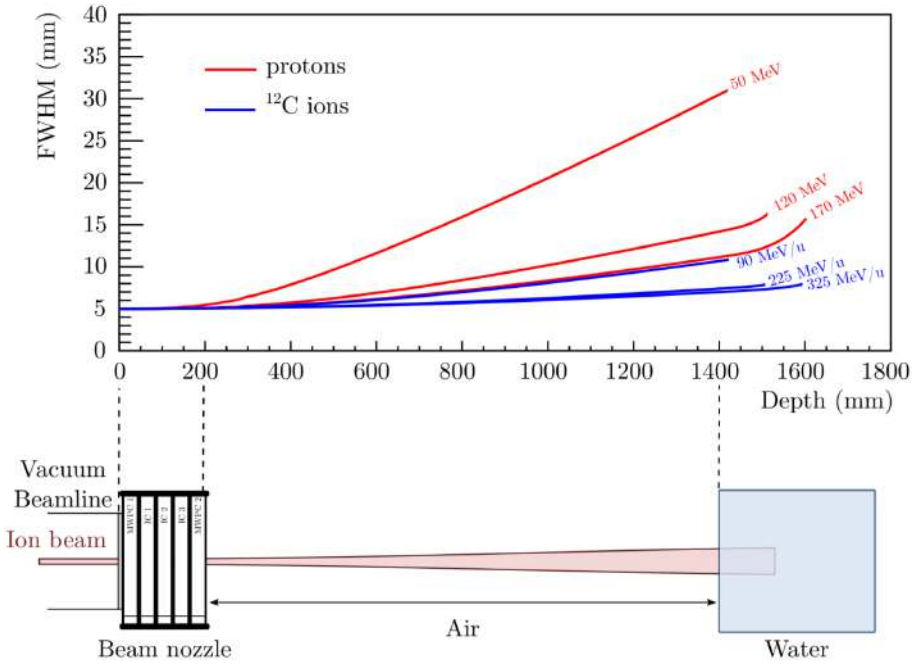

Figure 1.5: Lateral beam width as a function of the depth for protons (red lines) and carbon ions (blue lines) at different energies (top panel) for a setup representing a clinical case (bottom panel). Image from [13].

1.1.5 Nuclear Fragmentation

At the kinetic energies typical of hadrontherapy, charged particles can overcome the Coulomb barrier, allowing nuclear interactions with the target nuclei. These interactions may lead to *nuclear fragmentation*, which occurs via two distinct mechanisms depending on the projectile type: *target fragmentation*, in which the struck nucleus disintegrates, and *projectile fragmentation*, in which the incident ion itself breaks up.

Protons at therapeutic energies can induce only target fragmentation, whereas heavier ions may undergo projectile fragmentation, producing secondary ions with lower mass and charge but energies comparable to the primary beam.
Target fragmentation occurs along the entire beam path until the Bragg peak, producing predominantly short-ranged fragments that deposit their energy near the interaction vertex. In contrast, projectile fragmentation produces forward-emitted fragments that continue to propagate through the medium.
The particles directly produced in these nuclear reactions are referred to as *secondary fragments*, while those generated in subsequent interactions of secondary fragments are called *tertiary fragments*. The combined presence of primary particles, secondary and tertiary fragments results in a *mixed radiation field*, characterized by a broad spectrum of particle species with different charge, mass, and energy, all contributing to the total energy deposition.

Figure 1.6 illustrates the depth-dose contributions from primary ions, secondary fragments, and tertiary fragments for a 330 MeV/u ^{12}C beam in water, highlighting how the fragments give rise to the characteristic dose tail beyond the Bragg peak.

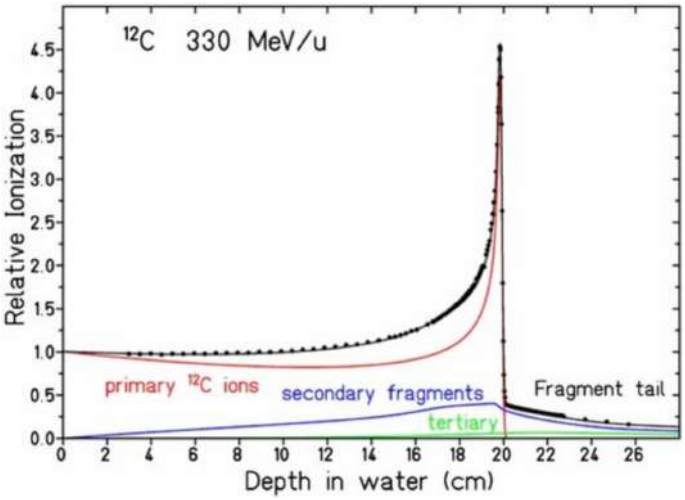

Figure 1.6: Dose contributions as a function of depth in water for a 330 MeV/u ^{12}C ion beam. The red curve represents the dose deposited by primary carbon ions, while the blue and green curves correspond to contributions from secondary and tertiary nuclear fragments, respectively. The black curve shows the total depth-dose distribution resulting from the superposition of all components. Image from [17].

A geometric approach is often adopted to model fragmentation, treating nuclei as approximately spherical objects. Collisions are classified as *central* or *peripheral* depending on the impact parameter b. Central collisions involve extensive overlap of nucleons and frequently result in complete disintegration with isotropic emission of light fragments, whereas peripheral collisions dominate for larger b, producing a few fragments emitted predominantly in the forward direction, with velocities close to that of the primary projectile.

For heavy ions ($Z > 2$), these interactions are described with the *abrasion–ablation model*, which consists of a fast *abrasion* stage followed by a slower *ablation* stage [18] (Figure 1.7). During the abrasion phase, occurring on a timescale of $10^{-23} - 10^{-22}$s, the projectile and target nuclei partially overlap, forming a reaction zone. Nucleons in the overlapping zone are abraded and form the hot reaction zone (fireball), whereas the outer nucleons (spectators) are only slightly affected by the collision. In the subsequent ablation phase, with a timescale of $10^{-18} - 10^{-16}$s, the remaining projectile and target fragments as well as the fireball de-excite by evaporation of nucleons, light nuclei and emissions of gamma rays.

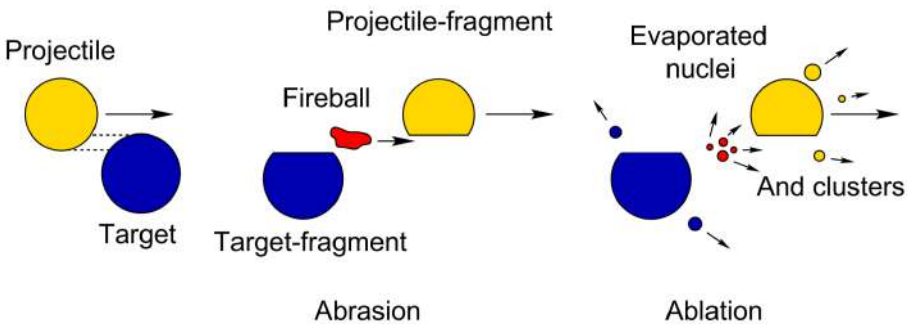

Figure 1.7: Simplified model of the nuclear fragmentation due to peripheral collisions of projectile and target nucleus. Image from [19].

Nuclear fragmentation plays a non-negligible role in CPT, affecting both the transport of the primary beam and the resulting energy deposition distribution.
Heavier projectile fragments retain a mass close to that of the primary ion and are emitted predominantly in the forward direction, with velocities comparable to the primary beam. In contrast, lighter fragments are emitted over a wider angular range, reaching angles up to 90°, and exhibit longer ranges due to their lower charge-to-mass ratio. The combined effect of these processes is a degradation of the sharpness of the characteristic depth–energy release distribution, with the deposition of an undesired dose beyond the Bragg peak and at larger lateral distances from the beam axis.
The emission of secondary fragments increases along the beam path, reaching a maximum near the Bragg peak position, and then decreases beyond it as the primary ions are fully stopped. Hydrogen and helium nuclei are produced most abundantly, while heavier fragments such as lithium, beryllium, and boron are roughly one order of magnitude less frequent.
Target fragments, which are present both in proton and heavy ion therapy, are characterized by short ranges (up to a few millimeters), which makes their experimental detection particularly challenging. As a consequence, their contribution is often not explicitly included in current treatment planning systems. These fragments predominantly deposit their energy in the entrance channel, leading to an unwanted energy deposition in healthy tissues upstream of the target.

Despite their negative impact on treatment planning, energetic secondary fragments may escape the irradiated medium and can therefore be exploited as detectable signals for *range monitoring*. This aspect represents the central physical motivation of the present work and will be discussed in detail in Sections 1.3.2 and 1.3.3.

1.2 Biological Effect of Radiation

In this section, we discuss the biological effects of ionising radiation, which are central to understanding radiation therapy. A quantitative description of these effects provides a framework for treatment planning, linking physical quantities such as energy deposition to biological outcomes in tissues.
The primary physical quantity used to quantify biological damage is the *absorbed dose*, defined as the energy deposited per unit mass of tissue and expressed in Gray [1 Gy = 1 J/kg], which has already been briefly mentioned in Section 1.1:

$$D = \frac{\mathrm{d}E}{\mathrm{d}m}\,. \tag{1.8}$$

The biological impact of a given absorbed dose depends on both the type of radiation and the tissue exposed. In order to account for these differences, the concepts of *equivalent dose* and *effective dose* have been introduced within the framework of *radiation protection*. The equivalent dose, denoted H_T, accounts for the different biological effectiveness of various types of ionizing radiation and is defined as

$$H_T = \sum_R w_R D_R\,, \tag{1.9}$$

where w_R is the radiation weighting factor for radiation type R, and D_R is the absorbed dose. The equivalent dose is expressed in Sievert (Sv).

The effective dose, E_T, further accounts for the different radiosensitivity of tissues and organs and is given by

$$E_T = \sum_T w_T H_T \,, \tag{1.10}$$

where w_T is the tissue weighting factor for each organ or tissue.
Standard values for these weighting factors are tabulated and periodically updated [20].

Biological effects of radiation are commonly classified into deterministic and stochastic outcomes. Deterministic effects appear above a certain dose threshold and manifest relatively soon after exposure; their severity increases with dose and includes phenomena such as skin reactions or organ damage. Stochastic effects, on the other hand, occur probabilistically, without a defined threshold, and may appear years after exposure. These include genetic mutations and cancers, where the probability of occurrence increases with dose, but the relationship is not immediate or deterministic.

1.2.1 DNA Strand Breaks

Ionising radiation can damage biological tissue primarily by inducing lesions in DNA, the most critical biomolecule for cellular function. This damage occurs through two main mechanisms: direct and indirect effects. In the case of direct effects, the radiation deposits energy directly within the DNA molecule, breaking the sugar-phosphate backbone. Such breaks can involve only one strand, resulting in a *single-strand break* (SSB), or both strands, leading to a *double-strand break* (DSB). Indirect effects arise when radiation deposits energy in the surrounding cellular environment, mainly water, producing reactive chemical species such as free radicals (reactive oxygen species). These radicals can diffuse and subsequently interact with DNA, causing SSBs and DSBs [21].
Cells possess multiple repair mechanisms to correct DNA damage [22]. Double-strand breaks are generally more challenging to repair than single-strand breaks. For instance, *homologous recombination* can accurately restore DSBs but is restricted to a precise phase of the cell cycle (the G2 phase), when DNA has already been duplicated [23]. The efficiency of DNA repair depends on the type and location of the damage along the DNA, as well as the cell cycle phase at the time of irradiation.
Figure 1.8 illustrates these mechanisms, showing direct energy deposition in DNA and indirect damage via reactive oxygen species.

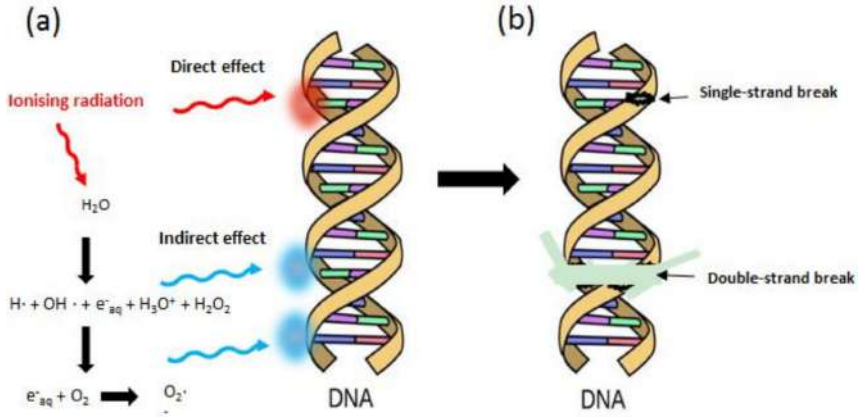

Figure 1.8: Mechanisms of DNA damage induced by ionising radiation: (a) direct deposition in DNA; (b) indirect damage via reactive oxygen species. Damage can result in single-strand breaks (SSBs) or double-strand breaks (DSBs) [24].

Understanding these processes is crucial in the context of hadrontherapy, where densely ionising particles produce complex DNA damage that is less easily repaired, enhancing the biological effectiveness of the treatment [24].

1.2.2 Survival Curve

In radiobiology, the *survival fraction* is a key quantity used to quantify the biological effect of a given radiation on cells. It is defined as the fraction of cells that retain their reproductive capacity after irradiation, plotted as a function of the absorbed dose.
Several models exist to describe cell survival, among which the *Linear-Quadratic (LQ) model* is widely adopted. Originally proposed by Chadwick and Leenhouts in 1973 [25], the model is based on the assumption that cell inactivation occurs primarily due to DNA double-strand breaks (DSBs). These DSBs can be induced either by a single radiation event affecting both DNA strands simultaneously (single-event DSB) or by two separate but closely spaced interactions (two-event DSB). The former process is linear with dose, as only one interaction is needed, whereas the latter is quadratic with dose, since two interactions are required [23].
Within the LQ formalism, the survival fraction $S(D)$ as a function of the absorbed dose D is expressed as

$$S(D) = e^{-\alpha D - \beta D^2}, \tag{1.11}$$

where the parameters α and β characterize the intrinsic radiosensitivity of the cells. The parameter α represents the linear component associated with single-event DSBs, while β quantifies the quadratic component linked to two-event DSBs [22]. Cells with higher values of α and β are more radiosensitive.
The shape of the survival curve reflects the balance between these two types of DNA damage. The linear term dominates at low doses, determining the initial slope of the curve, whereas the quadratic term produces a characteristic "shoulder" at intermediate doses, corresponding to sub-lethal damage that can be repaired by the cell. The ratio α/β is an important indicator of tissue radiosensitivity, providing a measure of the dose at which linear and quadratic damage contributions are equal. Tissues with a high α/β ratio (typically > 6 Gy), known as *early-responding tissues*, are more sensitive to radiation, while tissues with a low α/β ratio (1–4 Gy), called *late-responding tissues*, exhibit greater radioresistance [23].

1.2.3 LET

A key concept in radiobiology and dosimetry is the *Linear Energy Transfer* (LET), which quantifies the energy deposited per unit path length by ionising radiation in biological tissue. LET is closely related to the microscopic ionisation density along the particle track, and can be defined with respect to an energy threshold Δ, representing the minimum energy of *secondary electrons* produced by the primary radiation that are considered to contribute to local energy deposition and biological damage:

$$\mathrm{LET}_\Delta = \frac{\mathrm{d}E_\Delta}{\mathrm{d}x}, \tag{1.12}$$

where E_Δ is the energy deposited locally by electrons with energy below Δ. LET is expressed in units of keV/μm. This thresholded definition highlights that only the energy deposited by low-energy electrons contributes to the effective LET, whereas high-energy

electrons can travel farther and release their energy at more distant locations in the tissue. Radiation types are commonly classified as low-LET or high-LET according to the amount of energy released per unit length. Photons, electrons, and protons typically fall into the low-LET category, with values ranging from 0.2 to 2 keV/μm. Heavier ions, such as carbon ions, are high-LET radiations, with LET values in the range of 50–200 keV/μm. This difference arises because LET scales roughly with the square of the particle charge (Z_p^2), as predicted by the Bethe–Bloch formula for stopping power.
The biological relevance of LET is directly related to the density of ionisations along the track. High-LET particles generate densely ionising tracks that increase the probability of inducing critical DNA damage, such as double-strand breaks, which are challenging for the cell to repair. In contrast, low-LET radiation produces sparser ionisations, which tend to result in single-strand breaks that are more easily repaired. A schematic representation of the difference between low-LET radiation (in this case, proton) and high-LET radiation (in this case, carbon ion) track is shown in Figure 1.9, highlighting the higher density of secondary electrons produced by carbon ions and the resulting enhanced DNA damage.
The influence of LET on cellular survival can be observed in survival fraction curves. High-LET radiation produces steeper curves with smaller initial shoulders, indicating a greater effectiveness in inactivating cells at lower doses. This effect is reflected in the α parameter of the linear–quadratic model, which increases with LET. Consequently, high-LET particles, such as carbon ions, are more efficient at cell killing than low-LET radiation, supporting their use in targeted therapies such as hadrontherapy.

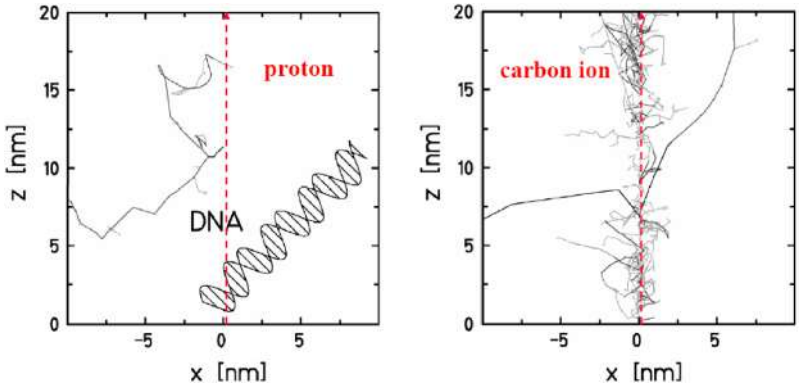

Figure 1.9: Comparison of a proton and a carbon track with a schematic representation of a DNA molecule. The trajectory of the primary particles is along z-axis. The higher density of the secondary electrons, produced by carbon ions, creates a large amount of clustered DNA damage. Image from [26].

1.2.4 Relative Biological Effectiveness

The *Relative Biological Effectiveness* (RBE) is a fundamental parameter used to quantify the radiobiological impact of different types of ionising radiation on a given biological system. It is defined as the ratio between the absorbed dose of a reference radiation, typically X-rays (D_{ref}), and the dose of the radiation under investigation (D_{test}) required to produce the same biological effect:

$$\text{RBE} = \frac{D_{\text{ref}}}{D_{\text{test}}}\bigg|_{\text{isoeffect}}. \tag{1.13}$$

Equal absorbed doses of different radiations do not produce the same biological outcomes.

For example, 1 Gy of carbon ions causes more extensive biological damage than 1 Gy of X-rays under the same conditions. To account for this, the concept of *Gray equivalent* (GyE) is introduced in hadrontherapy, which scales the absorbed dose by the RBE of the radiation:

$$D_{\mathrm{E}} = \mathrm{RBE} \times D_{\mathrm{absorbed}}, \tag{1.14}$$

where D_{E} is expressed in GyE. This allows the dose to be expressed in terms of its biological effect rather than purely its physical energy deposition.

RBE is commonly evaluated using *cell survival curves*. For two different radiations, the RBE can be estimated as the ratio of doses that result in the same surviving fraction, typically at 10% survival. However, RBE is not a fixed quantity: it depends on multiple factors, including the LET of the radiation, the total dose and fractionation scheme, cell cycle phase, tissue oxygenation, and dose rate.
In particular, there is a close relationship between RBE and LET. When RBE is plotted as a function of LET, it generally rises to a maximum around 100 keV/μm (Figure 1.10). This maximum corresponds to the optimal spacing of ionisation events for inducing DNA double-strand breaks, which occur over a distance of approximately 2 nm—the diameter of the DNA double helix. At this LET, energy deposition along the particle track is concentrated effectively to produce critical DNA damage. For LET values above 100 keV/μm, the probability of inducing DSBs remains high, but a portion of the energy does not contribute to further biological damage, leading to a decrease in RBE. This phenomenon is known as the *overkill effect*, reflecting the reduced efficiency of extremely densely ionising tracks.

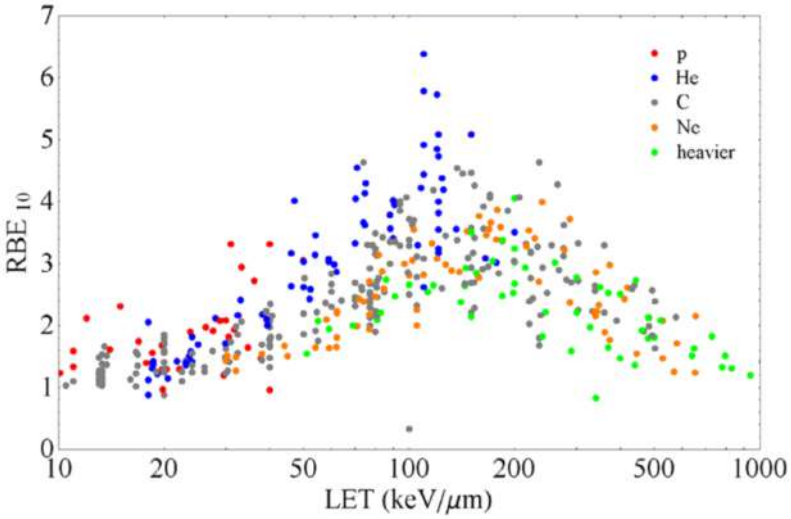

Figure 1.10: RBE relative to a fraction of 10% survival cell is plotted against LET for different ion species. Data taken from the PIDE database [27] related to in-vitro studies of cell survival [28].

Because LET and energy change along the particle path, RBE is depth-dependent in tissue. In heavy-ion therapy, where LET can exceed 100 keV/μm in the SOBP region, this variation is significant and must be accounted for in treatment planning. Accurate modeling of depth-dependent RBE is therefore essential for optimizing the SOBP to maximize tumor control while minimizing toxicity to healthy tissue.

1.2.5 Oxygen Enhancement Ratio

Another important factor affecting the biological effectiveness of ionising radiation is the oxygenation level of the irradiated tissue. Oxygen can amplify radiation-induced damage by reacting with free radicals produced during irradiation, thereby stabilizing DNA lesions and making them more difficult for the cell to repair. Conversely, tissues with low oxygen levels, such as many solid tumors, are more radioresistant. This phenomenon is quantified using the *Oxygen Enhancement Ratio* (OER), defined as the ratio of doses required to produce the same biological effect under hypoxic and aerobic conditions:

$$\mathrm{OER} = \left.\frac{D_{\mathrm{hypoxic}}}{D_{\mathrm{aerobic}}}\right|_{\mathrm{isoeffect}}. \tag{1.15}$$

OER plays a significant role for low-LET radiation; for photons, which are low-LET particles, the OER is approximately equal to 3. Consequently, the concentration of oxygen can strongly influence the extent of radiation-induced biological damage. In contrast, for high-LET radiation, the oxygen effect diminishes rapidly, approaching an OER value of 1. This behaviour arises because densely ionising tracks produce complex DNA damage that is less dependent on indirect, oxygen-mediated chemical processes. As a result, one of the main advantages of hadrontherapy is its increased effectiveness in the treatment of hypoxic, radioresistant tumors.

1.3 Range Monitoring

Hadrontherapy is a highly precise cancer treatment modality which allows for a conformal dose delivery to the tumour while sparing surrounding healthy tissues. However, this same characteristic makes hadrontherapy significantly more sensitive to range uncertainties than conventional photon radiotherapy. An inaccurate prediction of the particle range may lead to an under-dosage of the tumour and, simultaneously, to an over-dosage of healthy tissues beyond the target volume, potentially involving organs at risk (OARs).
To ensure optimal treatment outcomes, accurate Treatment Planning Systems (TPS) are essential. TPS combine patient imaging data with sophisticated dose calculation algorithms to predict the particle range and the resulting dose distribution within the patient. Despite continuous improvements in TPS accuracy, uncertainties remain due to factors such as patient mis-positioning, organ motion during the treatment, limitations in modelling tissue heterogeneities, and anatomical changes during different fractions of the treatment, which constitute the main focus of this thesis. Taken together, these factors can lead to a total uncertainty of the order of few millimeters in the actual position of the voxel being treated [29].
Consequently, range monitoring has emerged as a critical tool to complement TPS predictions (Section 1.3.1). Different strategies have been developed for different treatment beams. Here, the state of the art for range monitoring in proton therapy (Section 1.3.2) and carbon ion therapy (Section 1.3.3) will be presented.

1.3.1 Treatment Planning and Range Considerations

Accurate prediction of the beam range within the patient is a crucial requirement for treatment planning in hadrontherapy. The Treatment Planning System must account for all possible sources of range uncertainty. To standardize target definition and dose reporting in radiotherapy, the International Commission on Radiation Units and Measurements

(ICRU) introduced a set of reference volumes in Report 50 and Report 62 [30], defined as follows:

- **Gross Tumour Volume (GTV):** the macroscopic tumour volume identified by imaging;
- **Clinical Target Volume (CTV):** the GTV expanded to include regions of potential microscopic disease;
- **Internal Target Volume (ITV):** the CTV and an Internal Margin (IM), to take account of variations in size and position of the CTV;
- **Planning Target Volume (PTV):** a geometrical expansion of the CTV to ensure that the prescribed dose is actually deliverend in the CTV. It is often described as the CTV surrounded by a variable margin, named Safety Margin (SM), due to setup uncertainties.
- **Treated Volume (TV):** the volume enclosed by an isodose surface considered sufficient to achieve the therapeutic goal, often the 95% isodose;
- **Irradiated Volume (IV):** the volume receiving a dose level significant for normal tissue.

A schematic representation of these volumes is shown in Figure 1.11.

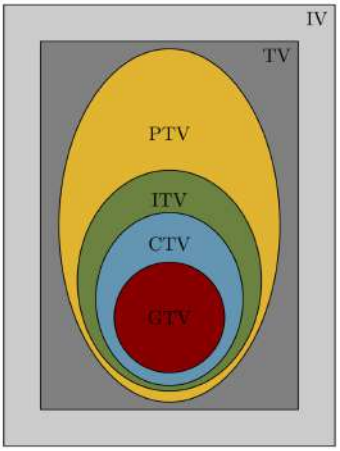

Figure 1.11: Anatomical regions defined by the Treatment Planning System.

Treatment planning involves multiple steps. Prior to treatment, the patient undergoes computed tomography (CT) and/or magnetic resonance imaging (MRI) to provide detailed anatomical information. These imaging data allow the oncologist to delineate the target volumes, which are then used by the TPS to compute the optimal treatment plan.
During this process, the TPS must account for several sources of uncertainty affecting the particle range, including CT calibration errors, conversion of Hounsfield Units (HU) to tissue density, patient misalignment, and organ motion such as respiration. To mitigate these uncertainties, safety margins of the order of a few millimetres are applied to the target volumes, ensuring adequate tumour coverage while sparing organs at risk within the treated anatomical region. However, fully exploiting the potential of particle therapy requires reducing these safety margins. Achieving this goal would necessitate an online monitoring of the treatment, providing direct information on the delivered dose during

irradiation and enabling, in the presence of significant deviations, treatment interruption and re-planning.
In hadrontherapy, treatments are typically fractionated, meaning that the prescribed dose is delivered over multiple sessions (fractions) across several days. Fractionation allows healthy tissues to recover and tumour tissues to reoxygenate, but it also makes accurate range prediction more critical, since anatomical variations between fractions may lead to deviations from the planned dose distribution. In selected cases, a control CT scan may be acquired during the course of treatment to assess anatomical changes. If these variations significantly affect the dose distribution, a re-planning of the treatment may be required. Currently, the decision to perform a mid-treatment control CT is often based on expected disease behaviour rather than on patient-specific information. This limitation highlights the need for range monitoring techniques capable of detecting morphological changes in a patient-dependent and objective manner. The ultimate goal is to provide real-time or near real-time information on the actual beam range, enabling informed decisions on treatment adaptation.
Two main approaches are typically distinguished: *inter-fractional monitoring*, which compares different fractions of treatment, and *on-line monitoring*, which verifies the range during beam delivery, allowing significant deviations to trigger immediate intervention.
Within both frameworks, range verification can rely on the detection of secondary radiation generated by the interaction of the primary beam with the patient. As the beam traverses the irradiated tissues, nuclear interactions lead to the production of secondary and tertiary particles (see Section 1.1.5) with sufficient energy to exit the body, making them suitable observables for range monitoring. The secondary emissions include:

- β^+ **emitters:** radioactive nuclei produced by projectile–target interactions undergo β^+ decay, emitting positrons that annihilate to produce 511 keV photons detectable by PET systems [31];
- **Prompt gamma rays:** nuclear interactions excite target nuclei, which de-excite almost instantaneously (less than 1 ns [32]), emitting photons with energies up to several MeV [33];
- **Charged fragments:** produced by nuclear fragmentation of primary ions with $Z > 1$ [34];
- **Neutrons:** generated through nuclear interactions between the incident beam and the target [35, 36].

For clinical applicability, a detector of secondary particles must meet several requirements: it should fit within the treatment room dimensions, comply with safety protocols, avoid interfering with the primary beam, introduce no additional dose to the patient, not increase treatment time, and provide a spatial resolution on the order of a few millimetres.

1.3.2 Range Monitoring in Proton Hadrontherapy

Since protons do not undergo projectile fragmentation, the most widely investigated approaches are based on the detection of β^+ emitters and prompt gamma radiation.

The production of β^+ emitting isotopes originates from nuclear reactions induced by the primary beam interacting with target nuclei, including fragmentation and excitation processes. These radioactive nuclei decay via β^+ emission, producing positrons that annihilate with electrons and generate pairs of 511 keV photons. These photons can be detected by

PET systems, enabling the reconstruction of the spatial distribution of the activated isotopes inside the patient.
As shown in Figure 1.12, the distribution of β^+ activity is correlated with the absorbed dose and, consequently, with the primary proton range: the activity is observed along the proton path, reaching a maximum just upstream of the Bragg peak and rapidly decreasing beyond it, reflecting the sharp fall-off of dose deposition.

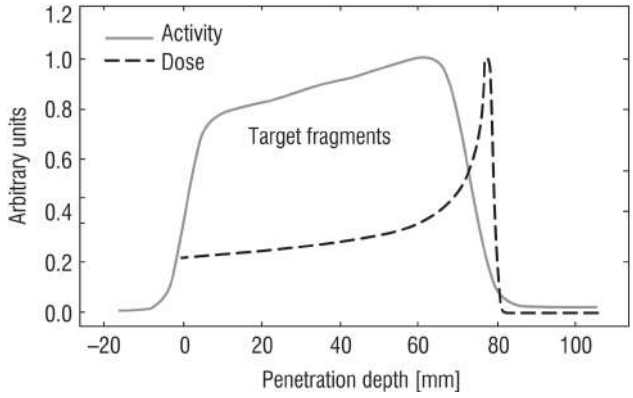

Figure 1.12: In-beam PET measurements of β^+ activity depth profiles (solid line) for proton irradiation of PMMA (Polymethyl Methacrylate) targets at 110 MeV. The dashed line shows the corresponding calculated dose distributions. The pattern of activation is due to positron-emitting target fragments. Image from [31].

Range monitoring based on β^+ emitters can be implemented according to different acquisition modalities:

- **Offline monitoring:** PET acquisition is performed in a separate room after treatment delivery [37–40]. This approach is limited by metabolic washout, a biological process that redistributes and eliminates radioactive isotopes, thereby reducing the correlation between measured activity and delivered dose.
- **In-room monitoring:** the PET system is installed in the treatment room, and the patient is positioned immediately after irradiation [40]. While this reduces the acquisition delay, washout effects are only partially mitigated. Moreover, the treatment room cannot be used during image acquisition, negatively impacting clinical throughput.
- **In-beam monitoring:** PET detectors are integrated with the beam delivery system, enabling data acquisition during and immediately after irradiation. This configuration further reduces washout effects but introduces additional challenges related to the high background during beam delivery and to the integration of the detection system within the treatment room [41, 42].

A comparative discussion of these techniques is presented in [43].

The alternative strategy exploits prompt gamma radiation. Prompt gamma photons are emitted almost immediately following the nuclear excitation of target nuclei by the primary beam, with photon energies ranging from 1 to 10 MeV [44, 45]. Their spatial distribution closely follows the dose profile, with a fall-off near the Bragg peak, as shown in Figure 1.13. Prompt gamma monitoring offers several advantages over β^+-based techniques. Owing to their extremely short emission times, prompt gamma rays are not affected by metabolic

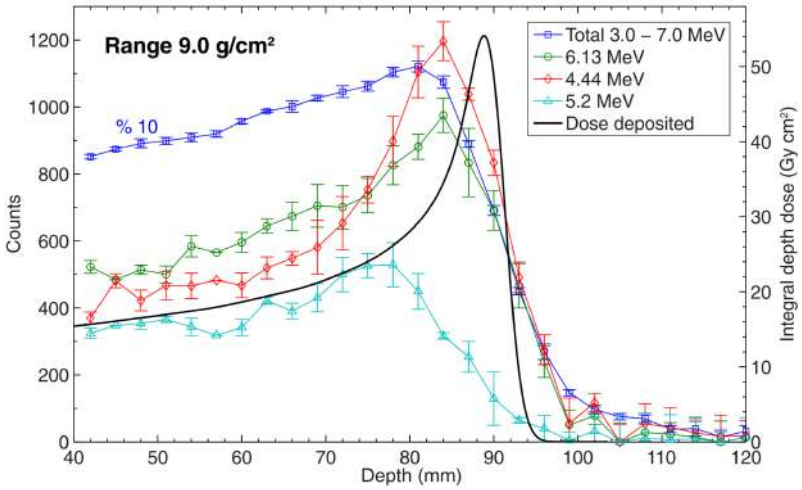

Figure 1.13: Energy-integrated (□) and discrete (○, ◇, △) prompt gamma emissions along proton pencil-beams in water. Mean and $\pm 1\sigma$ statistical uncertainty of five measurements with 10^{10} incident protons per point are shown. The black line represents the clinically commissioned depth-dose curve. Image from [46].

washout, and their nearly isotropic emission enables detection without the need for a full-ring geometry. However, their broad energy spectrum prevents the use of conventional SPECT (Single Photon Emission Computed Tomography) systems, requiring instead dedicated detection solutions. These would involve heavier and bulkier absorbers, which introduce constraints related to detector size, weight, and encumbrance, often at the expense of detection efficiency and spatial resolution. Furthermore, the presence of secondary neutrons and uncorrelated photons contributes significantly to the background, leading to a degradation of the achievable spatial resolution.
To address these challenges, several prompt gamma detection techniques have been proposed:

- **Mechanical collimation:** systems using pinholes or slits suppress background and achieve millimetric range resolution [47].
- **Compton cameras:** reconstruct the incoming photon direction via Compton scattering in a scatterer and absorber, enabling 3D reconstruction and partial background rejection, at the cost of system complexity [48].
- **Non-imaging systems:** rely on timing or spectral information, such as Time-of-Flight (TOF) measurements or energy spectra. Prompt Gamma Timing (PGT) exploits the correlation between TOF and Bragg peak depth.

1.3.3 Range Monitoring in Carbon Ion Hadrontherapy

Beyond the range monitoring methods discussed for proton therapy, carbon ions provide an additional and particularly promising channel: the detection of secondary charged fragments produced by the nuclear fragmentation of the primary beam. Secondary charged fragments are also produced in proton therapy via target fragmentation. However, in proton treatments, these fragments typically have kinetic energies of only a few MeV and ranges of a few micrometers to at most a few tens of micrometers, preventing them from exiting the patient and making their detection impractical. In contrast, fragments

from carbon ion beams can retain velocities comparable to the primary ions, with kinetic energies exceeding 100 MeV, allowing them to traverse the patient and reach external detectors. A fraction of these secondaries, however, still stops within the patient, reducing the overall detection efficiency.
Although secondary fragments are mainly emitted in the forward direction, carbon ion beams also produce significant emissions at large angles (typically 60°–90°). Fragments consist primarily of protons and neutrons, which can be efficiently discriminated, resulting in a relatively low background—one of the main advantages of this monitoring approach. Figure 1.14 shows the emission profiles of secondary fragments produced by a 400 MeV/u carbon ion beam in a 35 cm water phantom at GSI [49], highlighting that protons are the most abundant species and the only ones with significant emission at angles larger than 10°.

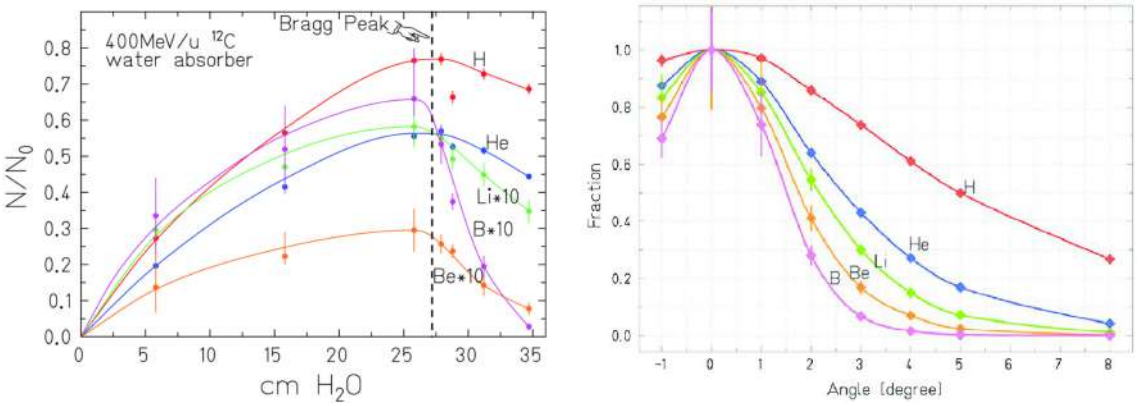

(a) (b)

Figure 1.14: Left: fraction of secondary fragments produced by a 400 MeV/u carbon ion beam in a water phantom as a function of depth. Right: relative angular distribution of the same secondary fragments. Values for Li, B, and Be are multiplied by 10 for clarity. Images from [49].

Since the emission intensity of secondary fragments is correlated with the position of the Bragg peak, these charged fragments can be exploited for range monitoring. To evaluate the feasibility of range monitoring in carbon-ion therapy, several experimental studies have measured the flux of charged secondary fragments produced by carbon-ion beams in tissue-equivalent targets. Such measurements were conducted at multiple ion-beam facilities, including GSI Helmholtzzentrum für Schwerionenforschung (GSI) [50, 51], the Laboratori Nazionali del Sud (LNS) [52], and the Heidelberg Ion-Beam Therapy Center (HIT) [53], using fully stripped carbon-ion beams with energies ranging from 80 to 220 MeV/u. In these experiments, multi-plane drift chambers (DC) were employed to reconstruct the trajectories of emitted secondary fragments, while arrays of LYSO scintillators measured their deposited energy. The experimental setup implemented at LNS is shown in Figure 1.15.
These studies confirmed that a significant fraction of secondary charged fragments exits the target with sufficient energy to be detected externally, demonstrating the potential of this channel as a real-time, patient-dependent observable for range verification in carbon ion therapy.
By back-tracking reconstructed trajectories, the emission profile of secondary protons along the beam axis (x_{PMMA}) can be obtained. Figure 1.16a shows such a profile together with the absorbed dose distribution calculated via Monte Carlo simulations. The

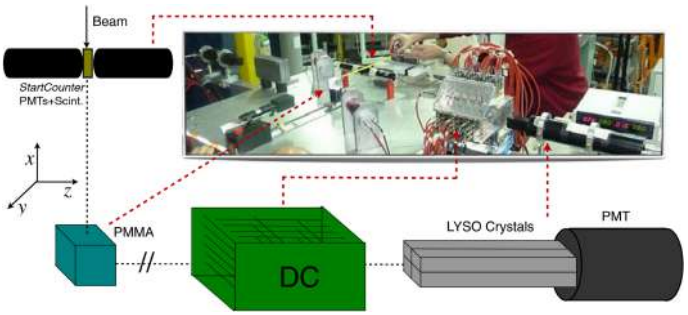

Figure 1.15: Experimental setup used for the measurement of the flux of charged secondary particles produced by the interaction of a 70 MeV/u fully stripped carbon ion beam with a PMMA target at LNS [52].

profiles are anti-correlated [50]: at shallow depths, the primary beam loses little energy, producing a low absorbed dose but high-energy secondaries that can escape and reach the detector. At greater depths, energy loss reduces both the energy and escape probability of secondaries, limiting sensitivity near the Bragg peak.
This behaviour represents an intrinsic limitation of charged secondary monitoring: low statistics near the Bragg peak reduce sensitivity to dose variations. Additional factors affecting spatial resolution include multiple Coulomb scattering (see 1.1.4) and re-absorption of secondaries within the patient.
Finally, variations in material density along the beam path significantly influence the spatial distribution of secondary fragments. Figure 1.16b shows that peaks in the secondary emission profile correspond to regions of PMMA, demonstrating sensitivity of this technique to density heterogeneities.

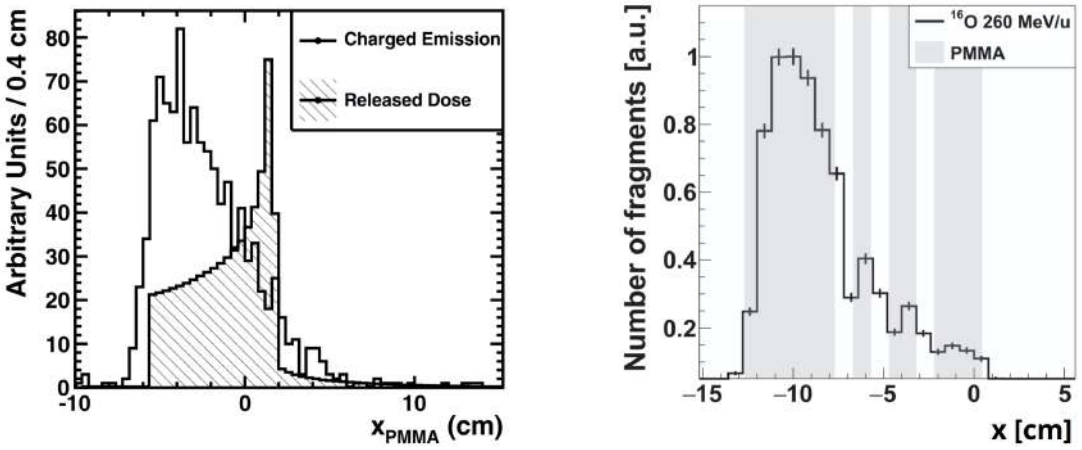

(a) (b)

Figure 1.16: Left: Depth profile of secondary proton emission (solid line) compared with Monte Carlo simulated absorbed dose (dotted line). Image from [50]. Right: Correlation between secondary fragment production and material density along the beam path. Image adapted from [53].

It is within the context of range monitoring using secondary fragments that the present thesis work is positioned, and its details will be discussed in the following chapters.

Chapter 2

The MULTIPASS Project

Despite the well-established physical advantages of Charged Particle Therapy (CPT), discussed in Sections 1.1 and 1.2, these benefits are not yet fully exploited in clinical practice. In particular, beam range uncertainties are still widely regarded by the medical physics community as one of the main obstacles to the widespread adoption of CPT.
As discussed in Section 1.3, discrepancies between the planned and the actual position of dose deposition may arise from several sources, leading to an overall range uncertainty of the order of a few millimetres [4]. To account for these uncertainties, the Treatment Planning System (TPS) introduces conservative safety margins around both the tumour volume and the surrounding Organs at Risk (OARs). Reducing these margins is of great importance to limit unnecessary irradiation of healthy tissues and to decrease the probability of radiation-induced secondary malignancies, especially in patients with a long life expectancy.
Another crucial aspect for improving the efficacy and safety of CPT treatments concerns the characterization of the neutron radiation produced by the interaction between the therapeutic beam and patient tissues [54]. Neutrons, due to their lack of electric charge, can propagate over relatively large distances before interacting and therefore represent one of the main contributors to the development of secondary malignant neoplasms far from the target volume [55]. A detailed characterization of the neutron background, in terms of fluence, energy spectrum, and angular distribution, is thus of paramount importance for both treatment optimization and radiological protection.

The state-of-the-art techniques currently employed for monitoring the absorbed dose distribution in proton and carbon-ion treatments have been described in Sections 1.3.2 and 1.3.3. Despite the progress achieved so far, the development of reliable monitoring techniques capable of detecting and exploiting the different components of secondary radiation remains a crucial step toward improving the overall clinical effectiveness of CPT.
In ion-based CPT, secondary radiation emitted as a consequence of nuclear interactions between the primary beam and patient tissues can be exploited to infer information on the dose deposition [34, 56, 57]. In this context, studies performed with the Dose Profiler within the INSIDE (INnovative Solution for In-beam DosimEtry in hadrontherapy) collaboration [58, 59] demonstrated the feasibility of using secondary charged particles for inter-fractional monitoring in carbon ion therapy. At the same time, these studies highlighted several intrinsic limitations of the implemented detector, including its relatively large distance from the patient, limited solid angle coverage, and restricted rate capability, which significantly constrained the achievable performance of the system.
Within this framework, the PRIN (Progetti di Rilevante Interesse Nazionale) MULTIPASS (MULTIPle trAcker for Secondary particleS monitoring) project aims to develop,

construct, and validate a compact monitoring detector specifically designed for CPT applications. The system is intended to detect secondary protons and prompt-γ radiation, enabling inter-fractional range monitoring and the identification of morphological changes in the treated region between different treatment sessions for both proton and carbon-ion therapies, while also contributing to the characterization of neutron-induced background radiation.

In this chapter, Section 2.1 first provides a brief description of the Dose Profiler detector, as one of the objectives of this thesis is to compare its performance with that of the MULTIPASS detector. The MULTIPASS project, which constitutes the primary focus of this thesis, is then presented in Section 2.2.

2.1 The Dose Profiler Detector

As discussed in Section 1.1.5, the interaction of a ^{12}C therapeutic beam with patient tissues leads to a significant production of secondary charged fragments as a result of nuclear fragmentation processes. These fragments, which include protons and light ions, are characterized on average by a lower stopping power than the primary carbon ions and consequently exhibit a longer range in matter. Although nuclear fragmentation represents an effect that must be carefully modeled within the TPS due to its impact on dose distributions, it also provides an opportunity for beam range monitoring.
In particular, high-energy secondary protons emitted during carbon-ion irradiation can exit the patient's body and be detected at relatively large angles with respect to the incident beam direction [17, 19, 50, 53]. This feature makes them suitable candidates for on-line and inter-fractional monitoring of the treatment [34, 56, 57]. Pioneering experimental studies in this field were carried out within the INSIDE (INnovative Solution for In-beam DosimEtry in hadrontherapy) project [28, 60], whose objective was the development of novel technologies capable of identifying inter-fractional anatomical variations by exploiting the spatial emission profile of secondary radiation.

The INSIDE system is based on a bimodal approach. It includes two PET detectors for the measurement of annihilation photons in proton therapy [61], as well as a dedicated device for carbon-ion treatments, known as the Dose Profiler (DP) [62], specifically designed to detect secondary charged fragments.
The DP consists of eight square detection planes, each with a lateral size of 19.2 cm, arranged along the beam axis with a spacing of 2 cm. Each plane is composed of two perpendicular layers of square plastic scintillating fibers with a cross section of 500 $\times$ 500 µm^2, providing one coordinate measurement per layer (x and y) and allowing for the reconstruction of charged-particle tracks from the energy deposits in both layers. The detector is currently installed in treatment room 1 at the CNAO (Centro Nazionale di Adroterapia Oncologica) facility in Pavia, at a distance of approximately 50 cm from the treatment isocenter. Figure 2.1 shows, on the left, a schematic view of the DP, highlighting the alternating planes composed of two perpendicular layers of fibers. On the right, an image of the detector during the assembly phase.

Clinical data collected with the Dose Profiler at CNAO demonstrated the feasibility of using secondary charged particles for treatment monitoring, showing the capability of the system to identify potential inhomogeneities in some treated patients [58, 59]. However, these studies also highlighted several intrinsic limitations of the DP design. First, the detector is positioned at a fixed location, relatively far from the patient ($\approx$ 50 cm), which

restricts its adaptability to different treatment geometries and limits the solid angle subtended by the active area. In addition, the system is relatively bulky and heavy, making handling, positioning, and maintenance more challenging. Finally, the maximum sustainable particle rate, of the order of 100 kHz, is insufficient to efficiently track the flux of secondary particles originating from regions where the carbon-ion dose is predominantly delivered.

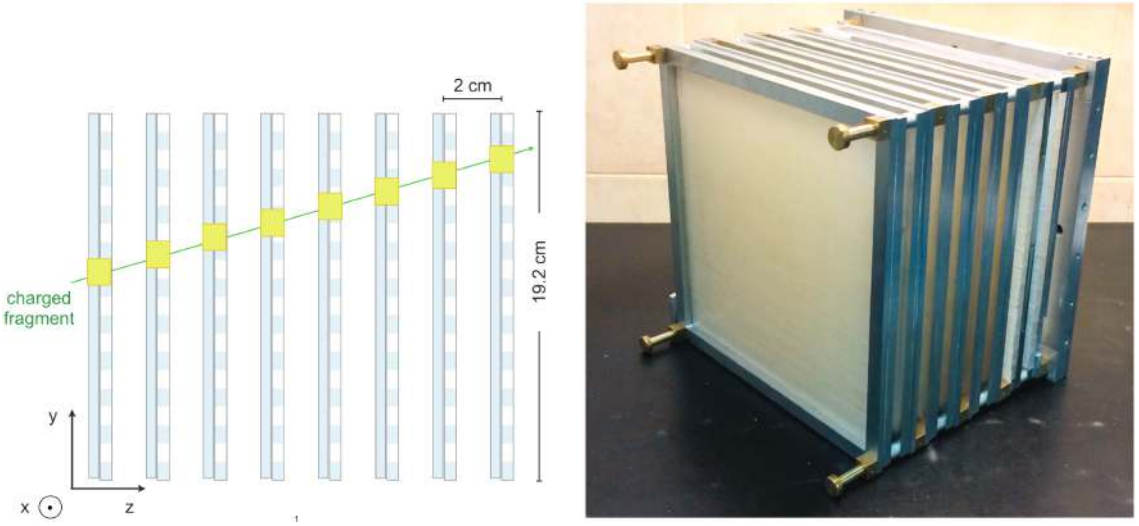

(a) (b)

Figure 2.1: Left: schematic view of the Dose Profiler, illustrating the fragments detection principle. The yellow squares identify the energy released in the fibres layers (in azure), whereas the particle trajectory is shown in green. Right: view of the Dose Profiler layers during the assembly phase showing the fibre layers. Images from [62].

2.2 The MULTIPASS Detector

With regard to the detection of charged secondary protons, which is the primary focus of the present work, the MULTIPASS detector is designed to overcome some of the practical constraints associated with the Dose Profiler. Its compact and versatile design allows for easy repositioning and placement closer to the patient, increasing geometrical acceptance and providing greater flexibility for different clinical configurations. Technological improvements in both the detector and the read-out electronics are expected to significantly enhance the collectable statistics, enabling operation at particle rates up to approximately 500 kHz.

Beyond proton detection, MULTIPASS is also specifically designed to study prompt-γ radiation by exploiting pair production [63], as developed within the PAPRICA (PAir PRoduction Imaging ChAmber) project [64], which demonstrated the feasibility of this approach for in-beam monitoring.

Additionally, the detector incorporates strategies previously explored in the MONDO project [65] for tracking neutron radiation produced by the interaction of the therapeutic beam with patient tissues. The MONDO (MOnitor for Neutron Dose in hadrOntherapy) project aimed to design a detector capable of characterizing neutron radiation in order to minimize tissue toxicity and the risk of secondary tumors, while distinguishing neutrons generated within the patient from those resulting from interactions of secondary particles

with the surrounding environment.

Section 2.2.1 describes the structure of the simulated detector, while Section 2.2.2 presents the design of the read-out electronics, which is still under development.

2.2.1 The Structure of the Detector

So far, studies on MULTIPASS have been conducted using a prototype similar to the one simulated in this work but with smaller dimensions ($5 \times 5 \times 2$ cm^3). The prototype employs the same type of scintillating fibers as the detector considered here, but in a reduced number and arranged in fewer detection planes. The prototype is shown in Figure 2.2.

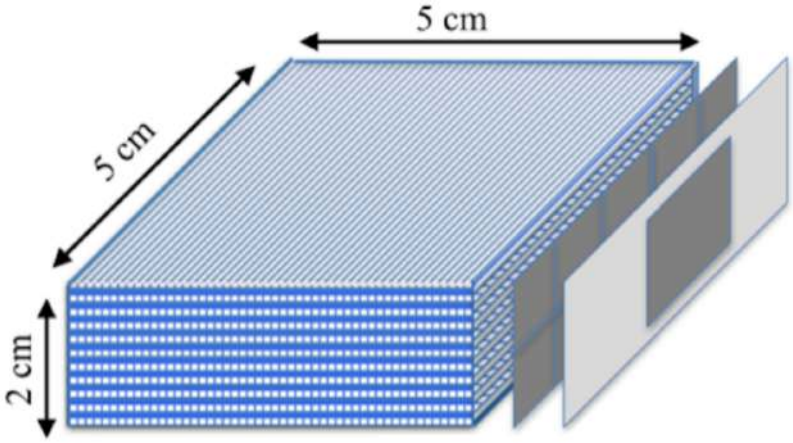

Figure 2.2: Sketch of the MULTIPASS prototype studied so far. The detector considered in this thesis has the same structure and components, but larger dimensions, with a total volume of $10 \times 10 \times 20$ cm^3.

Building on this prototype, the detector simulated in the present work represents a scaled-up version of MULTIPASS, designed to improve tracking capabilities and detection efficiency. It consists of 363 planes of squared plastic scintillating fibers, each 10 cm long and with a side length of 250 µm. The fibers are made of EJ-200 (polyvinyltoluene), resulting in a total active volume of $10 \times 10 \times 20$ cm^3. Each plane is composed of two adjacent fiber layers arranged in orthogonal directions, providing the x and y coordinates of the detected interactions, while the z coordinate along the detector axis is defined by the position of the fiber plane centers. Each fiber layer contains 400 fibers (200 in direction x–z and 200 in direction y–z), resulting in an active area of 10×10 cm^2 per plane. Mylar spacers with a thickness of 50 µm are placed between the two layers of each plane, as well as at the entrance and exit of the detector. Figure 2.3 shows the detector in the x–z plane, together with a zoomed-in view of a portion of the first five planes to highlight the fine structure of the simulated detector. The view in the y–z plane is analogous.

This detector layout is well suited to the monitoring tasks mentioned above. On the one hand, it enables accurate three-dimensional reconstruction of prompt-photon trajectories through pair-production mechanisms; on the other hand, it allows efficient tracking of secondary protons generated either by ion-beam nuclear fragmentation or by neutron double elastic scattering processes. The chosen fiber thickness provides sufficiently fine granularity to reconstruct both proton tracks and electron–positron pairs with high spatial resolution, while simultaneously ensuring the measurement of the deposited energy.

The choice of plastic scintillating material plays a crucial role in the detector performance. Owing to its high hydrogen content, it enhances the probability of proton production via elastic neutron scattering, which is particularly advantageous for neutron detection. At the same time, the low atomic number of the material reduces multiple Coulomb scattering of electron–positron pairs, thereby improving the reconstruction accuracy of prompt-photon trajectories. This choice, however, comes at the cost of a reduced pair-production yield, due to the relatively small pair-production cross section of prompt photons in the energy range of approximately 1–10 MeV when interacting with low-Z materials.

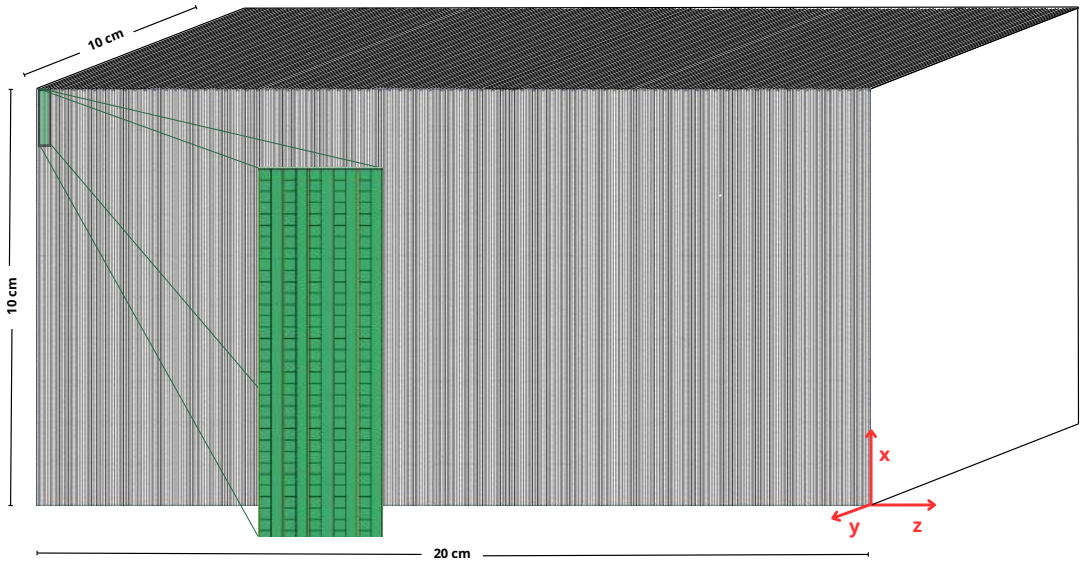

Figure 2.3: View of the simulated MULTIPASS detector in the x–z plane. A zoom of the first five detection planes highlights the fine segmentation of the fibers and the layered structure of the detector: the alternation of scintillating fiber layers oriented along the x and y direction and thin mylar spacer layers is visible. The structure in the y–z view is analogous.

2.2.2 The Read-out System

The adoption of scintillating fibers provides the compactness and tracking capabilities required to detect the various physical processes relevant to the MULTIPASS project. At the same time, this choice poses significant challenges from the perspective of the read-out electronics. In particular, the system must be capable of single-photon sensitivity, as the expected number of optical photons produced per unit energy deposition in a single fiber is of the order of 1–5 photons/MeV. Preserving the intrinsic granularity of the detector while sustaining high particle rates is therefore essential in order to maximize the collected statistics.

To meet these requirements, the read-out electronics must rely on a dedicated, fully digital architecture, tightly integrated with the sensor substrate to maintain the overall compactness of the device. A suitable technological solution is provided by the SBAM (SPAD-Based Acquisition for the MONDO experiment), originally developed by Fondazione Bruno Kessler (FBK, Trento) in collaboration with the Centro Ricerche “Enrico Fermi” (CREF, Rome) for the MONDO experiment [65]. The SBAM technology is based on the use of

Single Photon Avalanche Diodes (SPADs), semiconductor photodetectors implemented using CMOS (Complementary Metal–Oxide–Semiconductor) technology.
SPADs consist of highly doped p–n junctions operated above the breakdown voltage. When a photon is absorbed in the junction, it generates an electron–hole pair that is accelerated by the strong internal electric field toward the electrodes. During this process, ionization occurs, triggering an avalanche multiplication that results in a macroscopic electrical signal. This signal can be directly acquired by the read-out system and stored in digital form. The avalanche process is quenched by temporarily switching off the electric field, thereby restoring the detector to its initial operating conditions.
At present, the electronics architecture is being adapted to the specific requirements of the MULTIPASS detector, including the development of trigger logic, event selection algorithms, and background rejection strategies. Owing to its high sensitivity, scalability, and compatibility with compact detector layouts, the SBAM technology represents a particularly promising solution for the read-out of scintillating-fiber–based systems and constitutes a solid foundation for the MULTIPASS project.

Chapter 3

Monte Carlo Simulation of a Treatment Plan

The objective of this thesis is to assess the capability of the MULTIPASS system to detect morphological changes in patients treated with carbon-ion therapy by exploiting the emission profiles of protons emitted as secondary fragments.
As discussed in the previous sections, morphological variations along the path of the primary ions can modify their range and, consequently, lead to unexpected dose deposition compared to the treatment plan. This may result in potential damage to healthy tissues and inadequate dose delivery to the tumor volume. Therefore, identifying morphological changes occurring between successive treatment fractions is of primary importance. The ultimate goal is to provide radiation oncologists with a non-invasive, patient-specific monitoring tool capable of indicating whether a morphological change has occurred. This information can subsequently be used to determine whether a control CT scan is needed to adapt the treatment plan.

A further objective of this thesis is to compare the performance of MULTIPASS with that of the Dose Profiler detector, described in Section 2.1. The latter was developed within the INSIDE project and is currently installed in treatment room 1 at the CNAO facility in Pavia. Both detectors were designed with the same clinical aim of monitoring particle therapy treatments. For the Dose Profiler, both experimental data acquired during a clinical trial started in August 2019 and Monte Carlo simulations of some patient cases are available. To this end, the Monte Carlo study presented in this thesis has been constructed using data from one of the patients enrolled in the INSIDE clinical trial (ClinicalTrials.gov Identifier: NCT03662373), who had already been analyzed using the Dose Profiler system [66].

The selected patient was treated with carbon-ion therapy and underwent a control CT scan at mid-treatment. The availability of this additional imaging allows for the investigation of inter-fractional morphological changes, enabling the simulation of the treatment at mid-fraction, and provides a valuable reference for assessing the sensitivity of the monitoring system under study. The simulation, performed using the FLUKA Monte Carlo code, was configured so that the MULTIPASS detector reproduces the same spatial positioning and angular acceptance as the Dose Profiler employed in the corresponding clinical study. This setup enables a direct and consistent comparison of the detector performances.

In this chapter, following a brief introduction to FLUKA in Section 3.1, the selected patient and the simulation geometry are described in Sections 3.2 and 3.3.

3.1 FLUKA Monte Carlo Code

FLUKA (*FLUktuierende KAskade*) is a fully integrated Monte Carlo code for the simulation of particle transport and interactions with matter over a wide range of energies and particle types [67–70]. FLUKA finds applications in a broad spectrum of fields, including elementary particle physics, radiation protection, particle detector design, cosmic-ray physics, dosimetry, and medical physics, with particular relevance to radiotherapy. It has been developed through a collaboration between the European Organization for Nuclear Research (CERN) and the Istituto Nazionale di Fisica Nucleare (INFN), and it is continuously improved through the incorporation of advanced theoretical models and thorough benchmarking against experimental data. Figure 3.1 provides a schematic overview of the interactions implemented in FLUKA.

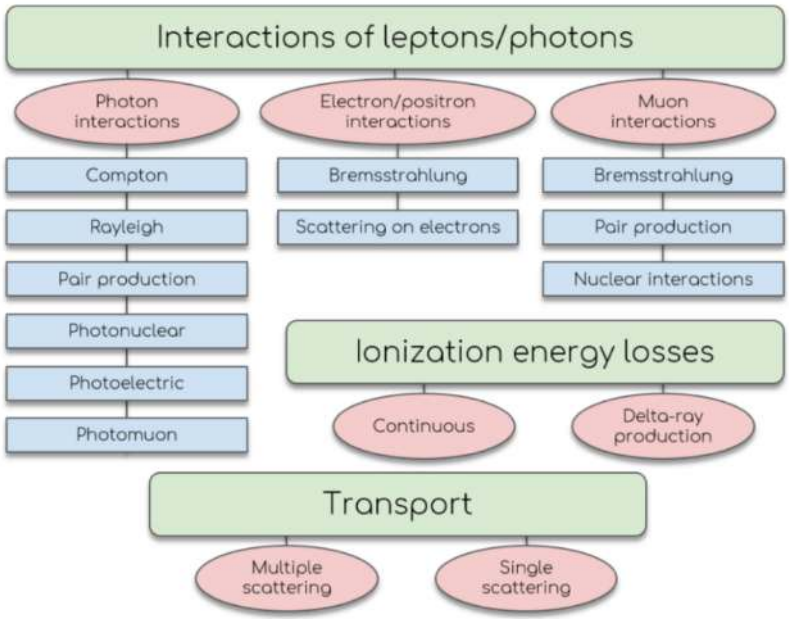

Figure 3.1: Summary of the electromagnetic interactions implemented in FLUKA [71].

In FLUKA, the geometry of the experimental setup is defined using simple shapes, such as parallelepipeds, spheres, and similar objects, referred to as *bodies*, which can be combined to form more complex structures known as *regions*. Each region is uniquely identified by a name and is assigned a specific chemical element or compound.
The simulation of the beam is organized in terms of *events*. Each generated beam particle defines a single event, which includes the particle's creation, its transport through the setup, any interactions it undergoes within the target, and all resulting final-state products, including secondary fragments and decay products, along with their interactions with the detection system.
A key concept for tracking charged particles in FLUKA is the *hit*, which represents the energy ΔE lost by a particle during a single step within a detector element; in the present study, the fundamental detector elements are the fibers.
For the simulation performed in this study, the raw data are saved in a customized output format and organized into three main structures:

- **Particle block:** Contains the kinematic information and intrinsic properties of all particles generated in the event.

- **Detectors block:** Stores all recorded hits for each fiber, including energy deposition, position, and momentum. Each hit is linked to the particle that generated it through a pointer, creating a direct connection between detector signals and particle tracks.
- **Crossings block:** A *crossing* occurs whenever a particle passes from one region of the geometry to another. For each crossing, the position, particle momentum, and a pointer to the corresponding particle are recorded.

Using FLUKA, a treatment plan can be simulated by carefully defining the geometry of the treatment room, reproducing the accelerator nozzle, the detector structure, and incorporating both the beam parameters of the treatment plan and the patient CT data. FLUKA provides a built-in function to automatically convert CT image data into the corresponding tissue densities using calibration coefficients. For the primary treatment beam, each individual pencil beam is simulated using the energy, position, and number of particles provided by the treatment facility's Dose Delivery System (DDS).

The FLUKA graphical interface FLAIR (FLUKA Advanced Interface) [72] allows the 3D visualization of the simulation geometries, including patient CT data and the detector. Once the simulation is completed, the FLUKA output is converted into a `ROOT` [73] file, which serves as input for the C++ analysis code described in the following chapter.

3.2 Patient Overview

The selected patient is affected by intestinal-type adenocarcinoma (ITAC), a malignant tumor originating in the nasal cavities. The prescribed treatment plan consists of 16 fractions of carbon-ion irradiation, delivering a total dose of 65.6 GyE (approximately 4.1 GyE per fraction).

For each treatment fraction, the patient is irradiated from different primary beam directions, referred to as *fields*. The therapeutic beam is delivered by the *Dose Delivery System* (DDS), which controls extraction, transport, and irradiation parameters. Its final section, the *beam nozzle*, located immediately upstream of the patient, hosts devices for beam shaping, monitoring, and safety, including ionization chambers that continuously measure the number of delivered particles as well as the beam position and size in real time, ensuring accurate and reproducible dose delivery. While the beam trajectory is fixed, irradiation from different angles is made possible by the Patient Positioning System (PPS), which consists of a carbon-fiber couch repositioned by a robotic arm in a plane parallel to the ground. The angular convention is defined such that an angle of 0° corresponds to the beam entering the patient from the left side, while 270° corresponds to the patient being aligned along the beam direction, with the beam incident from the cranial side. During treatment, the patient is immobilised using a thermoplastic mask, individually designed during the preliminary treatment planning phase. The mask is placed on the couch and must be worn throughout irradiation to ensure reproducible positioning. A set of optoelectronic markers is integrated into the mask and detected by the Optical Tracking System (OTS) [74], which consists of three infrared cameras and allows verification of patient positioning both before and during treatment.
Figure 3.2 illustrates the main components of Treatment Room 1 at CNAO, as well as the positioning of the couch for the 270° configuration.
In the considered treatment plan, the patient is irradiated from three distinct directions, with the parameters summarized in Table 3.1.

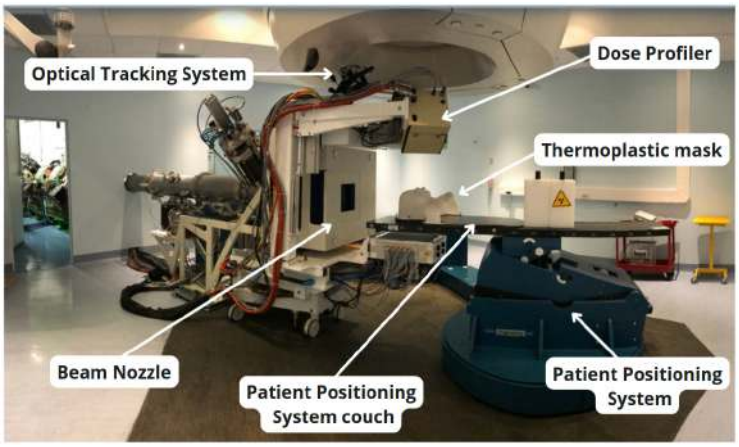

Figure 3.2: View of Treatment Room 1 at CNAO with the couch positioned at 270°. Image adapted from [75].

Field	Irradiation Angle (°)	Number of Primary Particles
B1	15	7.41×10^8
B2	195	7.15×10^8
B3	**270**	$\mathbf{5.98 \times 10^8}$

Table 3.1: Parameters of the irradiation fields prescribed in the treatment plan.

In the present work, only field B3 is considered, as this irradiation geometry is particularly favourable for the detection of charged secondary fragments. Indeed, the sensitivity to morphological changes is expected to depend on both the incoming beam direction and the tumour location, since secondary particles may pass through varying amounts and types of tissue before exiting the patient.

The planning CT of the patient was acquired approximately 20 days prior to the delivery of the first treatment fraction. Given the expected morphological changes associated with the treated pathology, a control CT scan was scheduled at mid-treatment, corresponding to the seventh treatment fraction.
The two CT scans were co-registered to ensure proper alignment, enabling the assessment of morphological variations. This procedure had been performed in previous studies on the same patient using the 3D Slicer software [76, 77]. The alignment was achieved through rigid roto-translations with six degrees of freedom, using cranial bone structures as the reference.
A comparison between the planning CT and the control CT reveals two distinct morphological changes, as highlighted in Figure 3.3. The first change is located in the tumor region (left panel), while the second, smaller in spatial extent but still clearly identifiable, is indicated by the yellow circles in the right panel.

The observed variations between the planning CT and the control CT are quantified in terms of tissue density using Hounsfield Units (HU). HU are defined as a linear transformation of the linear attenuation coefficient μ of a material relative to the radiodensity of distilled water at standard temperature and pressure, which is set to 0 HU, while air under the same conditions is defined as -1000 HU. For a voxel with linear attenuation coefficient μ, the corresponding HU value is calculated as:

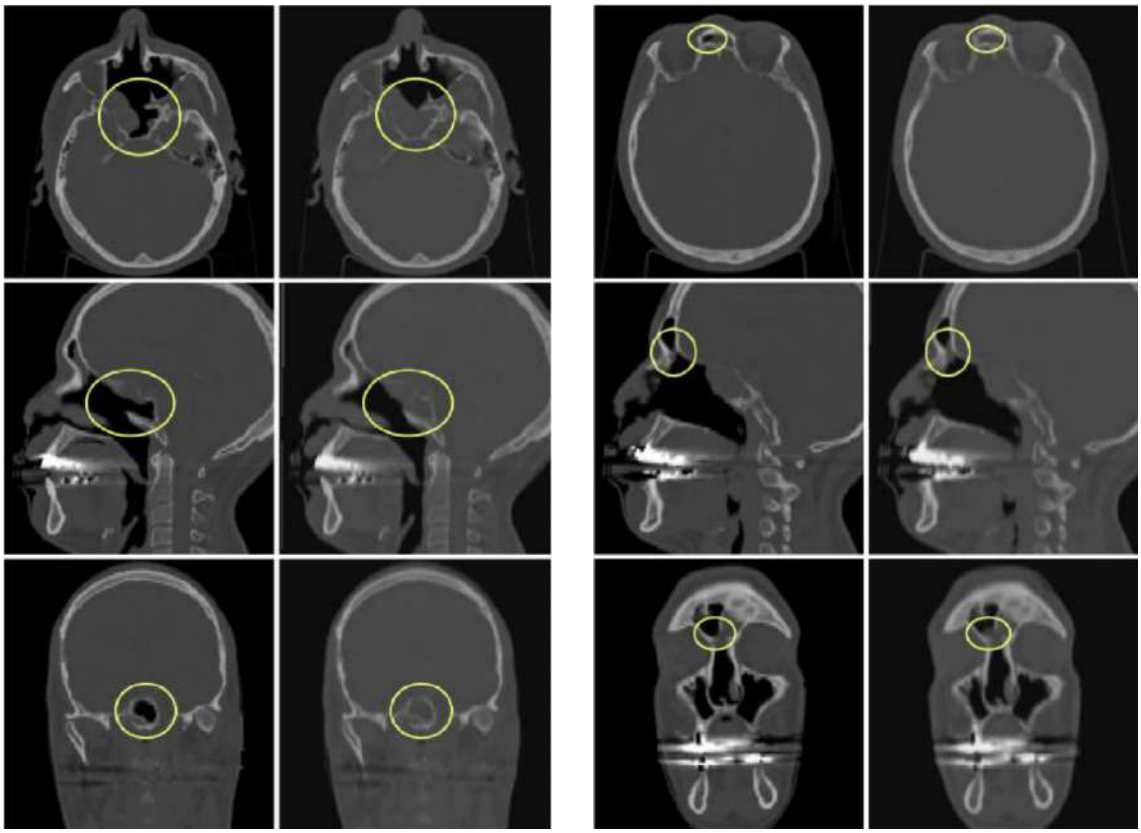

(a) (b)

Figure 3.3: Comparison between the planning CT and the control CT. Left: each row shows the planning CT (first image) and the control CT (second image); the yellow circle highlights the morphological change in the tumor region. Right: the second, smaller morphological change is indicated by the yellow circles. Image adapted from [66].

$$\mathrm{HU} = 1000 \times \frac{\mu - \mu_{\mathrm{water}}}{\mu_{\mathrm{water}} - \mu_{\mathrm{air}}}$$

where μ_{water} and μ_{air} are the linear attenuation coefficients of water and air, respectively. Density variations between the planning CT and the control CT are then expressed as the voxel-wise difference in HU, denoted as ΔHU:

$$\Delta\mathrm{HU} = \left|\mathrm{HU}_{\mathrm{control}} - \mathrm{HU}_{\mathrm{planning}}\right| .$$

Figure 3.4 shows the ΔHU maps obtained by computing the voxel-wise difference between the control CT and the planning CT and superimposed on the CT images using ITK-SNAP [78]. Each row represents axial, sagittal and coronal views, in this order from left to right, of representative slices selected to clearly visualize the identified morphological variations. The image intensity, represented by the colour scale and reported at the bottom of the figure, corresponds to the ΔHU value assigned to each voxel.

Neglecting the region near the mouth, where coregistration effects are dominant and not relevant for this study, the areas with the largest ΔHU values correspond to the two morphological variations introduced in Figure 3.3, with intensity values ranging from approximately 500 to over 1000. The first row highlights the smaller, more superficial varia-

tion (red circles), while the second row shows the larger, deeper variation (yellow circles). Other variations in ΔHU, particularly in regions surrounding the skull, are mainly due to imperfect co-registration between the two CT scans.

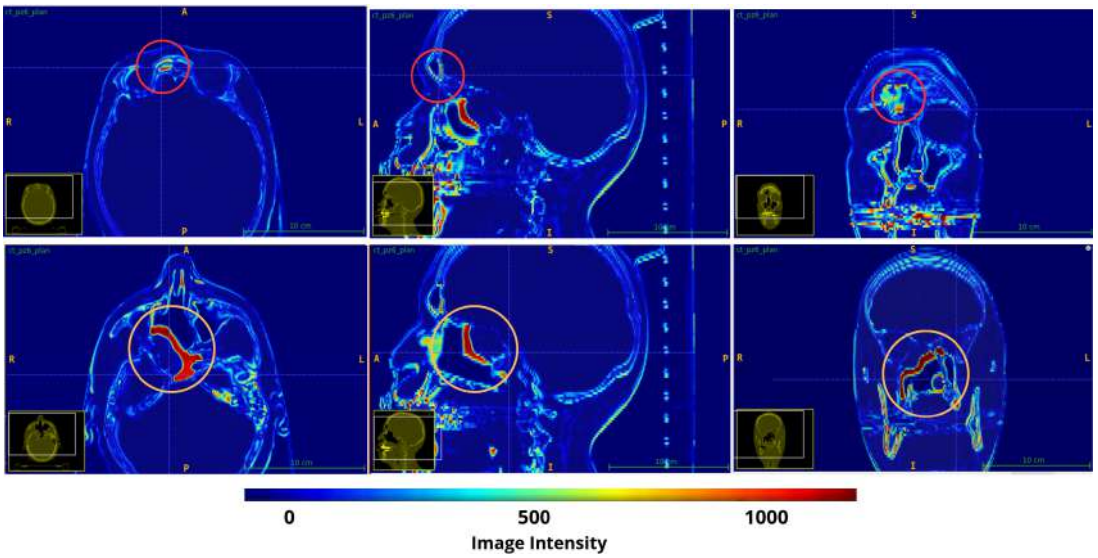

Figure 3.4: Maps of ΔHU superimposed on CT images and visualized using ITK-SNAP. The first row highlights the smaller, superficial variation (red circles), while the second row shows the larger, deeper variation (yellow circles).

The fact that the morphological variations correspond to such ΔHU values is consistent with studies performed in [76], where an optimal threshold for identifying morphological changes was found to lie between 500 and 600 HU. In Figure 3.5, only voxels with ΔHU > 500 are displayed, superimposed on the CT planning images, clearly highlighting the detected morphological changes. As in the previous Figure, the smaller, more superficial variation is shown in the first row (red circles), while the larger, deeper variation is shown in the second row (yellow circles).

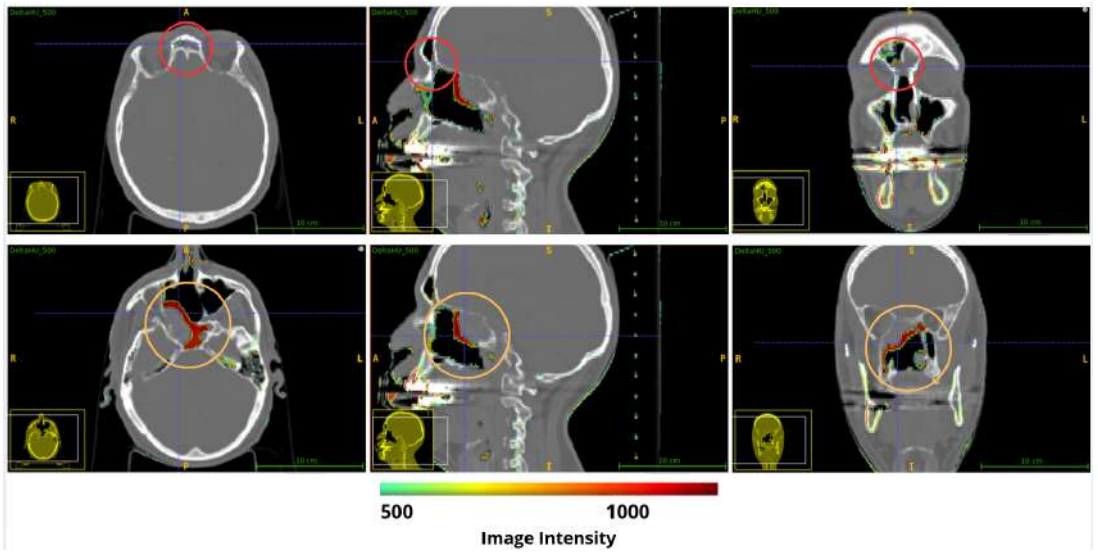

Figure 3.5: Thresholded ΔHU maps (ΔHU > 500) superimposed on CT images, emphasizing the morphological variations identified in Fig. 3.4.

Finally, Figure 3.6 shows the three views of the delivered dose prescribed by the treatment plan, displayed at a representative slice and superimposed on the planning CT.

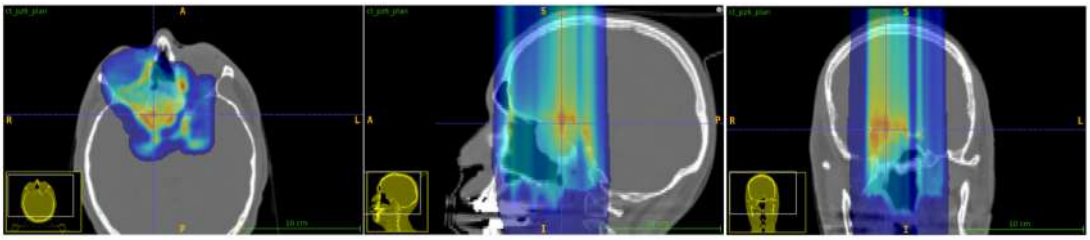

Figure 3.6: Dose distribution prescribed by the treatment plan, superimposed on the planning CT and visualized using ITK-SNAP. The dose map is expressed in arbitrary units, with the colour scale ranging from low (blue) to high (red) values.

3.3 Geometrical Set-Up of the Simulation

The clinical setup of the CNAO facility has been implemented in FLUKA, including the Dose Delivery System (comprising the beam nozzle and the integrated ionization chambers), the carbon-fibre patient couch, the MULTIPASS detector, and the patient, modeled from CT data.
A schematic representation of the simulated setup, as visualized in FLAIR, is shown in Figure 3.7. MULTIPASS is displayed in its operational position, together with the nozzle from which the primary carbon-ion beam is delivered (purple rectangles). The patient CT is positioned on the Patient Positioning System couch.

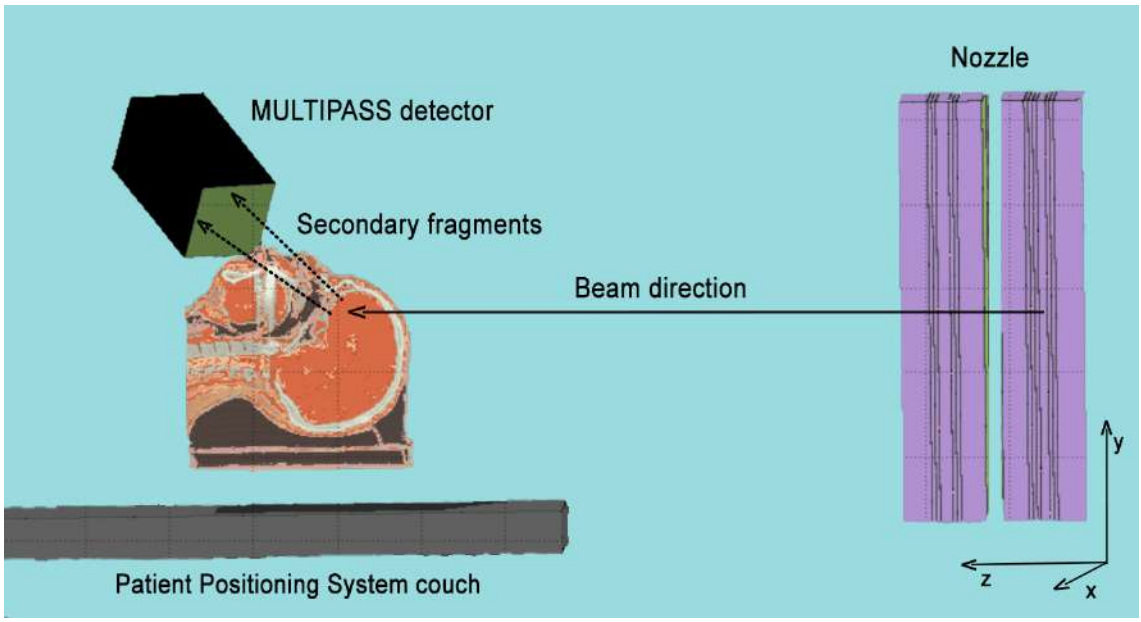

Figure 3.7: Schematic FLAIR representation of the simulated setup, showing the MULTIPASS detector (green), the beam nozzle (purple rectangles), and the patient CT on the Patient Positioning System couch (grey). All components are placed in air. The reference coordinate system used in the simulation is indicated.

In order to enable a direct comparison of the performance of MULTIPASS and the Dose

Profiler in identifying morphological variations, MULTIPASS was positioned to replicate the operating conditions of the Dose Profiler for the same treatment field fraction B3. Starting from an initial alignment with the beam axis (z-axis), the detector was first rotated by approximately 30° around the x-axis, followed by a rotation of approximately 60° around the y-axis. It was then displaced from the isocenter by $r \approx 25$ cm to achieve an angular acceptance of A/r^2, where A denotes the frontal area of the detector ($A \approx 10 \times 10$ cm^2). This angular acceptance is comparable to that of the Dose Profiler ($A \approx 20 \times 20$ cm^2), which is positioned at $r \approx 50$ cm from the isocenter.
Figure 3.8 shows the operating positions of MULTIPASS (top) and the Dose Profiler (bottom).

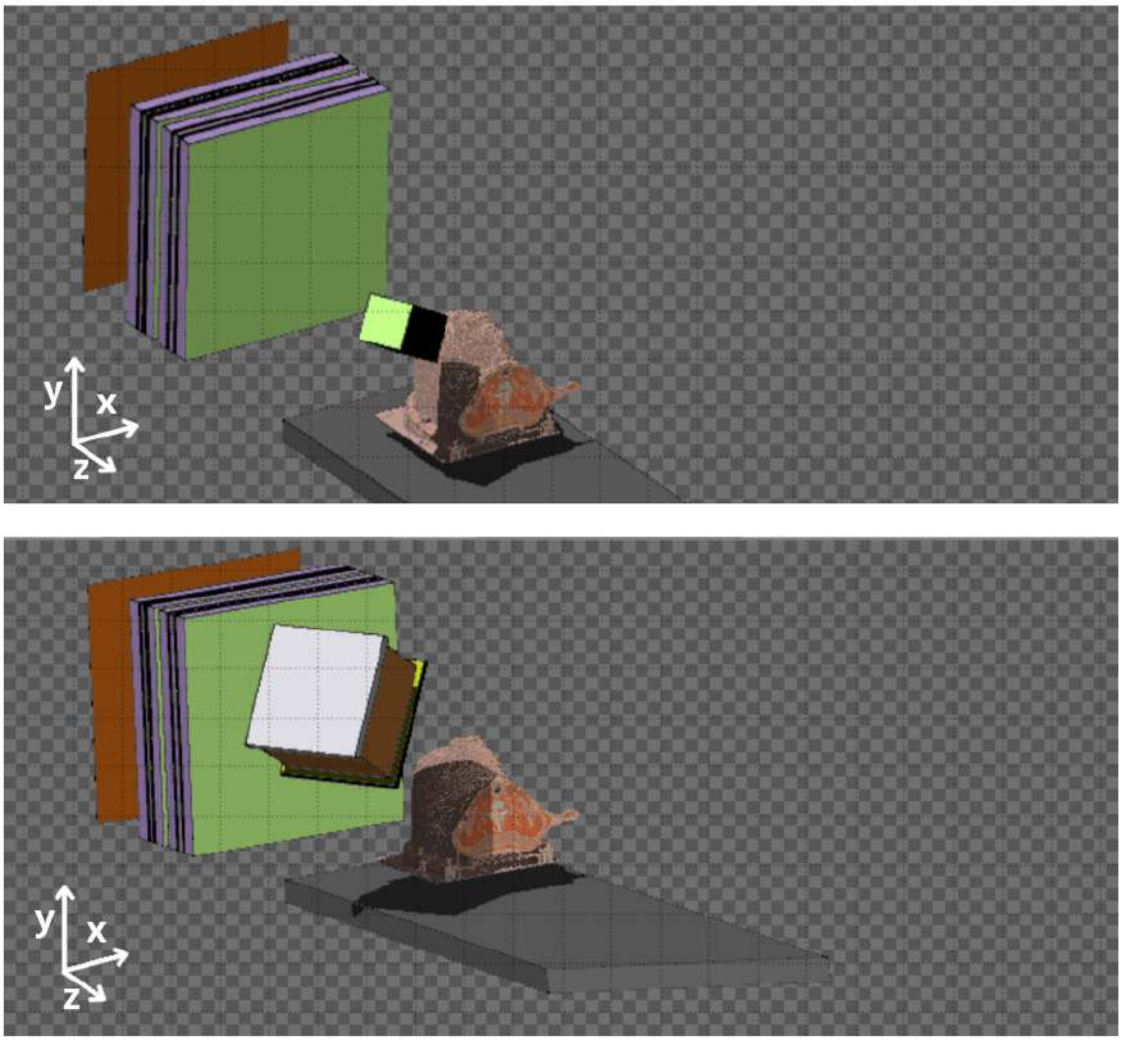

Figure 3.8: FLAIR visualization of the detector positioning used in FLUKA simulations for treatment field B3: MULTIPASS (top) and Dose Profiler (bottom). MULTIPASS is rotated and displaced from the isocenter to match the angular acceptance of the Dose Profiler.

Both CT scans, co-registered as described above, were used as input for the simulations, with one scan per run. By applying the same treatment plan to the planning CT and the control CT and comparing the three-dimensional distributions of the spatial emission coordinates of the secondary particles detected by MULTIPASS, the system sensitivity to

the morphological changes present in the control CT with respect to planning CT can be assessed.

The procedure for generating emission maps of reconstructed secondary charged particles from the two CT scans, and for comparing them to identify morphological variations, will be described in detail in the next chapter, which presents the analysis of the FLUKA simulation output.

Chapter 4

Analysis

This chapter describes the analysis performed on the secondary particles detected by the MULTIPASS detector in simulations of a carbon ion treatment plan carried out with FLUKA, as introduced in Chapter 3. The aim of the analysis is to assess the capability of the MULTIPASS detector to identify morphological variations in the treated region occurring between two different treatment fractions, by exploiting the information carried by the spatial emission distribution of detected secondary protons.
The analysis procedure follows a methodology similar to that already adopted for the Dose Profiler detector [58, 62, 66], adapted here to the MULTIPASS detector.

The workflow starts with event selection (Section 4.1), followed by proton track reconstruction (Section 4.2) and emission point coordinates estimation using the POCA method (Section 4.3). These stages are performed using a C++ code specifically developed for the MULTIPASS detector as part of this thesis.

Three-dimensional emission maps for the planning CT and the control CT are then constructed (Section 4.4) and compared using the gamma index method (Section 4.5). Both the construction of the emission maps and the computation of the gamma index maps are performed by adapting and extending code originally developed within the PAPRICA [64], MONDO [65], and Dose Profiler experimental frameworks.

Finally, Section 4.6 presents a comparison of the performance of the MULTIPASS and Dose Profiler detectors.

4.1 Trigger Study and Definition

The study described in this section consists in defining a trigger strategy to select the events of interest for the subsequent analysis.
The adopted trigger requires MULTIPASS to detect an energy deposition above threshold in at least one fiber of each layer (i.e. both in plane x–z and in plane y–z) for a minimum number of detector planes (for the structure of MULTIPASS, see Section 2.2.1). The deposited energy threshold is set to 50 keV, and the trigger condition requires signals above threshold in at least 40 detector planes.
The reasons behind the choice of the energy threshold and the required number of activated planes is discussed in the following subsections.

4.1.1 Definition of the Energy Threshold

The choice of a 50 keV deposited energy threshold is motivated by the expected energy deposition of a minimum ionizing particle (MIP) traversing a single scintillating fiber. A detector capable of registering the signal produced by a MIP is therefore also expected to be sensitive to secondary protons with higher kinetic energies, which strongly depend on the treatment conditions, in particular on the primary beam energy and on the emission depth of the secondaries. Even in the regime of minimal energy loss within the fiber, the energy deposited by such protons remains above the adopted threshold.

For a MIP, the average stopping power is approximately

$$\left(\frac{dE}{dx}\right)_{\text{MIP}} \simeq 2\,\text{MeV}\,\text{g}^{-1}\,\text{cm}^2\,. \tag{4.1}$$

The scintillating fibers are made of polyvinyltoluene (PVT), whose density is

$$\rho_{\text{PVT}} \simeq 1.03\,\text{g/cm}^3\,. \tag{4.2}$$

The corresponding energy loss per unit length in the material is therefore

$$\left(\frac{dE}{dx}\right)_{\text{MIP}} \simeq 2\,\text{MeV}\,\text{g}^{-1}\,\text{cm}^2 \times 1.03\,\text{g/cm}^3 \simeq 2.06\,\text{MeV/cm}\,. \tag{4.3}$$

The fiber thickness is

$$d = 250\,\mu\text{m} = 2.5 \times 10^{-2}\,\text{cm}\,. \tag{4.4}$$

The average energy deposited by a MIP in a single fiber is thus

$$\Delta E \simeq \left(\frac{dE}{dx}\right)_{\text{MIP}} \cdot d \simeq 2.06\,\text{MeV/cm} \times 2.5 \times 10^{-2}\,\text{cm} \simeq 5.2 \times 10^{-2}\,\text{MeV} \approx 50\,\text{keV}\,. \tag{4.5}$$

So, a value of 50 keV corresponds to the mean energy deposition of a MIP crossing a single fiber at normal incidence.

4.1.2 Definition of the Minimum Number of Triggered Planes

A detector plane is considered activated when at least one fiber in both the x–z and y–z layer records an energy deposition exceeding the defined energy threshold.
The requirement of a minimum of 40 activated detector planes was determined through a dedicated study based on Monte Carlo truth information. This analysis was performed on an event-by-event basis using the simulation data based on the planning CT, with particular emphasis on the protons entering the detector.

Figure 4.1 shows the results of a systematic scan over the plane multiplicity requirement, illustrating which particle species enters the detector—identified by the FLUKA particle code `jpa`—and satisfy progressively increasing minimum numbers of activated planes. While a minimum requirement of one fired plane is sufficient to fully suppress the photon contribution and reduce the neutron contribution by approximately four orders of magnitude, increasing the plane multiplicity threshold mainly enhances discrimination against weakly penetrating particles. A threshold of 40 activated planes effectively suppress spurious events while largely preserving the proton contribution. Specifically, electrons are reduced by more than one order of magnitude, positrons by a factor of five, protons are

only mildly affected (reduced by a factor of 2), and deuterons—the most abundant species after protons — tritons, ^{3}He, and ^{4}He are reduced by slightly more than a factor two.

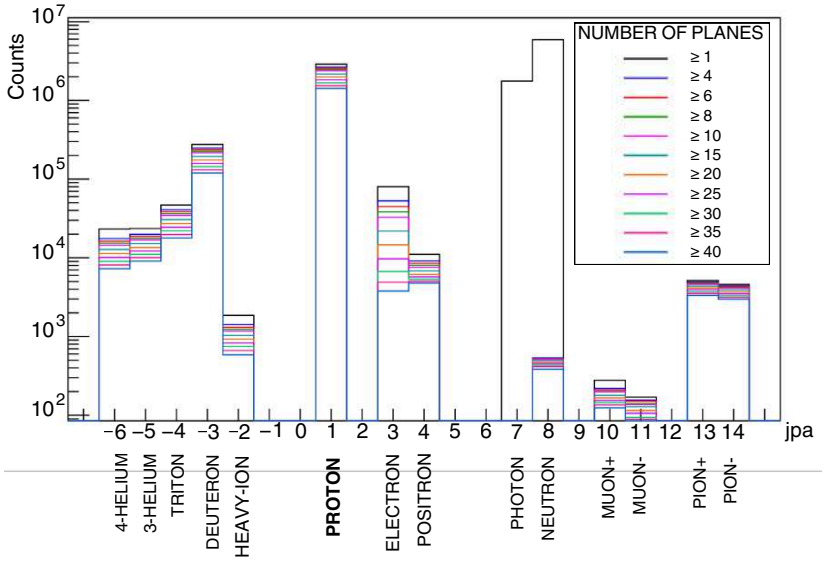

Figure 4.1: For each detected particle species, the number of events fulfilling the trigger condition as a function of the minimum required number of activated detector planes (identified by the different colours) is represented. The labels on the x-axis correspond to the FLUKA `jpa` codes identifying each species; for readability, the names of the detected species are also reported. The y-axis is shown in logarithmic scale.

Figure 4.2 shows the two-dimensional distribution for protons, with the kinetic energy at the detector entrance, $E_{\mathrm{kin}}^{\mathrm{cross}}$, on the x-axis and the number of activated planes on the y-axis. Applying a threshold on the number of activated planes effectively selects protons above a certain energy. In particular, a threshold of 40 planes selects protons with kinetic energy at the detector entrance $E_{\mathrm{kin}}^{\mathrm{cross}} \gtrsim 50$ MeV.

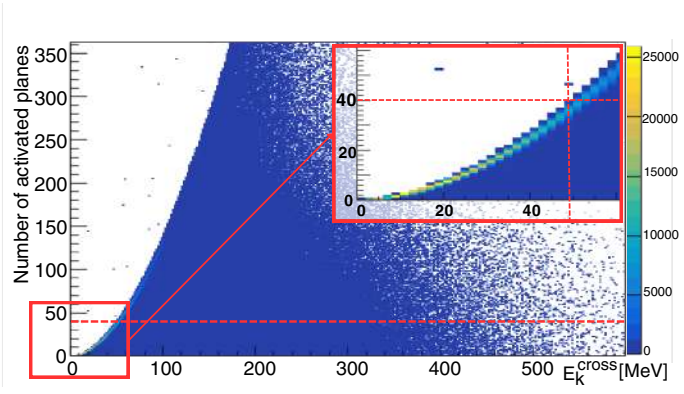

Figure 4.2: Two-dimensional distribution of the number of activated planes as a function of the proton kinetic energy at the detector entrance, $E_{\mathrm{kin}}^{\mathrm{cross}}$. The top-right inset shows a zoomed view of the region corresponding to the plane threshold.

The distribution for non-proton particles is shown in Figure 4.3a, where the number of activated detector planes is plotted as a function of the kinetic energy at the detector entrance, $E_{\mathrm{kin}}^{\mathrm{cross}}$.

The resulting distribution can be interpreted as the superposition of contributions from different particle species entering the detector. Applying a threshold of 40 activated planes effectively removes low-energy light particles with kinetic energies below approximately 10 MeV, which deposit most of their energy within the first $\sim$ 35 planes, as highlighted in the inset of Figure 4.3a. This low-energy component is predominantly due to electrons, positrons, and pions, as shown in Figure 4.3b. Instead, the part of the distribution that resembles the behaviour observed for protons is associated with deuterons, tritons, ^{3}He, ^{4}He, and other heavy ions not explicitly specified by FLUKA. This contribution is illustrated in Figure 4.3c.

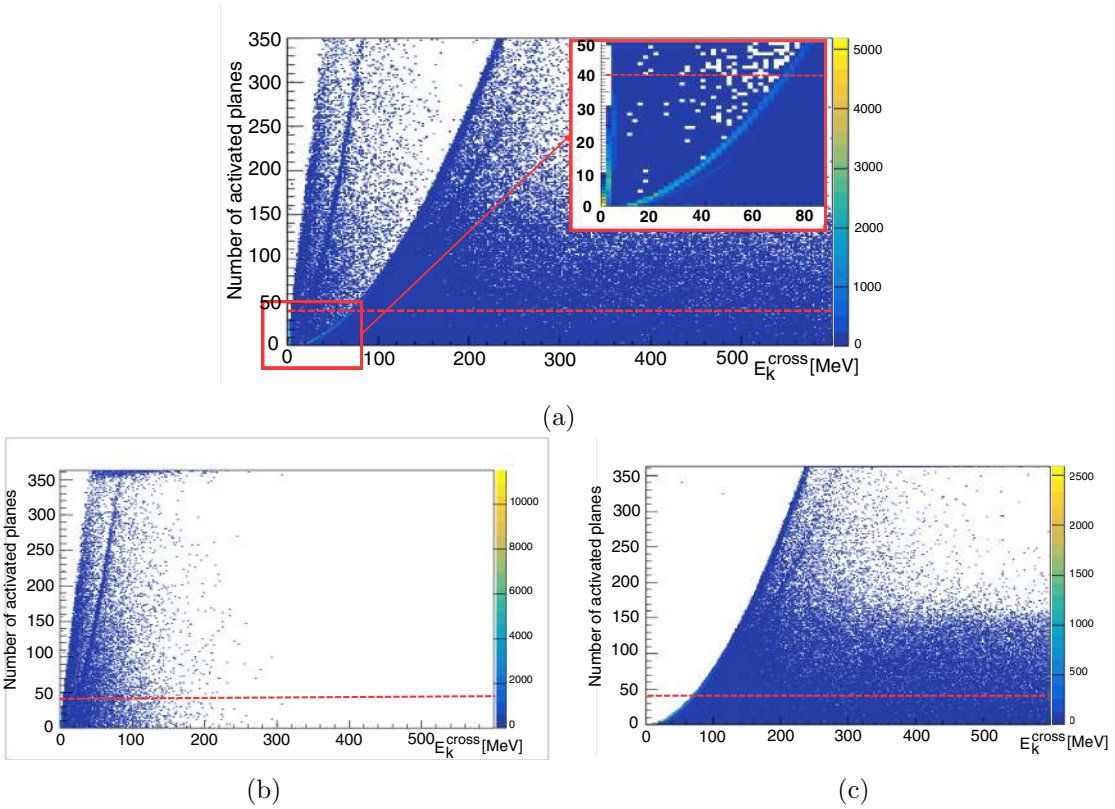

Figure 4.3: Two-dimensional distributions of the number of activated detector planes as a function of the kinetic energy at the detector entrance, $E_{\text{kin}}^{\text{cross}}$, for non-proton particles. The top panel includes all non-proton species, while the bottom panels separate electrons, positrons and pions (left) from deuterons, tritons, ^{3}He, ^{4}He, and other heavy ions not explicitly specified by FLUKA (right). The red dashed line indicates the plane multiplicity threshold.

A preliminary study of the backtracking resolution was carried out to evaluate the trigger. In this study, the focus was on the spatial resolution along the beam axis, z, which is directly related to the beam range. The backtracking resolution was investigated as a function of the kinetic energy at the crossing point, $E_{\text{kin}}^{\text{cross}}$, within the relevant energy range. For each selected energy value, the resolution along this direction was defined as the standard deviation of a Gaussian fit to the distribution of residuals, $z_{\text{reco}} - z_{\text{true}}$, where z_{reco} is the reconstructed position and z_{true} the true emission point from the Monte Carlo simulation. The procedure adopted to reconstruct the emission points will be described in detail in Section 4.2.

A more comprehensive characterization of the backtracking resolution along all spatial directions will be performed at the end of the reconstruction process in Section 4.2, including an additional selection criterion that will be introduced later.
An example of the residual distribution and the corresponding Gaussian fit, obtained for particles with $E_{\text{kin}}^{\text{cross}} = 50$ MeV, is shown in Figure 4.4.

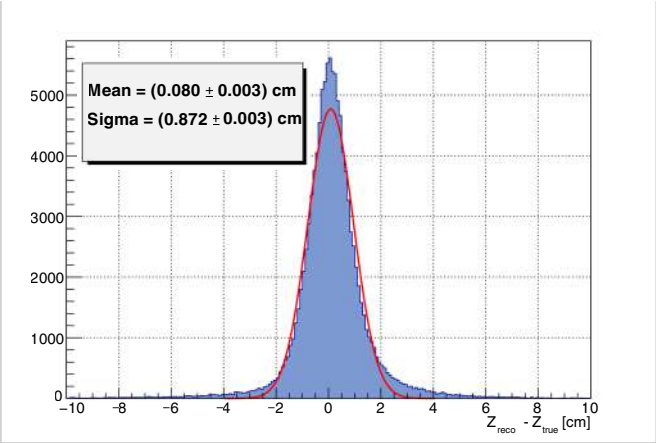

Figure 4.4: Distribution of the residuals $z_{\text{reco}} - z_{\text{true}}$ along the z direction for particles with $E_{\text{kin}}^{\text{cross}} \approx 50$ MeV. The red curve represents the Gaussian fit used to extract the backtracking resolution. The mean value and standard deviation obtained from the Gaussian fit, together with their uncertainties, are reported.

The results of the study (Figure 4.5) indicate that particles with higher kinetic energy at the crossing point exhibit improved backtracking resolution. In particular, particles crossing the detector with $E_{\text{kin}}^{\text{cross}} \approx 50$ MeV are associated with a backtracking resolution of approximately 9 mm. This value is compatible with the intrinsic physical limitations imposed by multiple Coulomb scattering, which originates from the cumulative small-angle deflections experienced by the fragments while traversing the patient's body and leads to an uncertainty on the reconstructed emission point of the order of 5–10 mm, depending on the type and thickness of the traversed material [62].

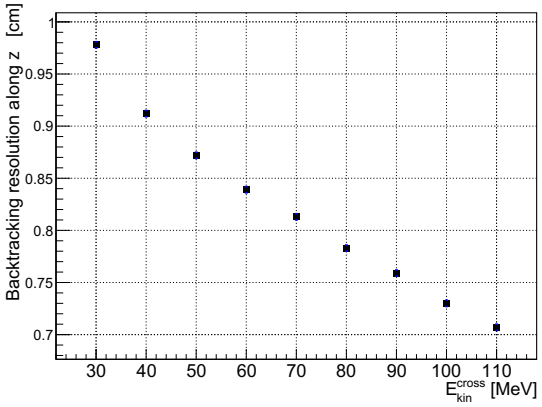

Figure 4.5: Backtracking resolution along the beam direction z for particles entering the detector with different kinetic energies at the crossing point, $E_{\text{kin}}^{\text{cross}}$. Vertical error bars indicate the uncertainties from Gaussian fits; all are 0.003 cm and thus too small to be visible.

To summarize, a threshold of 40 activated planes ensures that the selected events are predominantly proton-induced ($\approx 90\%$), with contributions from other particle species largely suppressed. The selected particles have sufficient kinetic energy at the crossing point ($E_{\text{kin}}^{\text{cross}} \gtrsim 50$ MeV), allowing a backtracking resolution along the z direction that is compatible with the requirements of the subsequent analysis.

For reference, the Dose Profiler trigger selects events corresponding to an energy threshold at the detector entrance of approximately $E_{\text{kin}}^{\text{cross}} \approx 30$ MeV.

4.2 Track Reconstruction

Once the proton events are selected, the detector hits are first grouped into clusters, as described in Subsection 4.2.1. Proton tracks are then reconstructed and fitted to determine the corresponding track parameters, following the procedure outlined in Subsection 4.2.2. The full track reconstruction has been implemented based on the reconstruction procedure originally developed for the Dose Profiler, with the algorithms clearly adapted to the specific geometry of MULTIPASS.

4.2.1 Clustering

Energy depositions in adjacent fibres within the same detector layer are clustered to obtain a more accurate estimate of the proton crossing position. This is necessary because a single proton might activate more than one fibre due to readout cross talk. Although the current simulation considers ideal fibre hits and does not include the effects of the detector electronics, clustering is applied to ensure consistency with the future integration of the full electronic readout of experimental data.

In the present study, hits occurring in neighbouring fibres are grouped together to form a cluster. Specifically, any fibres within a ± 3 position indices (referred to as fibre addresses) are considered part of the same cluster. In this Monte Carlo simulation, the resulting cluster size is close to one fibre on average, as shown in Figure 4.6, with about 90% of the clusters consisting of a single fibre. This behaviour is expected, since the analysis is based on idealised energy depositions and does not account for electronic integration. Consequently, energy depositions are predominantly confined to a single fibre, and clustering rarely combines multiple fibres.

4.2.2 Track Reconstruction using Hough Transform

The reconstruction of charged fragment tracks is performed using the Hough transform [79], a well-established technique in image processing for the detection of parametric geometric features, in particular straight lines. The key idea of the Hough transform is to reformulate the problem of identifying colinear points in the image space as the problem of locating maxima in a suitably defined parameter space.

In the image plane (x, y), a straight line can be described using the normal parametrization

$$x \cos\theta + y \sin\theta = \rho, \tag{4.6}$$

where θ is the angle of the normal to the line with respect to the x-axis and ρ is the algebraic distance of the line from the origin (Figure 4.7, left). By restricting θ to the interval $[0, \pi)$, each straight line is uniquely represented by a point in the two-dimensional parameter space (θ, ρ).

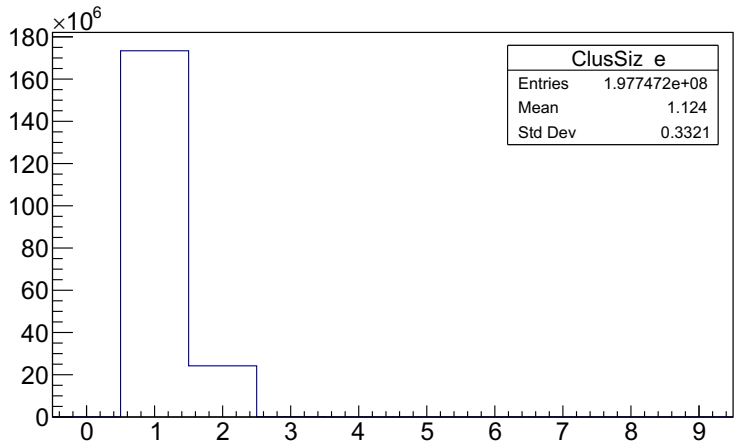

Figure 4.6: Cluster size obtained from the analysis of the planning CT data. The average cluster size is close to one fibre.

Given a set of points (x_i, y_i) in the image plane, each point is mapped into the parameter space as a sinusoidal curve defined by

$$\rho(\theta) = x_i \cos\theta + y_i \sin\theta. \tag{4.7}$$

This curve represents the set of all straight lines passing through the point (x_i, y_i). If multiple points in the image plane lie on the same straight line, the corresponding sinusoidal curves intersect at a common point (θ_0, ρ_0), which uniquely identifies the parameters of that line (Figure 4.7, right).

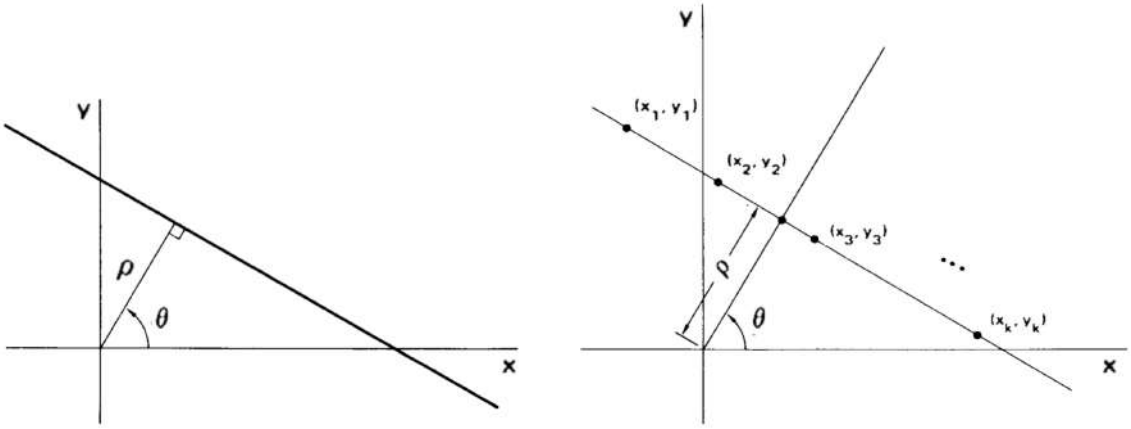

Figure 4.7: Left: Representation of the parameters θ and ρ describing a straight line in the image plane (x, y). Right: Illustration of a set of collinear points in the image plane and of the straight line passing through them. The parameters θ and ρ associated with this line correspond to an accumulation point in the Hough parameter space, since all points share, among the family of lines passing through each of them, this same (θ, ρ) pair. Images adapted from [79].

From a computational perspective, the Hough transform is implemented by discretizing the parameter space (θ, ρ) into finite bins and introducing an accumulator histogram. Each image point contributes a vote to all bins corresponding to the set of lines compatible with

its position. As a result, bins associated with straight lines supported by a large number of colinear points accumulate a higher number of votes. The detection of straight lines is therefore reduced to the identification of local maxima in the accumulator histogram, which correspond to the most probable line candidates present in the image.
In this work, the Hough transform is applied independently in the x–z and y–z projections of the detector to reconstruct two-dimensional track candidates. For each cluster, the local coordinates (z, x) or (z, y) are extracted and used to compute the Hough parameters over a discrete set of angular values. In each projection, the corresponding accumulator histogram is filled accordingly. After the accumulation step, bins whose content exceeds a defined threshold of five clusters are selected as two-dimensional track candidates. This threshold, along with other key parameters such as the discretization intervals of the Hough parameter space, was chosen empirically to suit the specific geometry of MULTIPASS and to achieve satisfactory track reconstruction, rather than through a systematic optimization procedure.
The filled accumulator histograms are visualized in Figure 4.8, showing the distribution of votes in both the x–z and y–z views for one of the analyzed events.

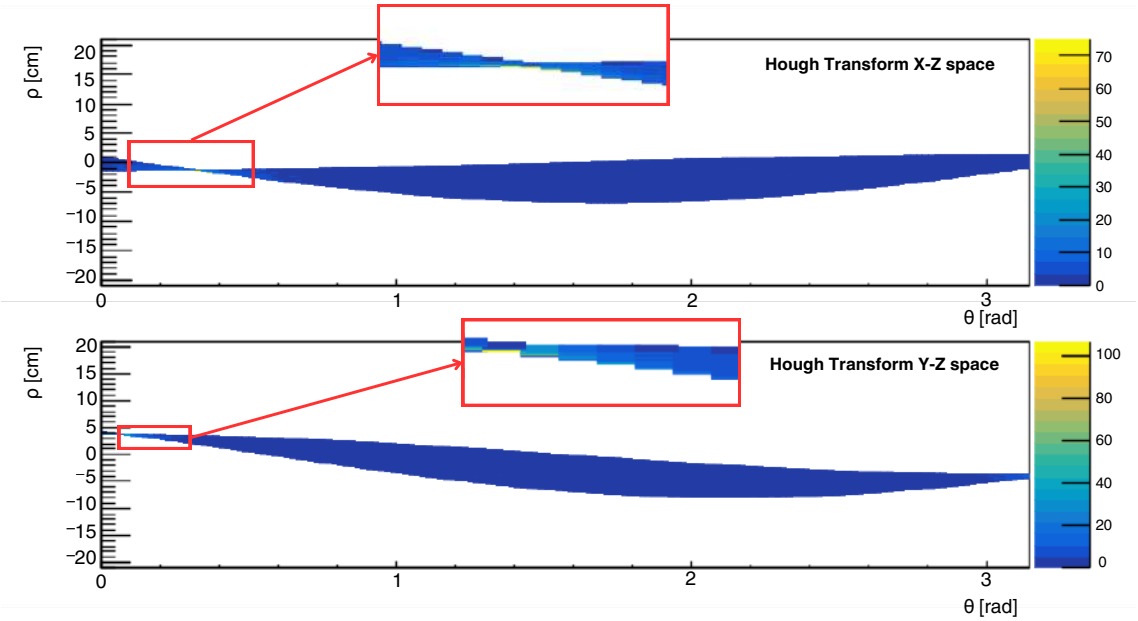

Figure 4.8: Hough transform histograms in both x–z and y–z views for one of the events analyzed. The zoomed panel highlights the region around the accumulation point, showing the most populated bins.

The final stage of the reconstruction consists of combining the track candidates obtained in the two projections to form three-dimensional tracks. Each candidate in the x–z plane is paired with candidates in the y–z plane.

Once the track candidates have been reconstructed, their parameters are refined by performing a linear fit and evaluating a chi-square for each track. Subsequently, a cleaning procedure is applied to remove duplicate or redundant tracks corresponding to the same physical trajectory. Tracks are compared pairwise according to their reconstructed directions and positions, taking into account the associated uncertainties. Tracks whose directions and positions are compatible within a tuned threshold are considered to correspond to the same underlying trajectory. For each group of compatible tracks, the

clusters contributing to the individual tracks are combined, avoiding duplication, and a single, consolidated track is formed. This process is iterated until all candidate tracks have been considered, resulting in a final set of tracks in which each physical trajectory is represented uniquely.

Finally, once the cleaning and combination steps are completed, a definitive linear fit is performed on the final set of tracks to determine their optimized parameters.

An example of a reconstructed track, viewed in both views, is showed in Figure 4.9.

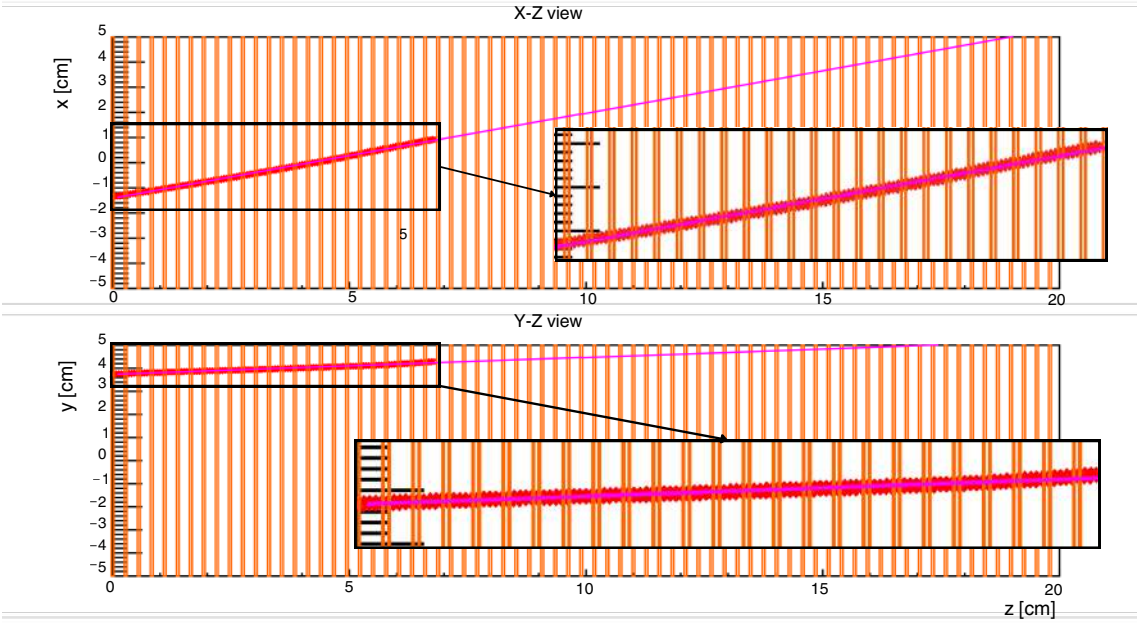

Figure 4.9: Reconstructed track of a detected proton. In both views, the inset shows a zoomed-in portion of the track. The cluster positions are shown in red, while the fitted track is represented by the purple line. The orange lines represent the detector planes; for clarity, only one out of every five planes is shown.

At the end of the track reconstruction process, approximately 80% of the events that activate the trigger result in a single detected track, while the remaining 20% correspond either to multiple reconstructed tracks or to no track at all. Only events leading to the reconstruction of a single track are considered in the subsequent analysis, as they provide unambiguous and reliable information about the particle trajectories.

Figure 4.10 shows the distribution of particle species responsible for these selected single-particle tracks in the planning CT simulation, identified by their FLUKA particle code (`jpa`) using Monte Carlo truth information. It can be seen that approximately 90% of the reconstructed tracks originate from protons.

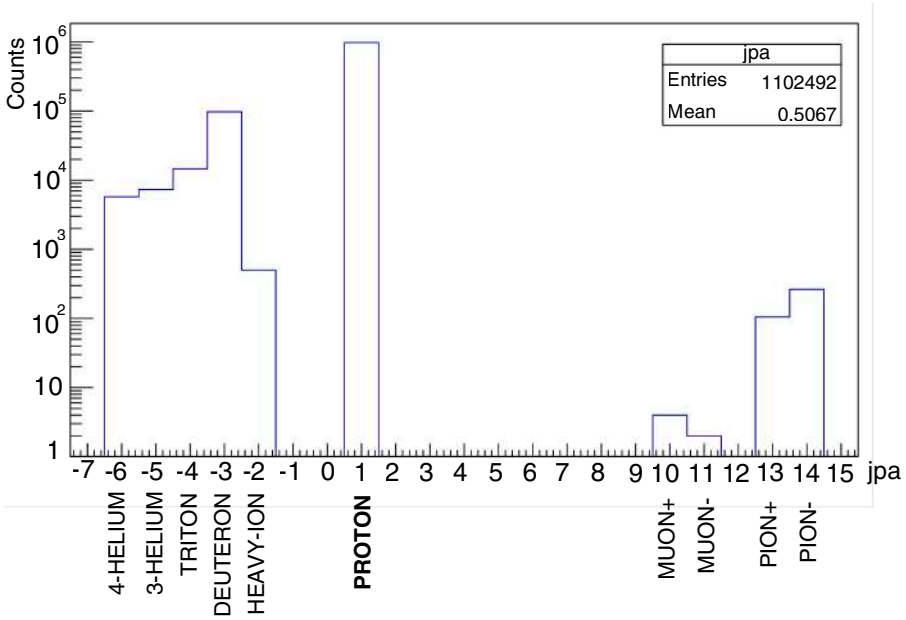

Figure 4.10: Distribution of particles contributing to the reconstructed tracks in the planning CT simulation (Monte Carlo truth). The x-axis shows the FLUKA particle codes (`jpa`) with corresponding particle names.

4.3 Emission Point Measurement

Once the tracks have been selected and fitted, fragment back-tracking is performed. The three-dimensional coordinates of the fragment production point are estimated using the Point of Closest Approach (POCA) method, which identifies the (x, y, z) coordinates of the point where the distance between the reconstructed fragment track and the incoming primary beam is minimized. Both the fragment trajectory and the primary beam are approximated as straight lines, with the beam direction and position known from the treatment plan. This stage of the analysis has also been implemented within the MULTIPASS C++ analysis code, based on an adaptation of the Dose Profiler analysis code.

To ensure that only tracks with limited multiple Coulomb scattering are considered, an additional selection is applied based on the Distance Of Closest Approach (DOCA) between the track and the primary beam axis. The DOCA provides a quantitative measure of the geometrical compatibility between the reconstructed track and the primary beam. Tracks with small DOCA values are more likely to have undergone minimal deflection, while larger DOCA values indicate strong scattering within the patient or misreconstruction. This DOCA-based selection, which is not implemented in the Dose Profiler analysis, has not been systematically investigated. In particular, its impact on the spatial resolution of the reconstructed tracks has not been evaluated and could be the subject of future dedicated studies.

Figure 4.11 shows the two-dimensional distribution of the proton kinetic energy at the detector entrance, $E_{\text{kin}}^{\text{cross}}$, as a function of the distance of closest approach (DOCA), for events selected in the planning CT simulation using Monte Carlo truth information.
To enhance the accuracy of the backtracking procedure, a maximum DOCA threshold of 1 cm is applied. This selection retains approximately 85% of the events in which a single track has been successfully reconstructed and was chosen pragmatically as a

compromise between improved track quality and adequate statistical significance. The plot illustrates that higher-energy protons tend to have smaller DOCA values, confirming that the selection effectively retains well-aligned, high-energy tracks while reducing the contribution of scattered or misreconstructed tracks.

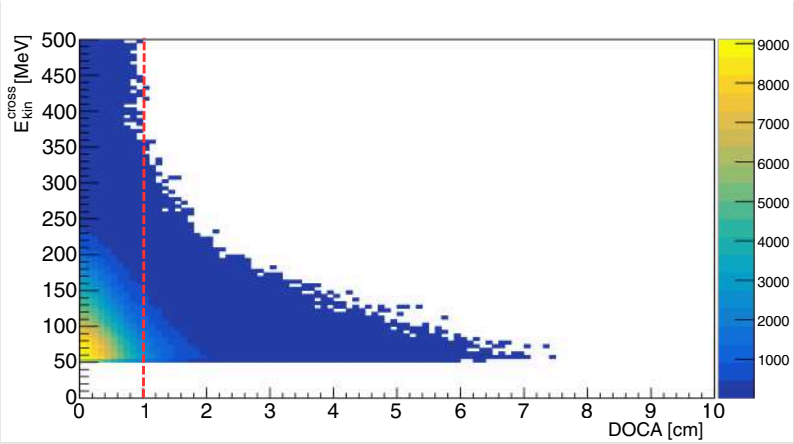

Figure 4.11: Two-dimensional distribution of the particle kinetic energy at the detector entrance, $E_{\text{kin}}^{\text{cross}}$, obtained from Monte Carlo truth information, as a function of the Distance Of Closest Approach (DOCA) to the primary beam axis, for events selected in the planning CT simulation. The red dashed line indicates the imposed DOCA threshold.

Finally, the performance of the emission point coordinates reconstruction has been evaluated by analysing the residuals between the reconstructed POCA coordinates and the true emission coordinates from Monte Carlo truth. The transverse residuals, $x_{\text{POCA}} - x_{\text{MC}}$ and $y_{\text{POCA}} - y_{\text{MC}}$, exhibit an approximately Gaussian shape. Gaussian fits to the distributions yield mean values of 0.03 cm and -0.05 cm, and standard deviations of 0.26 cm and 0.26 cm, respectively (Figures 4.12a and 4.12b). The asymmetric tails observed in the transverse residual distributions indicate the presence of a systematic bias in the reconstruction of the emission point. This effect is primarily attributed to the non-symmetric positioning of the MULTIPASS detector in the treatment room, which is shifted along both the x and y directions (see Figure 3.7). In particular, the observed bias originates from the interplay between the one-sided detector geometry and the depth-dependent acceptance of secondary protons. Events produced at larger distances from the detector experience a reduced detection probability and are reconstructed with degraded angular resolution due to multiple Coulomb scattering and the limited track lever arm.

The longitudinal residual, $z_{\text{POCA}} - z_{\text{MC}}$, is centred around -0.02 cm with a standard deviation of 0.74 cm from a Gaussian fit (Figure 4.12c). Although the longitudinal resolution is worse than the transverse, it remains comparable to the uncertainty introduced by multiple scattering in the patient (which is in the range of 5–10 mm [62]).
By comparing the backtracking resolution along the z direction obtained in Section 4.1.2 with the one derived in the present analysis, where an additional DOCA selection criterion is imposed, a clear improvement is observed. In particular, the longitudinal standard deviation decreases from 0.9 cm to 0.7 cm. This shows that the DOCA cut efficiently suppresses poorly reconstructed or strongly scattered tracks, resulting in a more accurate reconstruction of the emission point.

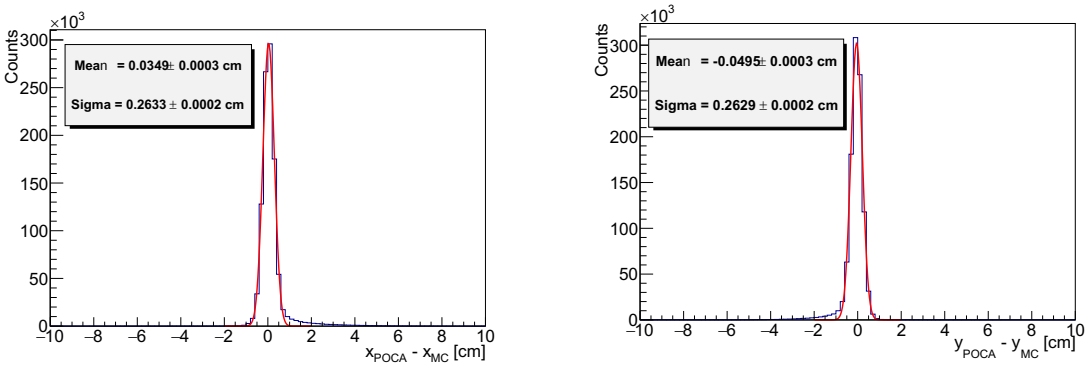

(a)

(b)

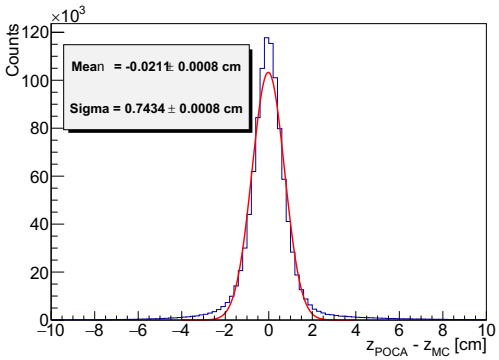

(c)

Figure 4.12: Residual distributions between the POCA-reconstructed coordinates and the Monte Carlo truth for the x, y, and z directions. Gaussian fits to the cores of the distributions are shown, with the extracted mean and standard deviation reported for each direction.

4.4 Reconstruction of 3D Emission Maps

Once the POCA distributions of the selected secondary fragments have been reconstructed in the x, y, and z coordinates in the global reference frame of the treatment room, they are processed using a dedicated C++ analysis code, originally developed within the Dose Profiler framework, to generate three-dimensional emission maps.

The patient CT and a geometry file are provided to transform the POCA coordinates from the laboratory reference frame to the CT reference frame, allowing direct visualization of the emission maps overlaid on the CT images.

Emission maps are constructed on a three-dimensional voxel grid matching the CT geometry. Each POCA is assigned to the corresponding voxel based on its spatial coordinates, incrementing the voxel content to build a raw map representing the spatial density of fragment emission points.

To reduce statistical fluctuations and account for the finite spatial resolution, a smearing procedure is applied. For each voxel, the emission density is computed by averaging the raw map values within a spherical volume of radius R centered on the voxel. A fixed number of points are sampled uniformly inside the sphere, and trilinear interpolation is used to evaluate the raw map at these positions. The voxel value is then obtained as the mean of all valid contributions. In this work, a smearing radius of $R = 5$ mm is used for all emission maps, as it was found to provide the most suitable balance between spatial resolution and noise reduction for the subsequent analysis.

Figure 4.13 shows the reconstructed emission maps for the treatment plan delivered on the planning CT (left) and on the control CT (right), visualized using ITK-SNAP [78] overlaid on the respective CT images. The color scale ranges from blue, corresponding to the lowest emission intensity, to red, corresponding to the highest.

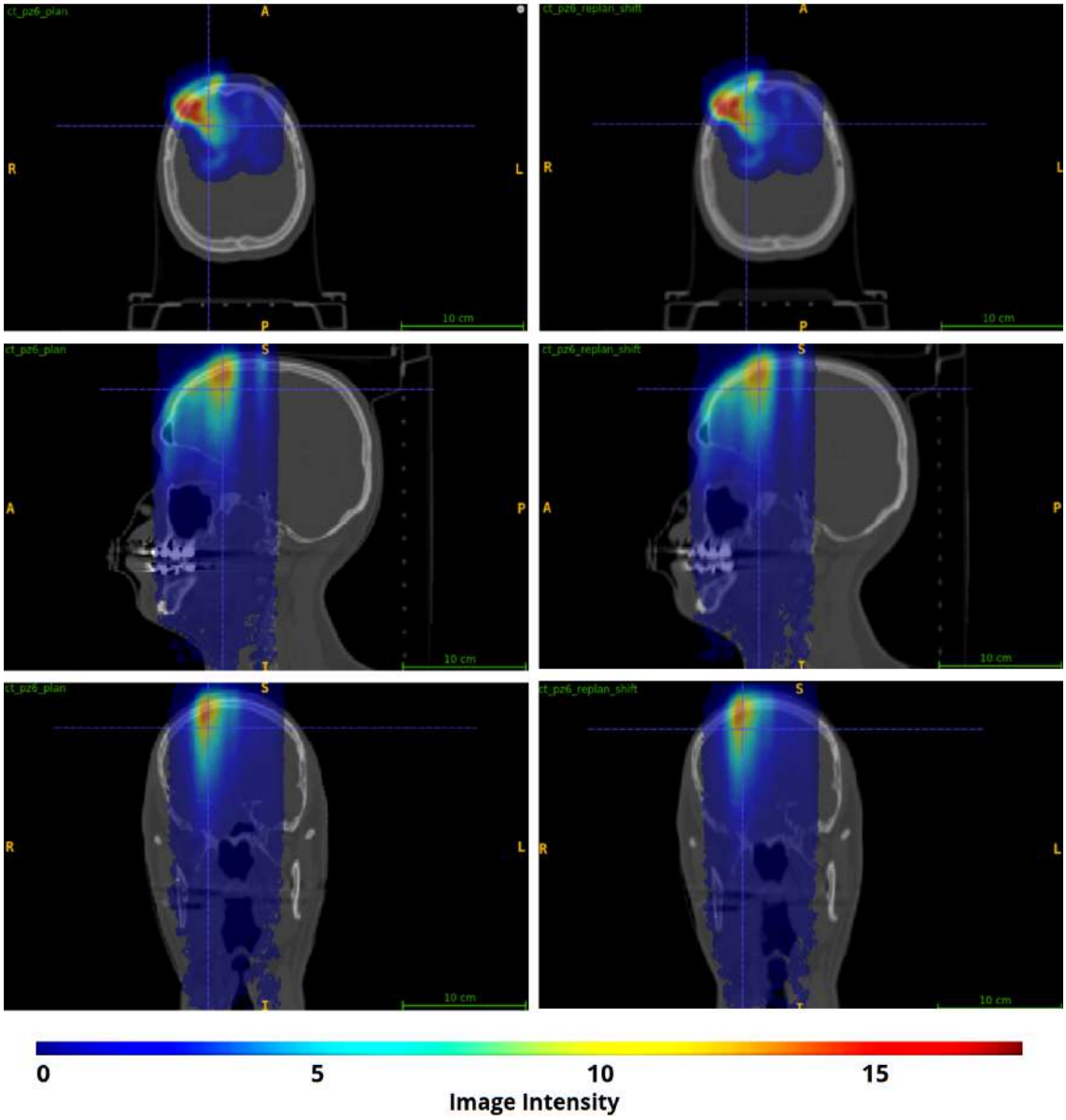

Figure 4.13: Reconstructed three-dimensional emission maps from the simulations based on the planning CT (left) and the control CT (right), overlaid on the corresponding CT images and displayed using ITK-SNAP [78]. A smearing radius of $R = 5$ mm has been used.

4.5 Gamma Index Analysis

Once the emission maps have been reconstructed for both the planning CT and the control CT, possible morphological variations are investigated using the gamma index test. Originally developed for dosimetric verification, the gamma index is a well-established method for quantifying the level of agreement between two three-dimensional dose distributions [80], defined as a reference and an evaluation map.
In this work, the gamma index formalism is adapted to compare secondary fragment emission maps acquired in different treatment fractions. In this context, local discrepancies between the two emission maps identified by the gamma index test are interpreted as signatures of morphological changes occurring within the treated region of the patient.

Subsection 4.5.1 introduces the gamma index formalism and describes the procedure adopted to construct three-dimensional gamma index maps. Subsection 4.5.2 presents the patient-specific analysis carried out in this thesis, illustrating the application of the method to identify regions affected by morphological variations and discussing the capability of the MULTIPASS detector to detect such changes.

4.5.1 Gamma Index Formalism and Optimisation Criteria

The gamma index is defined as a distance metric in a two-dimensional space that simultaneously accounts for spatial displacement and emission density differences between a reference distribution and an evaluated distribution. For a given voxel $\vec{r}_e$ belonging to the evaluation map, the gamma function is defined as

$$\Gamma(\vec{r}_e, \vec{r}_r) = \sqrt{\frac{|\vec{r}_e - \vec{r}_r|^2}{r^2} + \frac{|D_e(\vec{r}_e) - D_r(\vec{r}_r)|^2}{D^2}}, \tag{4.8}$$

where $\vec{r}_r$ denotes a voxel of the reference map, $D_e(\vec{r}_e)$ and $D_r(\vec{r}_r)$ are the emission densities evaluated at positions $\vec{r}_e$ and $\vec{r}_r$, respectively, while r and D represent the spatial and emission density tolerance parameters.
For each voxel $\vec{r}_e$ of the evaluation map, the gamma function $\Gamma(\vec{r}_e, \vec{r}_r)$ is computed over all voxels $\vec{r}_r$ of the reference map. The gamma index associated with $\vec{r}_e$ is then defined as the minimum value obtained:

$$\gamma(\vec{r}_e) = \min_{\vec{r}_r}\{\Gamma(\vec{r}_e, \vec{r}_r)\}. \tag{4.9}$$

A gamma index value greater than unity ($\gamma(\vec{r}_e) > 1$) indicates that the emission density at voxel $\vec{r}_e$ differs from the reference distribution beyond the prescribed spatial and density tolerances, and is therefore interpreted as a significant deviation.

The outcome of the gamma index test strongly depends on the choice of the tolerance parameters r and D, which define the acceptance criteria for spatial agreement and emission density differences, respectively.
The parameter r represents the distance-to-agreement criterion and sets the spatial scale over which deviations between the evaluation voxel $\vec{r}_e$ and the reference voxels $\vec{r}_r$ are penalized. In the gamma formalism, the spatial separation enters the gamma function through the normalized term $|\vec{r}_e - \vec{r}_r|/r$. Increasing r reduces the weight of spatial mismatches in the gamma calculation and therefore increases the probability of finding at least one reference voxel satisfying the condition $\Gamma(\vec{r}_e, \vec{r}_r) \leq 1$.

Similarly, the tolerance parameter D defines the acceptable emission density difference between the evaluation and reference maps. For a given spatial tolerance r, if the emission density differences $|D_e(\vec{r}_e) - D_r(\vec{r}_r)|$ exceed the tolerance D for all reference voxels considered in the minimization, the resulting gamma index is greater than unity and the test fails. Increasing D relaxes the density agreement criterion, allowing larger discrepancies to be accepted and thus increasing the likelihood of a passing gamma test.

Figure 4.14 illustrates a schematic representation of the one-dimensional gamma index test.

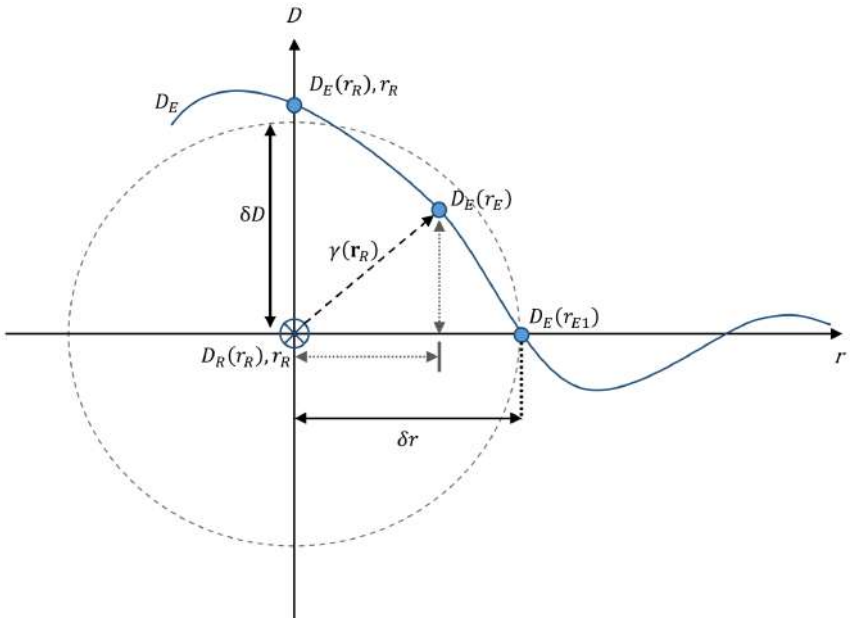

Figure 4.14: Schematic representation of the one-dimensional gamma index method. The y-axis represents the emission density D, while the x-axis denotes the spatial coordinate r. The cross identifies the reference point, and the blue curve corresponds to the evaluated emission density distribution, with solid circles indicating discrete sampling points. The distance-to-agreement δr and emission density difference δD criteria define an acceptance ellipse around the reference point. According to Equation 4.8, the point $D_E(r_R)$ yields $\gamma > 1$, $D_E(r_E)$ yields $\gamma < 1$, and $D_E(r_{E1})$ corresponds to $\gamma = 1$. Since at least one evaluated point lies within the acceptance ellipse, Equation 4.9 results in $\gamma < 1$ for the reference point. Image adapted from [81], originally from [80].

For the purposes of this thesis, the emission map obtained from the planning CT is used as the reference, while the emission map from the control CT serves as the evaluation map. This allows the construction of a three-dimensional gamma index map that preserves the spatial structure of the original emission distributions, with each voxel assigned its corresponding gamma index value, $\gamma(\vec{r}_e)$, thereby indicating local regions potentially affected by morphological variations.
The construction of the gamma index maps is performed using a dedicated C++ analysis code previously developed for three-dimensional emission map comparisons, which has been adapted and extended in this work to process and analyze MULTIPASS data. These gamma index maps can be visualized in two complementary ways. In the *pass rate mode*, the map is binarized according to the gamma criterion: voxels with $\gamma \leq 1$ are considered not discrepant and displayed in red, while voxels with $\gamma > 1$ are considered discrepant

and displayed in green. This representation highlights clusters of voxels that do not meet the gamma criteria, facilitating the identification of discrepant regions. In the *gamma mode*, each voxel is instead assigned its calculated gamma value, resulting in a continuous color scale that provides a more detailed view of the magnitude of local deviations. in the gamma mode map, the color scale ranges from blue, indicating non-discrepant voxels, to red, indicating discrepant voxels.

The gamma index computation implemented in the analysis code is governed by three configurable parameters, which adapt and extend the tolerance criteria r and D inherent to the gamma index definition of Equation 4.8. These parameters set the acceptance criteria of the test and allow the sensitivity of the method to be tuned. They are defined as follows:

- DTA (Distance To Agreement) [mm]: defines the maximum spatial displacement allowed between a voxel in the reference map and the corresponding voxel in the evaluated map.
- DD (emission Density Distance) [%]: quantifies the allowable difference in emission density between the evaluated map and the reference map. It is expressed as a percentage of the maximum emission density in the reference map:

$$\mathrm{DD} = \frac{D}{D_{r,\max}} \times 100\%. \tag{4.10}$$

- DTH (Density THreshold) [%]: excludes voxels with emission densities below a specified fraction of the maximum reference density from the analysis, reducing the impact of statistical noise in regions with negligible signal.

To quantify the ability to identify regions affected by morphological variations for given values of DTH, DTA, and DD in the gamma index test, two metrics were then introduced: *efficiency* (δ) and *purity* (ϵ).

The efficiency (δ) is defined as

$$\delta = \frac{\text{number of voxels with } \gamma > 1 \text{ and } \Delta HU > \text{threshold}}{\text{number of voxels with } \Delta HU > \text{threshold}} \tag{4.11}$$

where the numerator represents the number of voxels that simultaneously exhibit a gamma index value greater than unity and a difference in Hounsfield Units (ΔHU) between the two CT scans exceeding a given threshold. The denominator consists of all voxels with ΔHU values above the same threshold. With this definition, efficiency ranges between 0 and 1 and measures the fraction of truly discrepant voxels correctly detected by the gamma index test. The ΔHU threshold is introduced to exclude negligible differences between the two CTs that could lead to small, non-meaningful ΔHU values. As described in Section 3.2, a threshold of 500 has been set.

The second metric, purity (ϵ), is defined as

$$\epsilon = \frac{\text{number of voxels with } \gamma > 1 \text{ and } \Delta HU > \text{threshold}}{\text{number of voxels with } \gamma > 1} \tag{4.12}$$

where the numerator is identical to that in Eq. (4.11), while the denominator includes all voxels with $\gamma > 1$. Purity quantifies the precision of the gamma index test, indicating the

fraction of voxels flagged as discrepant by the gamma analysis that are actually associated with a true morphological variation.

Previous studies have shown that maximising efficiency alone leads to gamma index maps that are strongly affected by noise [82], while maximising purity alone can produce maps that are overly selective and less sensitive to subtle variations. Therefore, a balanced optimisation of efficiency and purity is necessary to achieve a reliable compromise between statistical robustness and sensitivity to clinically relevant morphological changes.

4.5.2 Patient-Specific Gamma Index Analysis: Case Study

In this subsection, the application of the gamma index method to the patient case studied in this thesis, introduced in Chapter 3, is presented. The analysis is divided into two parts: first, the study of the gamma index maps using the conventional definition of the DD parameter, as given in Equation 4.10, following the approach adopted in previous studies; second, the evaluation based on a modified formulation of DD, aimed at improving sensitivity in low-emission regions of the 3D emission maps. The overall objective is to assess the capability of the MULTIPASS detector to identify morphological variations in the patient anatomy through the application of this method.

The region of interest is restricted to the volume directly irradiated by the beam. This volume is defined as a parallelepiped encompassing the Clinical Target Volume (CTV), which corresponds to the anatomical region intended to receive the prescribed dose. Limiting the evaluation to the CTV ensures that the analysis focuses on areas where morphological variations are most relevant for treatment accuracy. By concentrating on this volume, the gamma index effectively highlights deviations that could impact the delivered dose (in Figure 3.6) within the target region.

Gamma Index Analysis with Original DD Definition

As evident from the emission maps in Figure 4.13, the region affected by morphological changes (visualized in Figure 3.5) exhibits a relatively low emission intensity, of the order of 0.1, compared to maximum values around 20. This occurs because the region is located at depth and does not correspond to the area of maximum dose deposition. Consequently, the fraction of secondary particles originating from that region is small relative to other areas.

In a clinical context, typical emission Density Distance (DD) values are generally no smaller than 2%, since the analysis primarily concerns regions with substantial emission, while low-emission areas are less relevant. In this study, however, to remain sensitive to variations in the region of interest, the parameter DD defined by Equation 4.10, which is normalized to the maximum emission intensity, is studied for smaller values. This ensures that even changes in low-emission regions, such as a doubling or halving of the intensity, produce a gamma index greater than unity. Conversely, if DD is too large, the gamma index becomes insensitive to such variations.
Accordingly, gamma index maps are evaluated for DD values of 0.25%, 0.5%, 1%, 1.5% and 2%, in order to explore the sensitivity of the test in the region of interest. To preserve sensitivity in low-emission regions—which are of primary relevance in this study, a Density THreshold DTH = 0% is used. The Distance-To-Agreement parameter DTA is scanned over the range 10–40 mm, in steps of 10 mm.

Figure 4.15 shows the resulting efficiency and purity trends under these conditions. Panel (a) shows the efficiency δ as a function of DD for different values of DTA (see legend), while panel (b) reports the purity ϵ for the same values of DD and DTA.

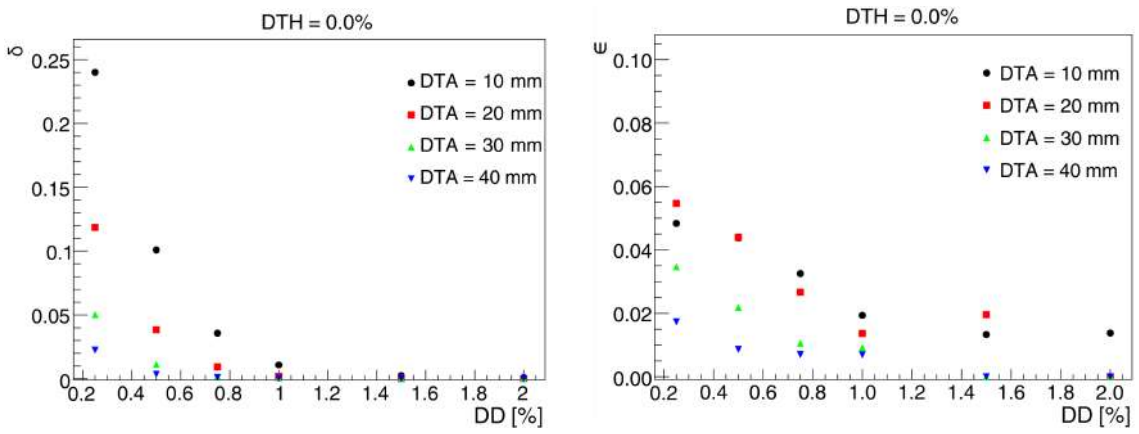

(a) (b)

Figure 4.15: Efficiency δ (left) and purity ϵ (right) trends as a function of DD for different values of DTA (specified in the legend) and for DTH = 0.0%.

It can be observed that for DD $> 1\%$, the efficiency values drop significantly, indicating that very few voxels with true morphological variations are detected.

An illustrative example is provided by the gamma index maps obtained with DD = 1.5% and DTA = 20 mm, corresponding to a purity of approximately 2% and an efficiency close to zero. Figure 4.16 shows the map in pass rate mode, while Figure 4.17 presents the corresponding map in gamma mode.
In the pass rate map, most voxels are displayed in red, corresponding to $\gamma < 1$, indicating the low sensitivity of the test for this choice of parameters. Voxels identified as discrepant ($\gamma > 1$) are highlighted in green. Despite the poor overall performance, the small morphological variation is correctly detected (see the right panel of Figure 3.3 and the top panel of Figure 3.5 for the corresponding CT-based visualization), as indicated by the red circle, whereas the larger morphological change is not identified.
The maps are shown in the three standard anatomical views (axial, sagittal and coronal), arranged vertically from top to bottom, and overlaid on the planning CT.

By maintaining DTA = 20 mm and DTH = 0% and lowering the DD value to 0.25%, a configuration that maximizes the purity up to approximately 5% while still ensuring an efficiency of about 12% is obtained. Figure 4.18, Figure 4.19, and Figure 4.20 show representative slices for this configuration in pass rate mode.
In the first two figures, the true morphological variations are correctly detected: Figure 4.18 shows the superficial morphological variation (see the right panel of Figure 3.3 and the top panel of Figure 3.5 for the corresponding CT-based visualization), while Figure 4.19 shows the deeper and greater morphological variation (see the left panel of Figure 3.3 and the bottom panel of Figure 3.5 for the corresponding CT-based visualization). However, the maps appear significantly noisy, mainly due to the very low DD value. Moreover, an additional variation, not corresponding to a real morphological change, is identified in a different slice (Figure 4.20), located in the region of maximum dose deposition.

Such a small value of DD produces a highly noisy map and an overly sensitive response, potentially highlighting apparent variations in regions where no true morphological change is present. This represents a major limitation for the analysis, as the aim is to detect genuine morphological variations with a good degree of certainty. Conversely, increasing DD suppresses sensitivity to low-emission regions, making genuine variations nearly undetectable.
If the region of expected morphological variation were known *a priori* (for example, in the case of a known progression of a specific disease), this issue could be mitigated by further restricting the volume of interest, allowing the sensitivity of the gamma index test to be increased in the relevant region. However, such information is not typically available. For this reason, a modified gamma index approach is explored.

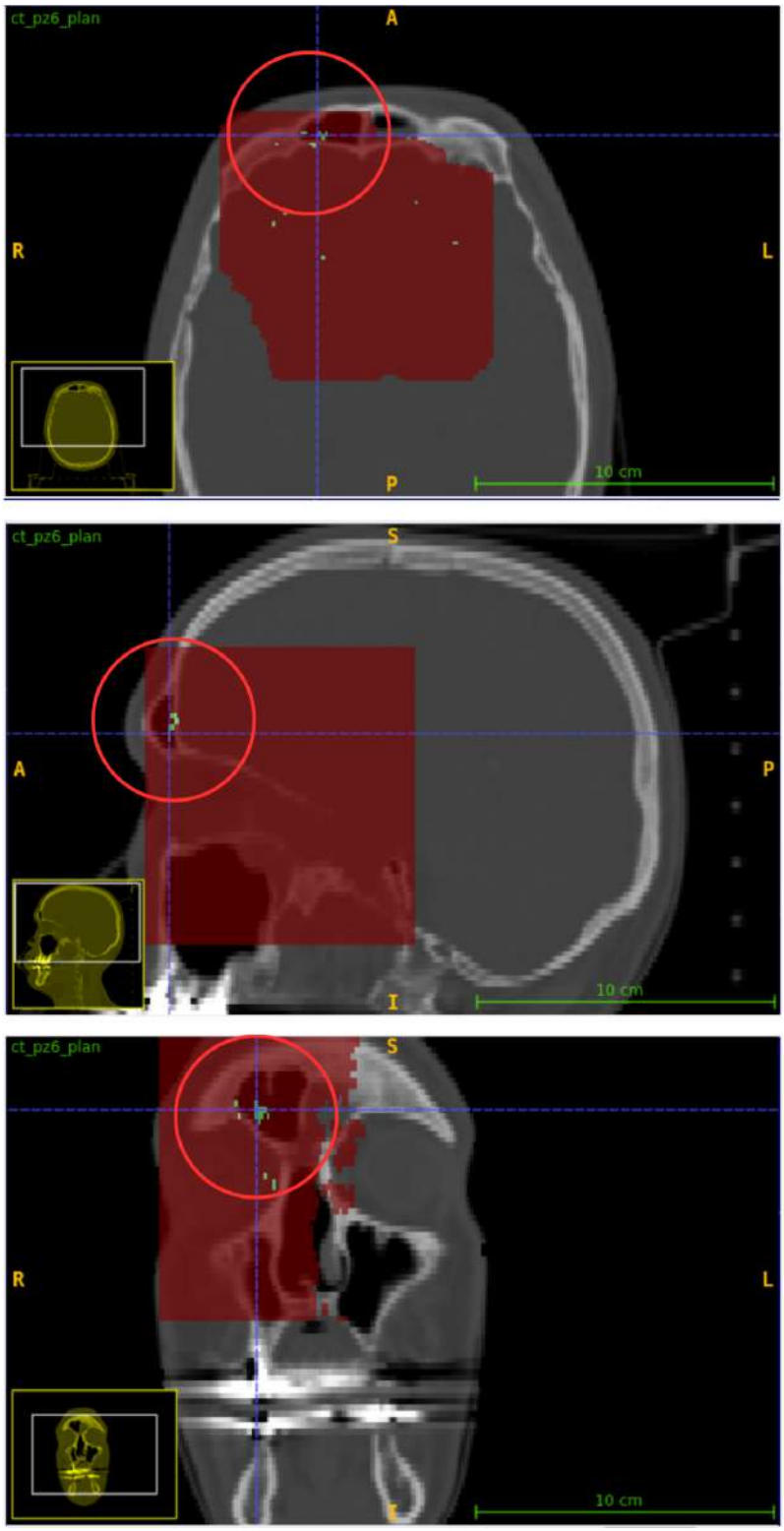

Figure 4.16: Pass rate map for DD = 1.5%, DTA = 20 mm, DTH = 0% in axial, sagittal and coronal views (from top to bottom), overlaid on the planning CT. Only the small morphological variation is detected (red circle), whereas the larger morphological change is not identified.

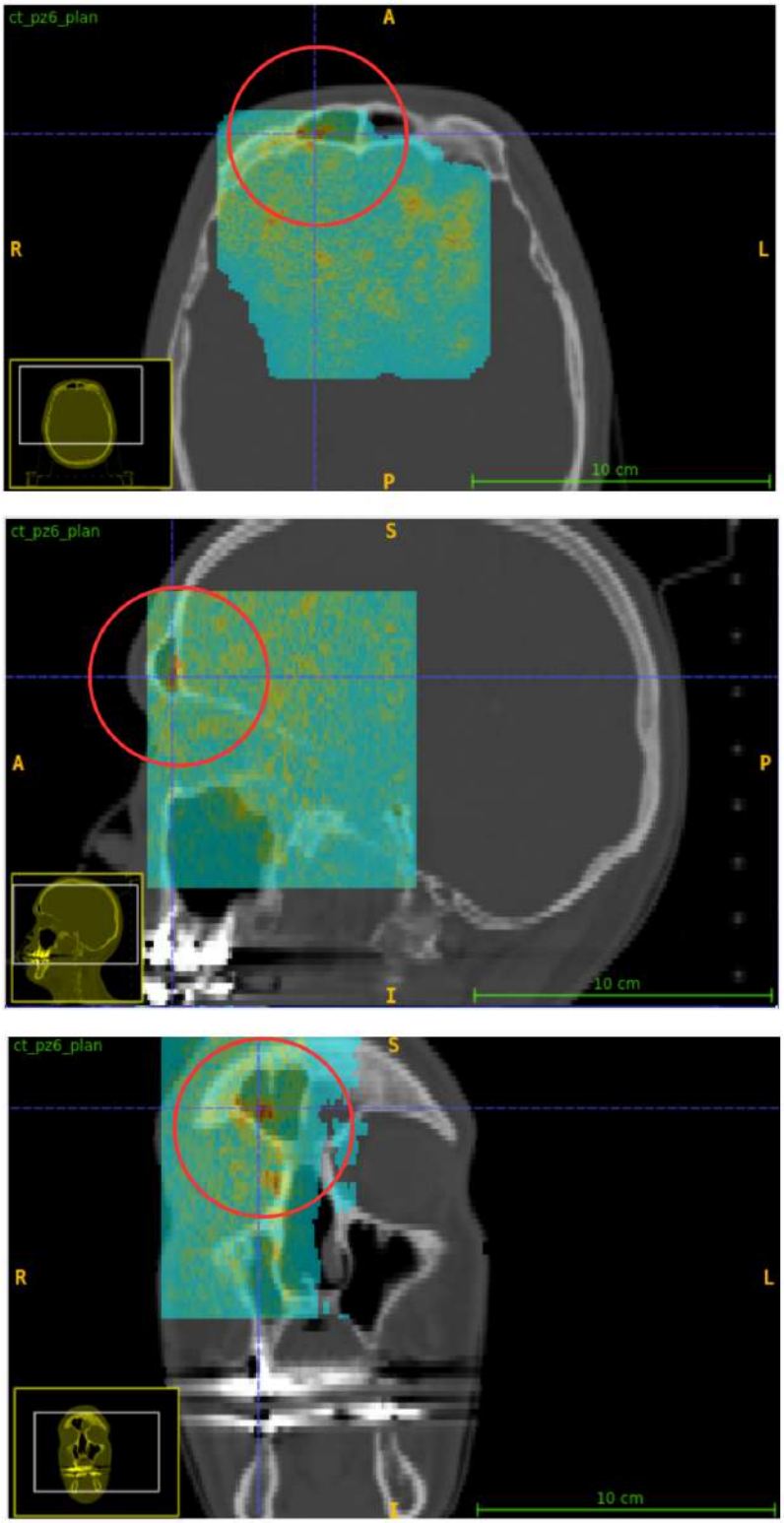

Figure 4.17: Gamma mode map for DD = 1.5%, DTA = 20 mm, DTH = 0% in axial, sagittal and coronal views (from top to bottom), overlaid on the planning CT. Only the small morphological variation is detected (red circle), whereas the larger morphological change is not identified.

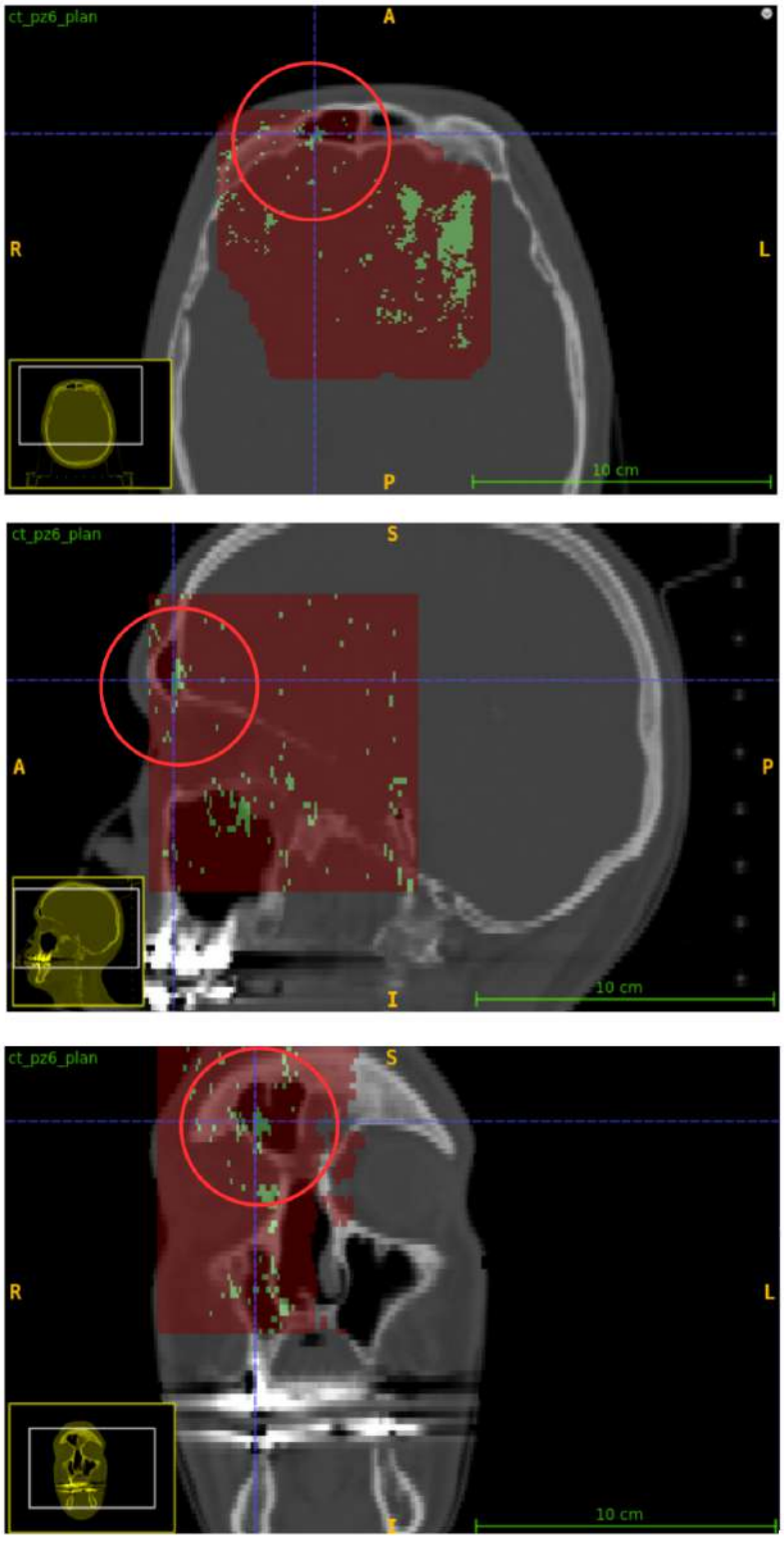

Figure 4.18: Pass rate map for DD = 0.25%, DTA = 20 mm, DTH = 0%, showing the superficial morphological variation (red circle) in axial, sagittal and coronal views (from top to bottom), overlaid on the planning CT.

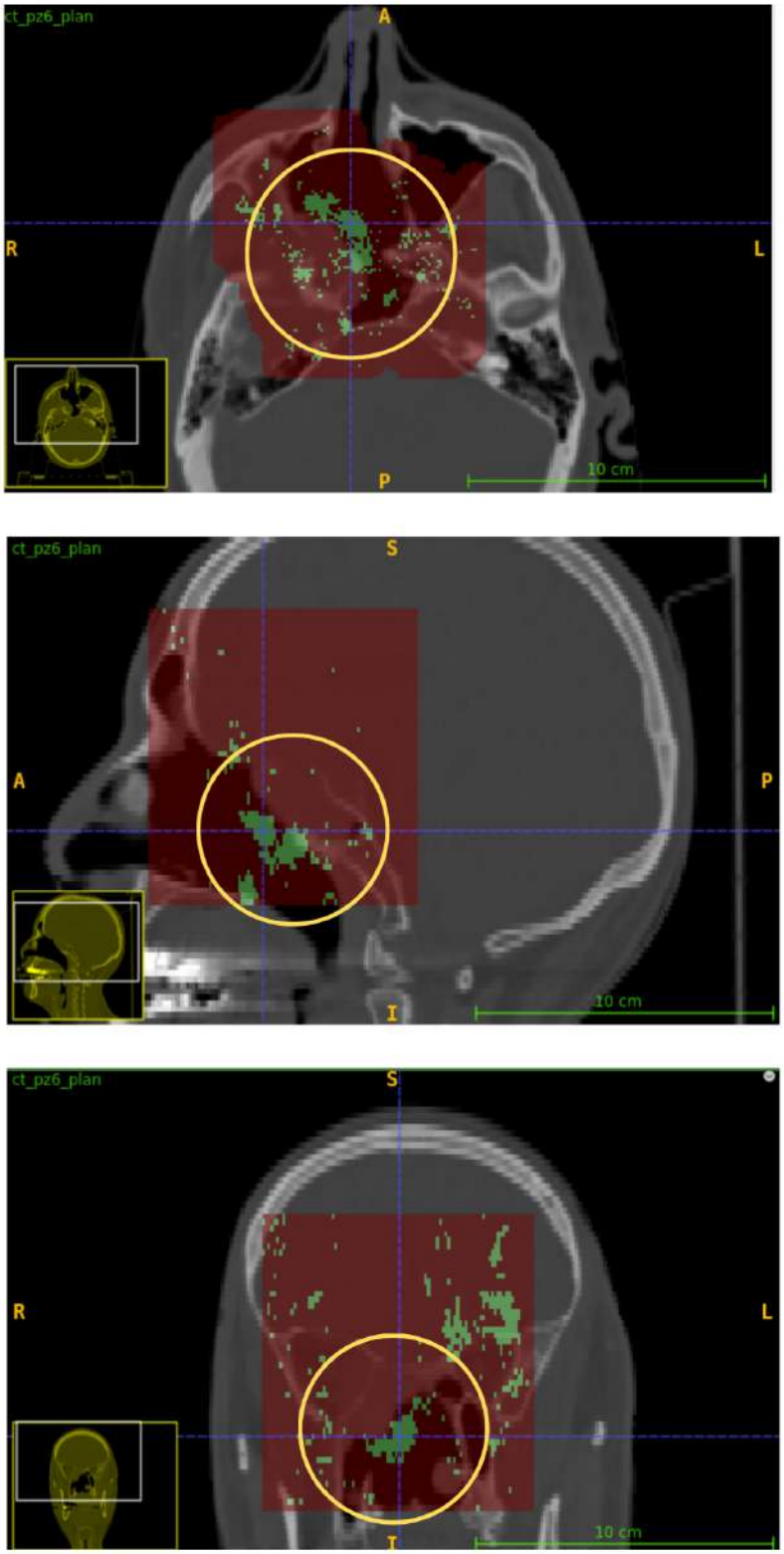

Figure 4.19: Pass rate map for DD = 0.25%, DTA = 20 mm, DTH = 0%, showing the deep and large morphological variation (yellow circle) in axial, sagittal and coronal views (from top to bottom), overlaid on the planning CT.

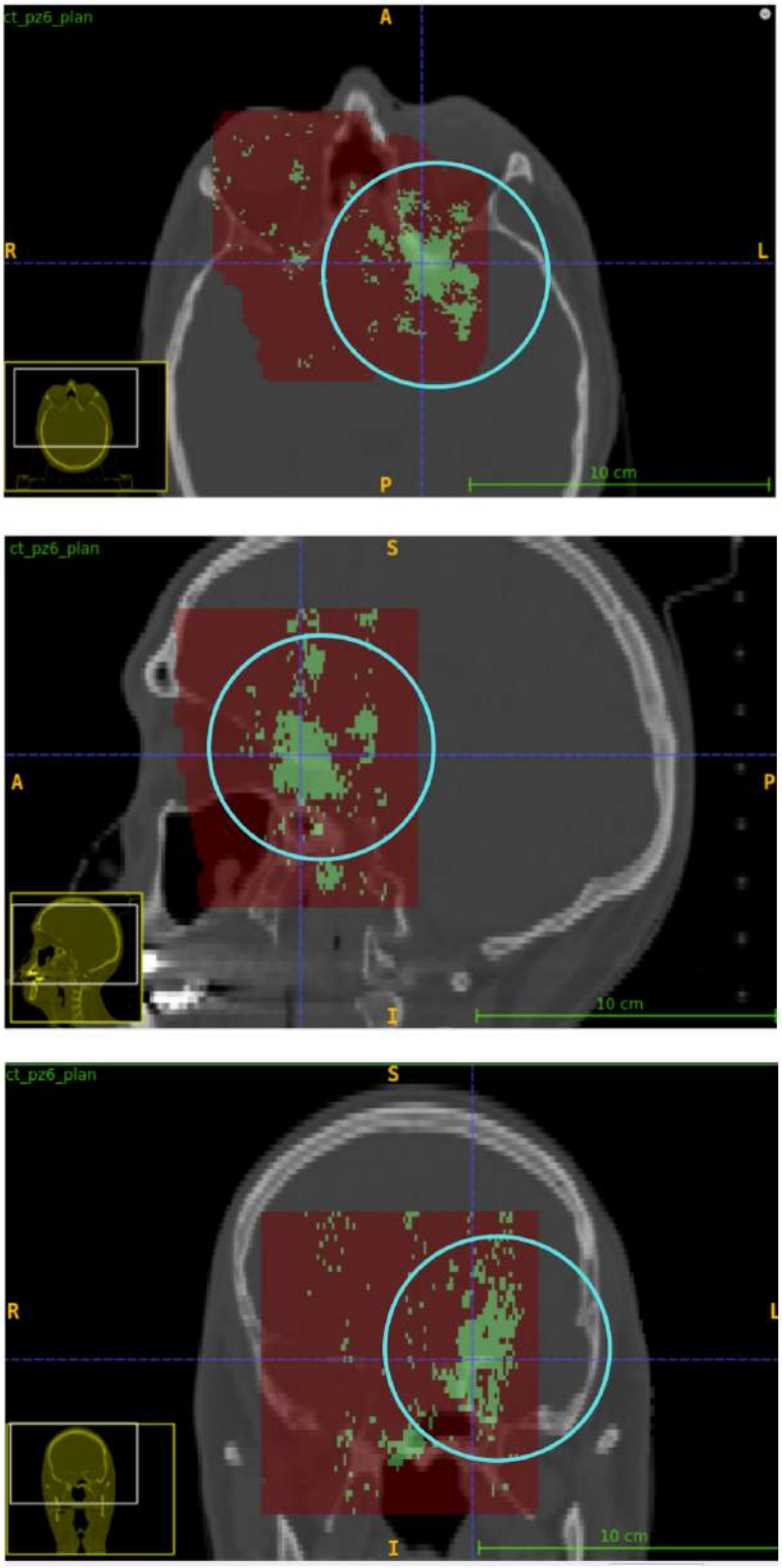

Figure 4.20: Pass rate map for DD = 0.25%, DTA = 20 mm, DTH = 0%, showing a spurious variation (blue circle) not corresponding to a real morphological change, in axial, sagittal and coronal views (from top to bottom), overlaid on the planning CT.

Gamma Index Analysis with Revised DD Definition

A revised definition of the emission Density Distance (DD) parameter, introduced in Equation 4.10, is provided to account for the voxel intensity in the evaluation map, thereby measuring the relative change experienced by each voxel between the two maps. The new definition is given by:

$$\mathrm{DD} = \frac{D}{D_{\mathrm{e}}(\vec{r}_{\mathrm{e}})} \times 100\%, \tag{4.13}$$

where $D_{\mathrm{e}}(\vec{r}_{\mathrm{e}})$ is the intensity of the voxel at position $\vec{r}_{\mathrm{e}}$ in the evaluation map. This formulation allows the gamma index to remain sensitive to meaningful variations in low-intensity regions, while reducing false positives in high-intensity areas, leading to a more accurate detection of morphological changes. This improvement is achieved, however, at the price of losing a strict interpretation of the gamma index as a true metric, since the modified DD no longer represents a pure distance measure in the original sense.

In this study, the emission Density Distance parameter DD is varied from 20% to 55% in steps of 5%. A Density THreshold (DTH) of 0.5% is applied to exclude voxels with emission values close to zero, which could otherwise lead to divergences or instabilities in the DD calculation. Finally, the Distance-To-Agreement (DTA) parameter is varied from 2 to 8 mm in steps of 2 mm.

The new values of efficiency δ and purity ϵ obtained in this way (without modifying the region of interest or the ΔHU map) are shown in Figure 4.21, highlighting a significant improvement compared to the previous definition of the DD parameter (Figure 4.15). In this case, for the same value of DTH analyzed, both efficiency and purity are displayed on the same plot to facilitate a direct comparison of their trends. The purity lies approximately in the range 10–40%, while the efficiency lies approximately in the range 5–25%. The two metrics exhibit opposite trends as a function of DD: as one increases, the other decreases. Nevertheless, the purity shows a steeper growth compared to the efficiency.

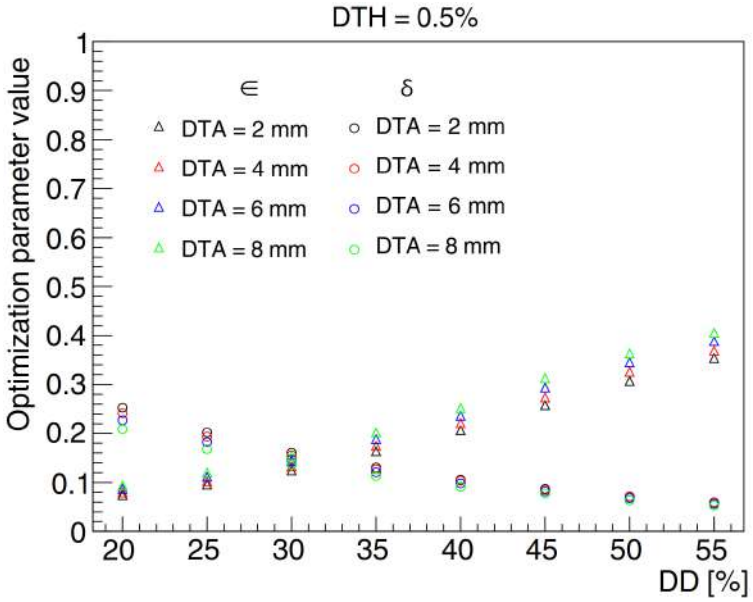

Figure 4.21: Efficiency δ and purity ϵ trends as a function of DD for different values of DTA (specified in the legend) and for DTH = 0.5%, for the modified definition of DD.

As an illustrative example of the effect of maximizing purity, Figure 4.22 shows the pass rate map for DD = 55%, DTA = 8 mm, DTH = 0.5% in axial, sagittal and coronal views (from top to bottom), while Figure 4.23 presents the corresponding gamma mode map. In this configuration, the gamma index exhibits a purity of nearly 40% and an efficiency of approximately 5%.
The larger morphological variation is clearly identified (see the left panel of Figure 3.3 and the bottom panel of Figure 3.5 for the corresponding CT-based visualization), and the resulting maps appear significantly cleaner and better defined compared to maps obtained using the previous definition of the gamma index. The smaller morphological variation, however, is not detected.

On the other hand, to illustrate the effect of maximizing efficiency, Figure 4.24 shows the pass rate map for DD = 20%, DTA = 2 mm, DTH = 0.5% in axial, sagittal and coronal views (from top to bottom), while Figure 4.25 presents the corresponding gamma mode map. In this configuration, the efficiency reaches nearly 25%, while purity is approximately 8%.
Compared to purity maximization, efficiency maximization enables an almost complete detection of the deep morphological variation (see the left panel of Figure 3.3 and the bottom panel of Figure 3.5 for the corresponding CT-based visualization). However, as a consequence, the pass rate maps become less well defined: the presence of scattered green voxels may be misleading when assessing whether a true morphological variation has occurred. In this configuration, for instance, it is not clear whether the smaller morphological variation (see the right panel of Figure 3.3 and the top panel of Figure 3.5 for the corresponding CT-based visualization) of the analysed patient is correctly identified or if the observed signal corresponds to a spurious cluster of green voxels.

Parameter values that guarantee intermediate levels of purity and efficiency are thus identified as optimal, as they ensure a balance between detecting a substantial fraction of the morphological variation while maintaining sufficient purity, thereby avoiding excessively noisy maps and preserving their reliability.
By prioritizing the optimization of purity, which allows for clean and well-defined maps while reducing the risk of false positives, an intermediate DD value oriented towards maximizing purity, equal to 45%, is chosen. At the same time, selecting DTA = 4 mm yields, for the same DD, a sensible higher efficiency compared to DTA values of 6 mm or 8 mm, which would further maximize purity. The resulting maps, shown in Figure 4.26 in pass rate mode and Figure 4.27 in gamma mode, therefore represent a good compromise between image purity and the detection of a wide area of morphological variation. With these parameter choices, an efficiency of approximately 10% and a purity of approximately 29% is obtained. However, also in this case, only the deeper and larger morphological variation is correctly detected (see the left panel of Figure 3.3 and the bottom panel of Figure 3.5 for the CT-based visualization).

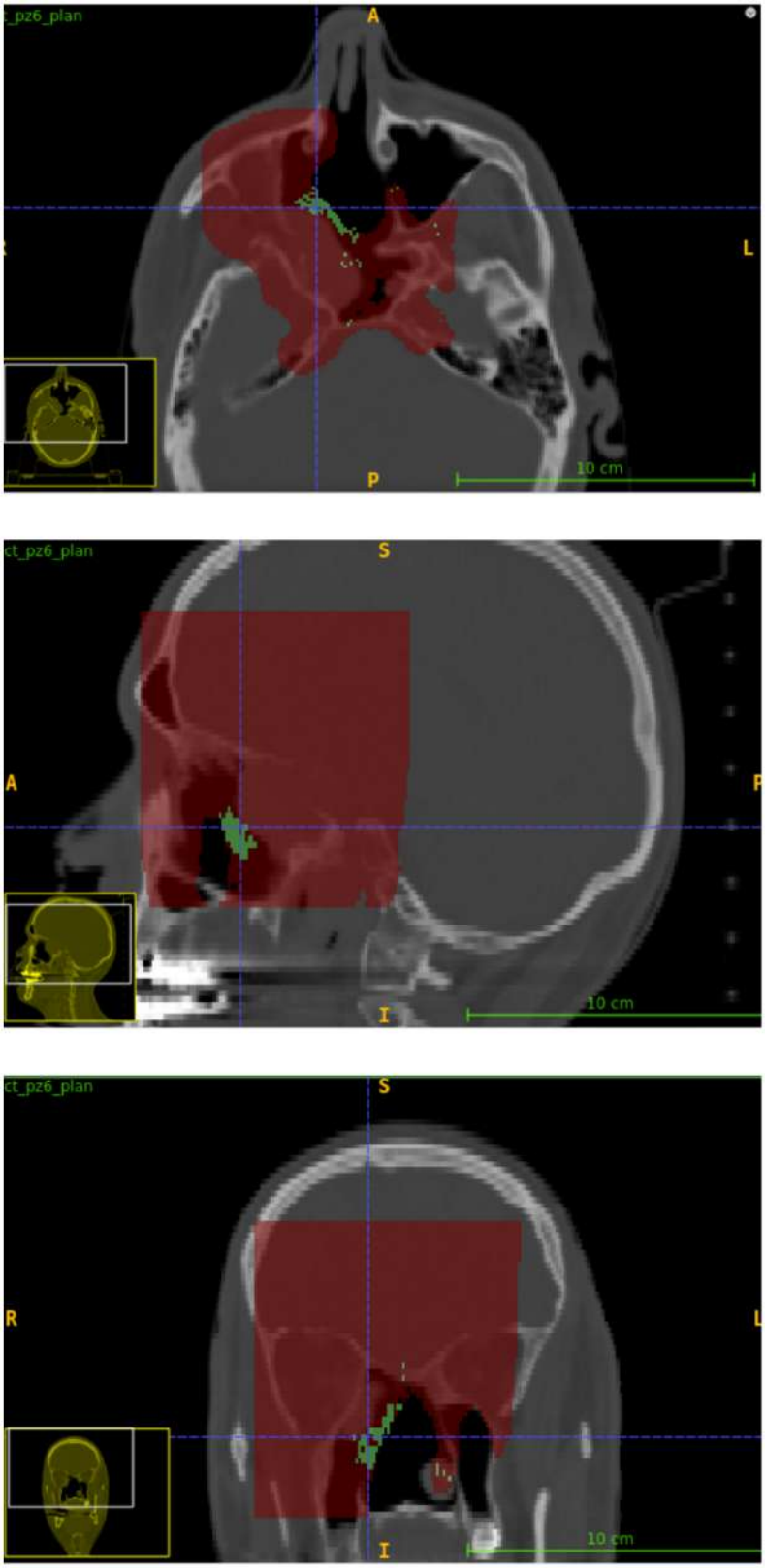

Figure 4.22: Pass rate map for DD = 55%, DTA = 8 mm, DTH = 0.5% in axial, sagittal and coronal views (from top to bottom), overlaid on the planning CT.

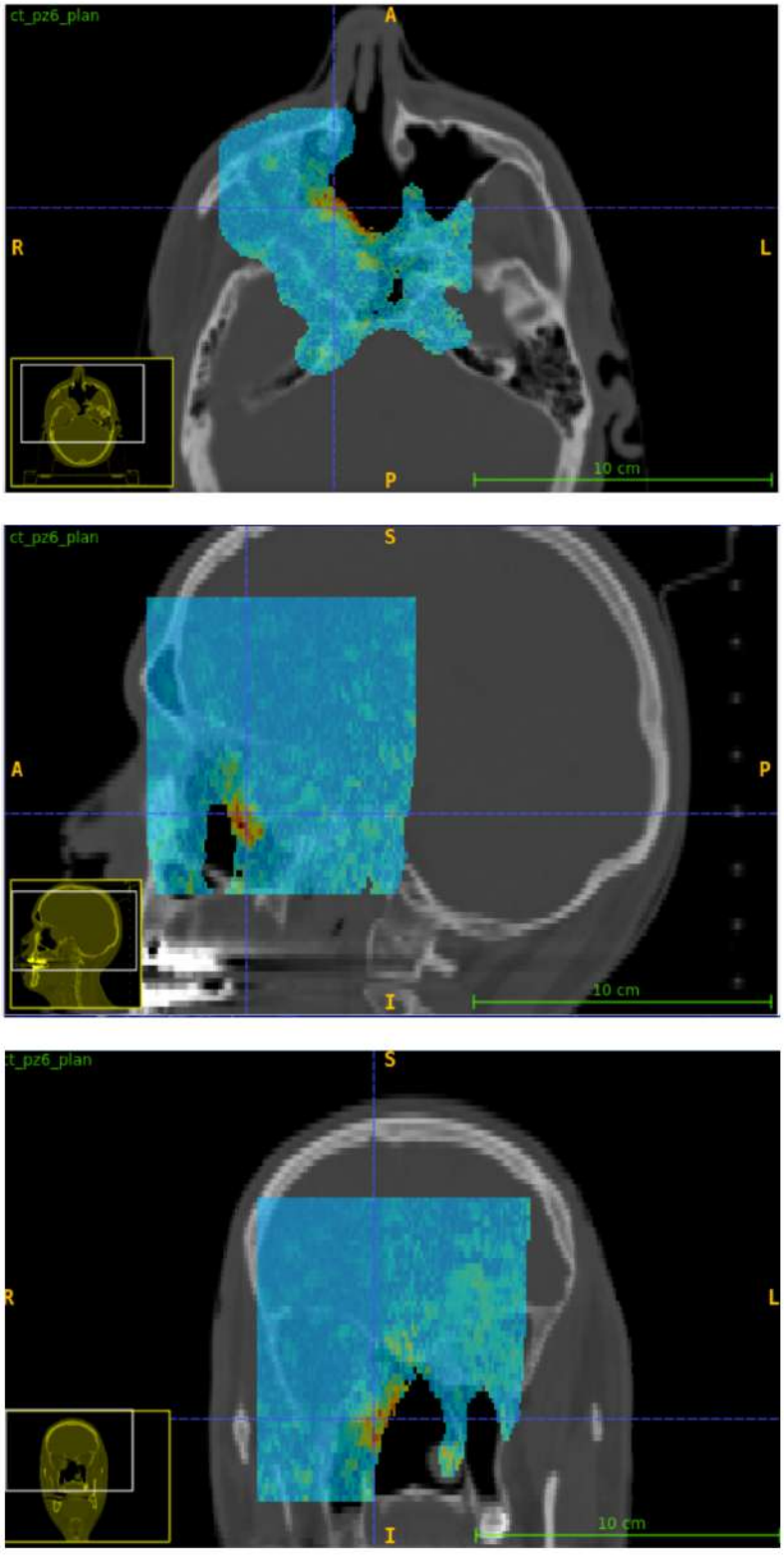

Figure 4.23: Gamma mode map for DD = 55%, DTA = 8 mm, DTH = 0.5% in axial, sagittal and coronal views (from top to bottom), overlaid on the planning CT.

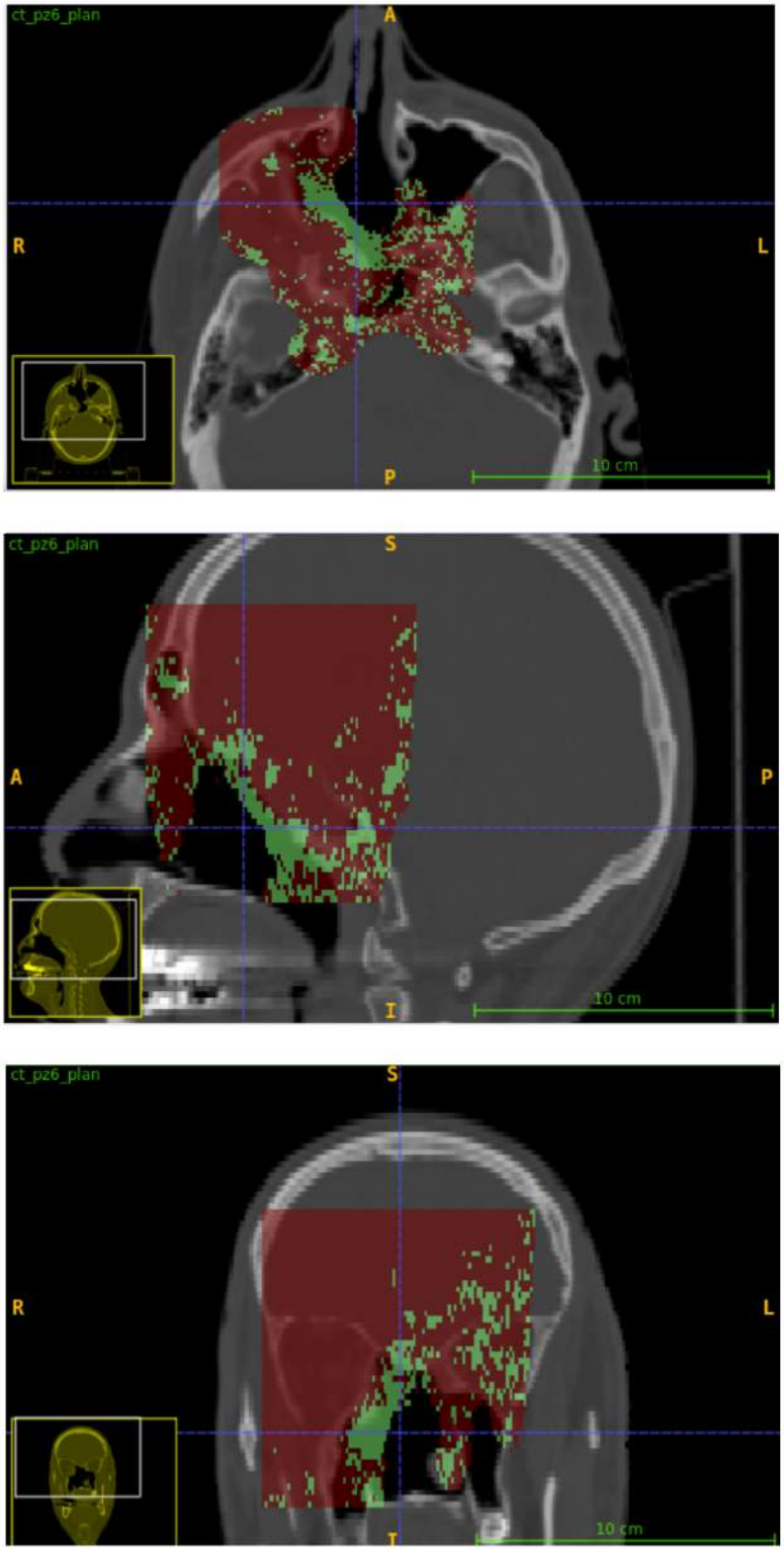

Figure 4.24: Pass rate map for DD = 20%, DTA = 2 mm, DTH = 0.5% in axial, sagittal and coronal views (from top to bottom), overlaid on the planning CT.

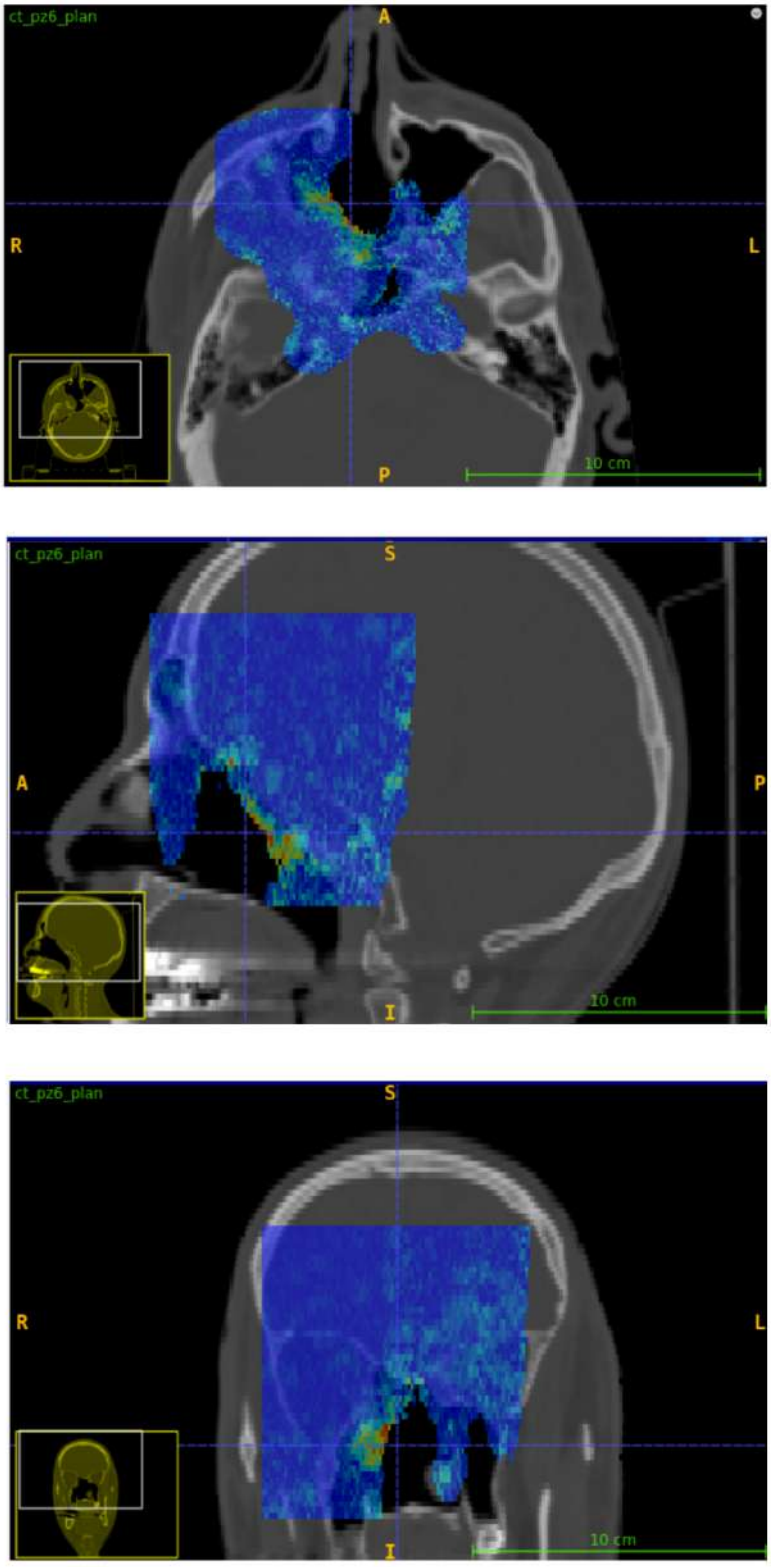

Figure 4.25: Gamma mode map for DD = 20%, DTA = 2 mm, DTH = 0.5% in axial, sagittal and coronal views (from top to bottom), overlaid on the planning CT.

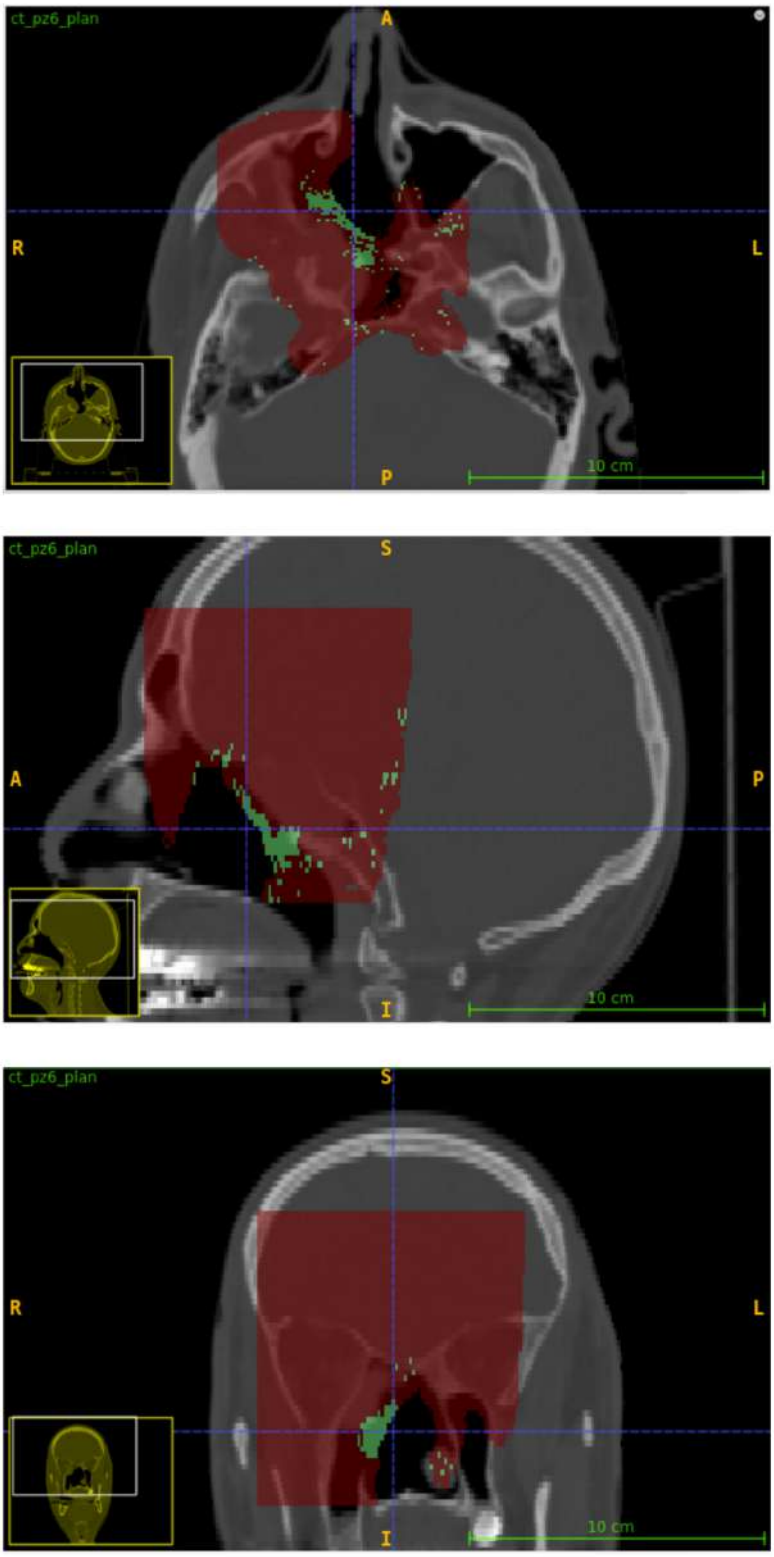

Figure 4.26: Pass rate map for DD = 45%, DTA = 4 mm, DTH = 0.5% in axial, sagittal and coronal views (from top to bottom), overlaid on the planning CT.

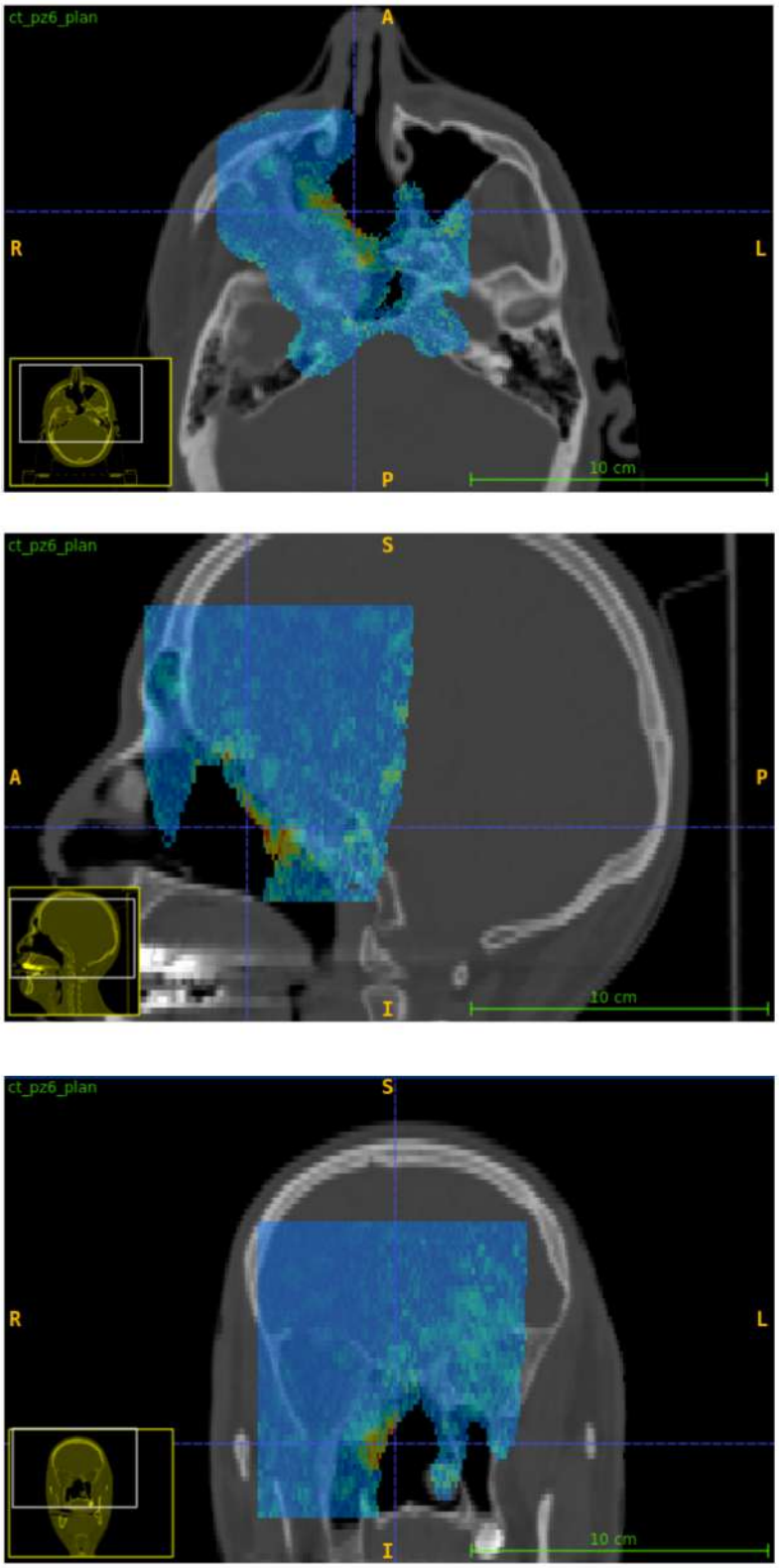

Figure 4.27: Gamma mode map for DD = 45%, DTA = 4 mm, DTH = 0.5% in axial, sagittal and coronal views (from top to bottom), overlaid on the planning CT.

The analysis shows that MULTIPASS is capable of detecting morphological variations through the gamma-index map method, but careful tuning of the gamma-index parameters is crucial. The present study highlights both the potential and the limitations of the method, and motivates further systematic investigations to refine the technique and establish robust criteria for clinical application.
From the analysis presented in this chapter, it clearly emerges that finding a set of parameters providing a suitable compromise between purity and efficiency, such that true morphological variations are visualized while avoiding false positives, is a challenging task. The analysed case represents a particularly demanding scenario, as the major morphological variation is located deep inside the patient and is not directly intersected by the high-dose region. This configuration emphasizes the need to adapt the analysis parameters to such situations, or even to reconsider their interpretation, for instance through the alternative definition of the DD parameter provided.

Systematic studies on a larger cohort of patients, considering different types of morphological changes (both superficial and deep), are essential in order to fully optimize the capabilities of the gamma index method, using both the DD parameter definition adopted in previous studies and the alternative definition proposed in this thesis.
By studying a variety of patient cases, it will be possible to identify which parameter sets allow the detection of morphological variations with specific characteristics, such as depth, level of dose received or size. This will help determine whether a single, compromise set of parameters for the gamma index method can be applied universally, or whether specific parameter sets need to be defined for typical situations and applied either consecutively or guided by clinical knowledge of the potential evolution of the tumor mass.

4.6 Comparison with the Dose Profiler

Having studied for the first time the ability of MULTIPASS to detect morphological variations in a patient, it is now possible to perform a comparison with the Dose Profiler on the same case of study. This comparison is particularly meaningful, as both detectors were operated under comparable conditions, with the same angular acceptance and orientation relative to the patient, as described in Section 3.3.

The results obtained with the Dose Profiler, based on both experimental data and Monte Carlo simulations, are reported in [66]. In that study, the sensitivity of the DP to morphological variations was evaluated without defining a specific region of interest. Gamma index maps were computed using the DD parameter defined in Equation 4.10, with the investigated parameter ranges set to 2–14% for DD (in steps of 2%) and 10–45 mm for DTA (in steps of 5 mm), while DTH was fixed at 5%. The resulting efficiency and purity values for experimental data are shown in Figure 4.28. The efficiency attains its maximum value of 1% for DD= 2% and DTA= 10 mm, while the purity reaches a maximum value of 1% for DD= 2% and DTA= 45 mm. The Monte Carlo simulation yields results consistent with those obtained from experimental data, with similar efficiency and purity values also observed in the simulation. In particular, the highest purity value is approximately 1%, obtained for DTA= 40 mm and DD= 4%.
Such low values of purity and efficiency are due to the inability of the DP to detect the largest morphological change (see left panel of Figure 3.3), both in experimental data and in Monte Carlo simulations. For the second, smaller morphological variation (see right panel of Figure 3.3), the DP identifies a cluster of discrepant voxels that is not spatially aligned with the actual anatomical change, but is instead shifted along the primary beam

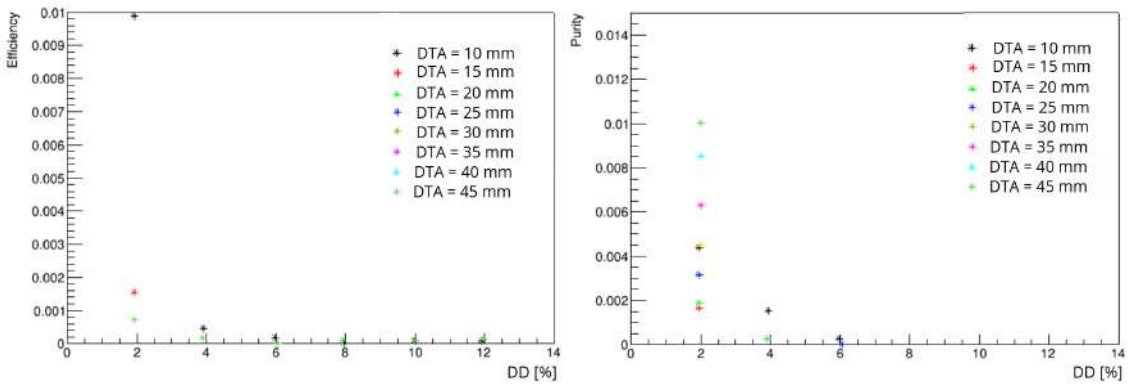

Figure 4.28: Efficiency and purity obtained with the Dose Profiler as a function of the gamma index parameters DD and DTA, with DTH fixed at 5%. Results are shown for experimental data. Image adapted from [66].

direction, again consistently in both data and simulation.

As an example, Figure 4.29 shows the pass rate map obtained for DD= 4% and DTA= 40 mm, corresponding to the maximum purity in the Monte Carlo simulation, where the spatial misalignment of the detected morphological variation along the primary beam direction can be clearly observed.

Considering the efficiency and purity values obtained with MULTIPASS using the same DD definition (Equation 4.10) in the gamma index calculation, the results are improved (Figure 4.15). Considering, for example, the map obtained for DD= 1.5%, DTA= 20 mm, and DTH= 0% (Figure 4.16), which corresponds to a parameter configuration similar to that investigated in [66], the achieved purity, although limited to approximately 2%, indicates a correct identification of the small superficial morphological variation, as highlighted by the gamma-index maps.

The study conducted with MULTIPASS may suggest further investigations into the Dose Profiler's ability to detect deep morphological variations, including a potential assessment of its performance using the new DD definition (Equation 4.13), which appears to show promising results in MULTIPASS, as well as further investigation into the observed misalignment between the morphological changes detected in the gamma-index maps and the expected anatomical regions of variation.

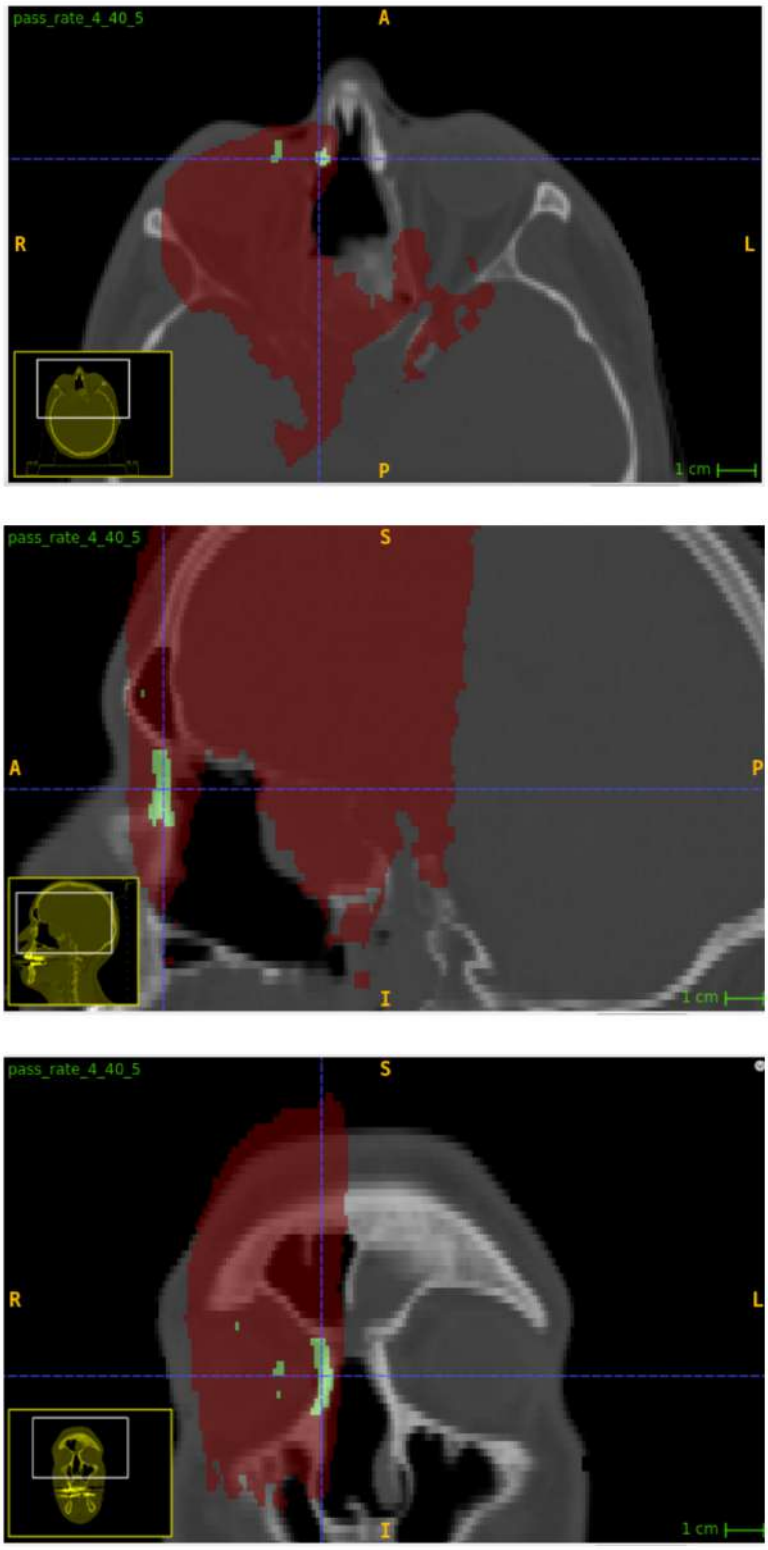

Figure 4.29: Pass rate map obtained with the Dose Profiler for DD= 4%, DTA= 40 mm, DTH = 5% in the Monte Carlo study. The smaller detected morphological variation is not spatially aligned with the actual change, while the larger variation is not detected.

Conclusion

In this thesis, a Monte Carlo study using the FLUKA code was performed to investigate the capability of the MULTIPASS detector, a compact prototype based on scintillating fibers, to identify inter-fractional morphological changes in patients undergoing carbon-ion treatments by detecting charged secondary particles (especially secondary protons). Its performance was directly compared with that of the Dose Profiler, a charged secondary particles tracker developed within the INSIDE project and currently installed in treatment room 1 at CNAO (Pavia, Italy), where it is being tested in phase II of a clinical trial (ClinicalTrials.gov Identifier: NCT03662373).
To perform the study, a patient affected by head and neck cancer who had undergone a mid-treatment *control* CT and had previously been measured and analyzed with the Dose Profiler was selected. Between the *planning* CT and the *control* CT, the patient underwent two morphological changes, one larger and deep-seated, which has led to a treatment replan, and one smaller and more superficial.
Two simulations were carried out: one applying the treatment plan to the *planning* CT, and the other to the *control* CT, effectively simulating two fractions of the treatment.

A dedicated C++ analysis framework was developed to process the FLUKA simulation outputs, building upon and extending the framework previously implemented for the Dose Profiler. The first phase of the analysis involved the implementation of a trigger to select events for further processing, specifically those corresponding to secondary protons with sufficient energy to achieve the desired backtracking resolution suitable for charged fragments monitoring applications (< 10 mm). In this study, a resolution of 7 mm was achieved. After the event selection, proton tracks were reconstructed and fitted, and the emission coordinates of charged secondary particles were estimated using the Point of Closest Approach (POCA) method. These coordinates were used to generate 3D emission maps overlaid on the patient CT. Finally, the 3D emission maps obtained for both the *planning* and *control* CT datasets were compared using the gamma-index method to identify morphological variations between treatment fractions. The performance in identifying regions affected by morphological changes was then evaluated through two complementary metrics: efficiency (δ) and purity (ϵ). Efficiency measures the fraction of voxels corresponding to true morphological variations that are correctly detected, while purity indicates the fraction of voxels flagged as discrepant by the gamma-index test that truly correspond to morphological changes.

The gamma-index analysis highlighted several challenges. Since the method was originally developed in clinics to compare dose distributions, its application to secondary-particle emission maps required careful tuning of the parameters, specifically DTA (Distance To Agreement), DTH (Density THreshold), and DD (emission Density Distance).
In the studied case, the largest morphological change, that clinically led to a treatment replan of the patient, was deep-seated and characterized by low emission intensity, making

it essentially undetectable when using conventional DD values (typically above 2% from Dose Profiler previous studies), which resulted in a purity of about 2% and an efficiency close to zero.
Reducing the DD value to 0.25% increased sensitivity in low-emission regions, yielding an efficiency of approximately 12% and a purity of around 5%, but at the cost of significant noise and false positives. In the presented study, a modified definition of DD, accounting for relative intensity variations, was introduced. This adjustment enhanced the clear detection of the deep morphological change, increasing the purity to around 29% for an efficiency of approximately 10%, for DTA = 4 mm, DTH = 0.5%, and DD = 45%.

Overall, the analysis shows that MULTIPASS is capable of detecting inter-fractional morphological variations through gamma-index maps, although the sensitivity and accuracy of the detection strongly depends on the choice and interpretation of the gamma-index parameters. The analyzed case was particularly challenging, as the main morphological change was located deep inside the patient and outside the high-dose region, making it difficult to detect with standard parameter settings. This highlights the need for tailored analysis strategies and motivates further systematic studies on larger patient cohorts, including both superficial and deep anatomical variations, with specific characteristics such as dose level and spatial extent, in order to define robust and clinically applicable criteria.

The comparison with the Dose Profiler was carried out using the original DD definition, as studied in [66]. The analysis shows that the Dose Profiler is unable to detect the deep morphological change, while the superficial variation is identified as a cluster of voxels that is spatially misaligned with the actual anatomical modification, resulting in very low efficiency and purity of approximately 1%. In contrast, MULTIPASS demonstrates clear improvements in both efficiency and purity even when evaluated under the same DD definition.
Furthermore, the methodological advancements developed in this thesis work within the MULTIPASS project, including the modified DD parameter, could be applied to the Dose Profiler to enhance its sensitivity to anatomical variations in clinical practice. This is particularly important considering that the Dose Profiler is already operational and acquiring clinical data within the CNAO clinical trial, highlighting the potential immediate impact of these developments on patient-specific treatment monitoring.

Bibliography

[1] M. Durante, R. Orecchia, and J.S. Loeffler. "Charged-particle therapy in cancer: clinical uses and future perspectives". In: *Nature Reviews Clinical Oncology* 14.8 (Aug. 2017). Epub 2017 Mar 14, pp. 483–495. DOI: 10.1038/nrclinonc.2017.30.

[2] H. Paganetti. "Relative biological effectiveness (RBE) values for proton beam therapy: Variations as a function of biological endpoint, dose, and linear energy transfer". In: *Physics in Medicine and Biology* 59.22 (Nov. 2014). Epub 2014 Oct 31, R419–R472. DOI: 10.1088/0031-9155/59/22/R419.

[3] F. Tommasino, E. Scifoni, and M. Durante. "New ions for therapy". In: *International Journal of Particle Therapy* 2.3 (2016). Epub 2016 Feb 9, pp. 428–438. DOI: 10.14338/IJPT-15-00027.1.

[4] Harald Paganetti. "Range uncertainties in proton therapy and the role of Monte Carlo simulations". In: *Physics in Medicine Biology* 57.11 (May 2012), R99. DOI: 10.1088/0031-9155/57/11/R99. URL: https://doi.org/10.1088/0031-9155/57/11/R99.

[5] N. Carron. *An introduction to the passage of energetic particles through matter*. CRC Press, 2006. ISBN: 9780429137396. DOI: 10.1201/9781420012378.

[6] Niels Bohr. "On the Theory of the Decrease of Velocity of Moving Electrified Particles on Passing through Matter". In: *The London, Edinburgh, and Dublin Philosophical Magazine and Journal of Science*. 6th ser. 25.145 (1913), pp. 10–31. DOI: 10.1080/14786440108634359.

[7] Hans A. Bethe. "Zur Theorie des Durchgangs schneller Korpuskularstrahlen durch Materie". In: *Annalen der Physik* 397.3 (1930), pp. 325–400. DOI: 10.1002/andp.19303970303.

[8] Felix Bloch. "Zur Bremsung rasch bewegter Teilchen beim Durchgang durch Materie". In: *Zeitschrift für Physik* 81 (1933), pp. 363–376. DOI: 10.1007/BF01339455.

[9] W. R. Leo. *Techniques for nuclear and particle physics experiments*. Berlin, Heidelberg: Springer-Verlag Berlin Heidelberg, 1994.

[10] D. E. Groom, N. V. Mokhov, and S. I. Striganov. "Muon stopping power and range tables 10 MeV–100 TeV". In: *Atomic Data and Nuclear Data Tables* 78.2 (2001), pp. 183–356. DOI: 10.1006/adnd.2001.0861.

[11] M. Plum. "Interceptive beam diagnostics: Signal creation and materials interactions". In: *AIP Conference Proceedings* 732 (2004). DOI: 10.1063/1.1831132.

[12] C. Stengl. "In-phantom dosimetry study for target and organs at risk during breathing-induced motion: Improving pancreatic cancer treatment by combining carbon ion and mini-beam irradiation". PhD thesis. Heidelberg, Germany: Ruprecht-Karls-Universität Heidelberg, Medizinische Fakultät, 2020.

[13] C.-A. Reidel. “Applications for CMOS pixel sensors in ion-beam therapy”. École Doctorale de Physique et Chimie-Physique, Institut Pluridisciplinaire Hubert Curien. PhD thesis. Strasbourg, France: Université de Strasbourg, 2016.

[14] G. Molière. “Theorie der streuung schneller geladener teilchen II: Mehrfach- und vielfachstreuung”. In: *Zeitschrift für Naturforschung A* 3.2 (1948), pp. 78–97. DOI: 10.1515/zna-1948-0203.

[15] V. L. Highland. “Some practical remarks on multiple scattering”. In: *Nuclear Instruments and Methods* 129.2 (1975), pp. 497–499. DOI: 10.1016/0029-554X(75)90743-0.

[16] V. L. Highland. “Erratum”. In: *Nuclear Instruments and Methods* 161.1 (1979), p. 171. DOI: 10.1016/0029-554X(79)90379-3.

[17] E. Haettner et al. “Experimental study of nuclear fragmentation of 200 and 400 MeV/u ^{12}C ions in water for applications in particle therapy”. In: *Physics in Medicine and Biology* 58 (2013), pp. 8265–8279. DOI: 10.1088/0031-9155/58/23/8265.

[18] R. Serber. “Nuclear Reactions at High Energies”. In: *Phys. Rev.* 72 (11 Dec. 1947), pp. 1114–1115. DOI: 10.1103/PhysRev.72.1114.

[19] K. Gunzert-Marx et al. “Secondary beam fragments produced by 200 MeV/u ^{12}C ions in water and their dose contributions in carbon ion radiotherapy”. In: *New Journal of Physics* 10.7 (2008), p. 075003. DOI: 10.1088/1367-2630/10/7/075003.

[20] C. Steffer and J. D. Harrison. “The ICRP protection quantities, equivalent and effective dose: Their basis and application”. In: *Radiation Protection Dosimetry* 127.1–4 (2007), pp. 1–4. DOI: 10.1093/rpd/ncm175.

[21] Elahe Alizadeh, Thomas M. Orlando, and Léon Sanche. “Biomolecular damage induced by ionizing radiation: The direct and indirect effects of low-energy electrons on DNA”. In: *Annual Review of Physical Chemistry* 66.1 (2015), pp. 379–398.

[22] P. L. Olive. “The role of DNA single- and double-strand breaks in cell killing by ionizing radiation”. In: *Radiation Research* 150.5s (1998).

[23] Eric J. Hall and Amato J. Giaccia. *Radiobiology for the Radiologist*. 8th. Lippincott, 2019.

[24] B. Milborne et al. “The use of biomaterials in internal radiation therapy”. In: *Recent Progress in Materials* 2 (2020), pp. 1–34. DOI: 10.21926/rpm.2002012.

[25] H. P. Leenhouts and K. H. Chadwick. “A molecular theory of cell survival”. In: *Phys. Med. Biol.* 13 (1973), pp. 78–87.

[26] Ugo Amaldi and Gerhard Kraft. “Radiotherapy with beams of carbon ions”. In: *Reports on Progress in Physics* 68.8 (July 2005), p. 1861. DOI: 10.1088/0034-4885/68/8/R04.

[27] GSI Helmholtzzentrum für Schwerionenforschung. *Particle Irradiation Data Ensemble (PIDE)*. https://www.gsi.de/bio-pide. 2025.

[28] Marco Durante et al. “Applied nuclear physics at the new high-energy particle accelerator facilities”. In: *Physics Reports* 800 (2019), pp. 1–37.

[29] Antje-Christin Knopf and Antony Lomax. “In vivo proton range verification: a review”. In: *Physics in Medicine Biology* 58.15 (July 2013), R131. DOI: 10.1088/0031-9155/58/15/R131.

[30] A. Bridier and J. Chavaudra. "Definition of volumes in external radiotherapy: ICRU reports 50 and 62". In: *Cancer Radiotherapie* 5.5 (2001), pp. 472–478.

[31] K. Parodi. "PET monitoring of hadrontherapy". In: *Nuclear Medicine Review* 15 (2012), pp. C37–C42.

[32] G. Battistoni, I. Mattei, and S. Muraro. "Nuclear physics and particle therapy". In: *Advances in Physics: X* 1.4 (2016), pp. 661–686. DOI: 10.1080/23746149.2016.1237310.

[33] J. Krimmer et al. "Prompt-gamma monitoring in hadrontherapy: A review". In: *Nuclear Instruments and Methods in Physics Research Section A* 878 (Jan. 2018), pp. 58–73. DOI: 10.1016/j.nima.2017.07.063.

[34] S. Muraro et al. "Monitoring of Hadrontherapy Treatments by Means of Charged Particle Detection". In: *Frontiers in Oncology* 6 (Aug. 2016), p. 177. DOI: 10.3389/fonc.2016.00177.

[35] J. Mattingly, K. S. Ytre-Hauge, K. Skjerdal, et al. "A Monte Carlo feasibility study for neutron-based real-time range verification in proton therapy". In: *Scientific Reports* 9 (2019), p. 2011.

[36] J. Lerendegui-Marco et al. "Simultaneous neutron and gamma imaging system for real-time range and dose monitoring in hadron therapy and nuclear security applications". In: *EPJ Web of Conferences*. Vol. 261. 2022, p. 05001.

[37] K. Parodi et al. "Patient study of in vivo verification of beam delivery and range using positron emission tomography and computed tomography imaging after proton therapy". In: *International Journal of Radiation Oncology, Biology, Physics* 68.3 (2007), pp. 920–934.

[38] K. Inoue, T. Nishio, and A. Miyatake. "Experimental verification of proton beam monitoring in a human body by use of activity image of positron-emitting nuclei generated by nuclear fragmentation reaction". In: *Radiological Physics and Technology* 1.1 (2008), pp. 44–54.

[39] W. Hsi et al. "In vivo verification of proton beam path by using post-treatment PET/CT imaging". In: *Medical Physics* 36 (2009), pp. 4136–4146.

[40] X. Zhu et al. "Monitoring proton radiation therapy with in-room PET imaging". In: *Physics in Medicine and Biology* 56.13 (2011), pp. 4041–4057.

[41] W. Enghardt et al. "Charged hadron tumour therapy monitoring by means of PET". In: *Nuclear Instruments and Methods in Physics Research* 525 (2004), pp. 284–288.

[42] W. Enghardt et al. "Dose quantification from in-beam positron emission tomography". In: *Radiotherapy and Oncology* 73 (2004), S96–S98.

[43] Georgy Shakirin et al. "Implementation and workflow for PET monitoring of therapeutic ion irradiation: a comparison of in-beam, in-room, and off-line techniques". In: *Physics in Medicine Biology* 56.5 (Feb. 2011), p. 1281. DOI: 10.1088/0031-9155/56/5/004.

[44] I. Mattei et al. "Prompt-γ production of 220 MeV/u ^{12}C ions interacting with a PMMA target". In: *Journal of Instrumentation* 10.10 (2015), P10034. DOI: 10.1088/1748-0221/10/10/P10034.

[45] C. Agodi, F. Bellini, P. Cirrone, et al. "Precise measurement of prompt photon emission from 80 MeV/u carbon ion beam irradiation". In: *Journal of Instrumentation* 7 (Mar. 2012), P03001. DOI: 10.1088/1748-0221/7/03/P03001.

[46] J. M. Verburg et al. "Energy- and time-resolved detection of prompt gamma-rays for proton range verification". In: *Physics in Medicine and Biology* 58.20 (2013), p. L37. DOI: 10.1088/0031-9155/58/20/L37.

[47] J. Krimmer et al. "Prompt-gamma monitoring in hadrontherapy: A review". In: *Journal of Instrumentation* 878 (2018), pp. 58–73.

[48] P. G. Thirolf et al. "A Compton camera prototype for prompt-γ medical imaging". In: *EPJ Web of Conferences*. Vol. 117. 2016, p. 05005.

[49] E. Haettner, H. Iwase, and D. Schardt. "Experimental fragmentation studies with C-12 therapy beams". In: *Radiation Protection Dosimetry* 122 (2006), pp. 485–487. DOI: 10.1093/rpd/ncl402.

[50] L. Piersanti et al. "Measurement of charged particle yields from PMMA irradiated by a 220 MeV/u ^{12}C beam". In: *Physics in Medicine and Biology* 59.7 (2014), pp. 1857–1872.

[51] I. Mattei et al. "Addendum: Measurement of charged particle yields from PMMA irradiated by a 220 MeV/u ^{12}C beam". In: *Physics in Medicine and Biology* 62.21 (2017), pp. 8483–8494.

[52] C. Agodi et al. "Charged particle flux measurement from PMMA irradiated by an 80 MeV/u carbon ion beam". In: *Physics in Medicine and Biology* 57.18 (2012), pp. 5667–5678.

[53] A. Rucinski et al. "Secondary radiation measurements for particle therapy applications: Charged secondaries produced by ^{16}O ion beams in a PMMA target at large angles". In: *Physica Medica: European Journal of Medical Physics* 64 (2019), pp. 45–53.

[54] K. Gunzert-Marx, D. Schardt, and R. S. Simon. "Fast neutrons produced by nuclear fragmentation in treatment irradiations with ^{12}C beam". In: *Radiation Protection Dosimetry* 110.1–4 (2004), pp. 595–600. DOI: 10.1093/rpd/nch138.

[55] Martha Hultqvist and Irena Gudowska. "Secondary absorbed doses from light ion irradiation in anthropomorphic phantoms representing an adult male and a 10 year old child". In: *Physics in Medicine Biology* 55.22 (Oct. 2010), p. 6633. DOI: 10.1088/0031-9155/55/22/004.

[56] U. Amaldi et al. "Advanced Quality Assurance for CNAO". In: *Nuclear Instruments and Methods in Physics Research Section A: Accelerators, Spectrometers, Detectors and Associated Equipment* 617.1 (2010), pp. 248–249. DOI: https://doi.org/10.1016/j.nima.2009.06.087.

[57] P. Henriquet et al. "Interaction vertex imaging (IVI) for carbon ion therapy monitoring: a feasibility study". In: *Physics in Medicine and Biology* 57.14 (July 2012), pp. 4655–4669. DOI: 10.1088/0031-9155/57/14/4655.

[58] M. Fischetti, G. Baroni, G. Battistoni, et al. "Inter-fractional monitoring of ^{12}C ion treatments: results from a clinical trial at the CNAO facility". In: *Scientific Reports* 10.1 (2020), p. 20735. DOI: 10.1038/s41598-020-77843-z.

[59] Marco Toppi et al. "Monitoring Carbon Ion Beams Transverse Position Detecting Charged Secondary Fragments: Results From Patient Treatment Performed at CNAO". In: *Frontiers in Oncology* 11 (June 2021), p. 601784. DOI: 10.3389/fonc.2021.601784.

[60] M. Marafini et al. “The INSIDE Project: Innovative Solutions for In-Beam Dosimetry in Hadrontherapy”. In: *Acta Physica Polonica A* 127 (2015), pp. 1465–1467.

[61] V. Ferrero et al. “The INSIDE project: on-line monitoring and simulation validation with the in-beam PET scanner”. In: *Journal of Physics: Conference Series* 841 (2017), p. 012011.

[62] G. Traini et al. “Review and performance of the Dose Profiler, a particle therapy treatments online monitor”. In: *Physica Medica* 65 (2019), pp. 84–93. ISSN: 1120-1797. DOI: https://doi.org/10.1016/j.ejmp.2019.07.010.

[63] Thomas Kormoll et al. “A prototype Compton camera for in-vivo dosimetry of ion beam cancer irradiation”. In: (June 2011). DOI: 10.1109/NSSMIC.2011.6152639.

[64] M. Toppi et al. “PAPRICA: The Pair Production Imaging Chamber—Proof of Principle”. In: *Frontiers in Physics* 9 (Mar. 2021), p. 568139. DOI: 10.3389/fphy.2021.568139.

[65] M. Marafini et al. “MONDO: A neutron tracker for particle therapy secondary emission characterisation”. In: *Physics in Medicine and Biology* 62 (Mar. 2017), pp. 3299–3312. DOI: 10.1088/1361-6560/aa623a.

[66] Leonardo Lampertico. “Inter-fractional monitoring of ^{12}C ion treatments with the Dose Profiler detector: simulation studies and clinical trial results at the CNAO facility”. Master’s Thesis. Corso di Laurea Magistrale in Fisica, Università degli Studi di Milano, 2024.

[67] F. Ballarini et al. “The FLUKA code: Overview and new developments”. In: *The European Physical Journal Nuclear Science and Technology* 10 (2024), p. 16.

[68] T. T. Böhlen et al. “The FLUKA code: Developments and challenges for high energy and medical applications”. In: *Nuclear Data Sheets* 120 (2014), pp. 211–214.

[69] A. Ferrari et al. *FLUKA: A multi-particle transport code*. Tech. rep. CERN-2005-010. INFN/TC-05/11, SLAC-R-773. CERN, 2005.

[70] G. Battistoni et al. “The FLUKA code: An accurate simulation tool for particle therapy”. In: *Frontiers in Oncology* 6 (2016).

[71] *FLUKA – A fully integrated particle physics Monte Carlo code*. https://www.fluka.org/. 2025.

[72] Vasilis Vlachoudis. “FLAIR: A powerful but user friendly graphical interface for FLUKA”. In: *Proceedings of the International Conference on Mathematics, Computational Methods & Reactor Physics (M&C 2009)*. FLUKA Advanced Interface. American Nuclear Society. 2009, pp. 790–800.

[73] Rene Brun and Fons Rademakers. “ROOT — An object oriented data analysis framework”. In: *Nucl. Instrum. Meth. A* 389.1-2 (1997). Ed. by M. Werlen and D. Perret-Gallix, pp. 81–86. DOI: 10.1016/s0168-9002(97)00048-x.

[74] G. Fattori and et al. “Commissioning of an integrated platform for time-resolved treatment delivery in scanned ion beam therapy by means of optical motion monitoring”. In: *Technology in Cancer Research & Treatment* 13.6 (2014), pp. 517–528.

[75] Istituto Nazionale di Fisica Nucleare. *Osservare le radiazioni in tempo reale per rendere ancora più precise le terapie oncologiche*. Immagine tratta dal sito INFN, consultato il 28 gennaio 2026. 2019. URL: https://www.infn.it/sservare-le-radiazioni-in-tempo-reale-per-rendere-ancora-piu-precise-le-terapie-oncologiche/.

[76] A. Belardo. “Studio Monte Carlo dell’utilizzo di PAPRICA per inter-fractional monitoring 3D su pazienti trattati al CNAO con adroterapia”. Master’s thesis. Università degli Studi di Milano, 2022.

[77] *3D Slicer User Guide*. Accessed: 2026-01-05. 2025. URL: https://www.slicer.org.

[78] Paul A. Yushkevich et al. “User-guided 3D active contour segmentation of anatomical structures: Significantly improved efficiency and reliability”. In: *NeuroImage* 31.3 (2006), pp. 1116–1128. DOI: 10.1016/j.neuroimage.2006.01.015.

[79] Richard O. Duda and Peter E. Hart. “Use of the Hough transformation to detect lines and curves in pictures”. In: *Commun. ACM* 15.1 (Jan. 1972), pp. 11–15. ISSN: 0001-0782. DOI: 10.1145/361237.361242. URL: https://doi.org/10.1145/361237.361242.

[80] Daniel A. Low et al. “A technique for the quantitative evaluation of dose distributions”. In: *Medical Physics* 25.5 (May 1998), pp. 656–661. DOI: 10.1118/1.598248.

[81] Mohammad Hussein, Catharine Clark, and Andrew Nisbet. “Challenges in calculation of the gamma index in radiotherapy – Towards good practice”. In: *Physica Medica* 36 (Apr. 2017), pp. 1–11. DOI: 10.1016/j.ejmp.2017.03.001.

[82] G. Giacchi. “Monitoraggio 3D inter-frazione delle variazioni morfologiche in trattamenti con ioni ^{12}C al CNAO tramite rivelazione di frammenti secondari carichi”. Master’s thesis. Sapienza Università di Roma, 2022.